9-2017

Evaluation of Stray Light Correction for the Thermal Infrared Sensor (TIRS) from Landsat 8

Fu Jiang
fj4136@rit.edu

Evaluation of Stray Light Correction for the Thermal Infrared Sensor (TIRS) from Landsat 8

by

Fu Jiang

A thesis submitted in partial fulfillment of the
requirements for the degree of Master of Science
in the Chester F. Carlson Center for Imaging Science
College of Science
Rochester Institute of Technology

Sep, 2017

Signature of the Author _____

Accepted by _____
Coordinator, M.S. Degree Program Date

CHESTER F. CARLSON CENTER FOR IMAGING SCIENCE
COLLEGE OF SCIENCE
ROCHESTER INSTITUTE OF TECHNOLOGY
ROCHESTER, NEW YORK

CERTIFICATE OF APPROVAL

M.S. DEGREE THESIS

The M.S. Degree Thesis of Fu Jiang
has been examined and approved by the
thesis committee as satisfactory for the
thesis required for the
M.S. degree in Imaging Science

Dr. Carl Salvaggio, Thesis Advisor

Dr. Emmett Ientilucci

Dr. Aaron Gerace

Date

Evaluation of Stray Light Correction for the Thermal Infrared Sensor (TIRS) from Landsat 8

by

Fu Jiang

Submitted to the
Chester F. Carlson Center for Imaging Science
in partial fulfillment of the requirements
for the Master of Science Degree
at the Rochester Institute of Technology

Abstract

The Thermal Infrared Sensor (TIRS) of Landsat 8 suffers from a *stray light issue*, where out of field-of-view (FOV) radiance reflects into the optical system and is recorded by the sensors. This is confirmed to be resulting from a defect in hardware of the third order lens. The *TIRS-on-TIRS* algorithm has been proposed to be an operational correction algorithm. This algorithm has an advantage of simple and easy processing steps. However, no comprehensive evaluation of the *TIRS-on-TIRS* algorithm has been performed to this point.

This thesis addresses a full evaluation of the performance of the algorithm with two datasets; especially associated with two artifacts related to the stray light issue: absolute radiometric error and "banding" effect. The dataset with truth, MODIS, demonstrates a good performance of the *TIRS-on-TIRS* algorithm in terms of both absolute radiometric error and the "banding" effect on all situations except for a higher absolute error for desert scenes after correction. The dataset without truth shows good consistency in terms of absolute radiometric error and no worse performance on the worst situations. Residual pattern error was found with band 11, but almost none in band 10. This should be taken into consideration for further calibration work.

Acknowledgements

Firstly, I would like to express my sincere gratitude to my advisor Prof. Carl Savalggio for the continuous support of my study and related research, for his patience, motivation, and immense knowledge. His guidance helped me in all the time of research and writing of this thesis. I could not have imagined having a better advisor and mentor for my study.

Besides my advisor, I would like to thank the rest of my thesis committee: Dr. Emmett Ientilucci, Dr. Aaron Gerace, and Dr. Matthew Montanaro, for their insightful comments and encouragement during the committee meetings over a whole semester, but also for the hard question which incentivized me to widen my research from various perspectives. And I would like to address my special thanks to Dr. Aaron Gerace and Dr. Matthew Montanaro during the whole research time. Without their help and guidance, this work cannot be finished. Their insight and critical thinking guided me through the whole year.

My sincere thanks also goes to Dr. John Kerekes, who provided me a lot help during the whole time in the department.

I thank my classmate for the help and funny activities during the three years.

Last but not the least, I would like to thank my family: my parents and to my sister for supporting me spiritually throughout writing this thesis and my life in general.

Contents

1 Introduction **1**

1.1 Problem to be Stated 1

1.2 Organization of Thesis 2

2 Background **4**

2.1 Overview of Thermal Infrared Sensor (TIRS) Instrument 4

2.2 Stray Light Artifacts of TIRS 7

2.2.1 "Banding" Effect 7

2.2.2 Absolute Radiometric Error 8

2.2.3 Special Lunar Collection and Optical Model 10

2.3 Stray Light Correction Methodology 12

2.3.1 Using External Sensor Data 13

2.3.2 Using Internal Data 15

2.4 Analysis of the *TIRS-on-TIRS* algorithm 17

2.4.1 Main Issues with the *TIRS-on-TIRS* algorithm 18

2.4.2 Other Issues 20

2.5 Summary 21

3 Methodology **22**

3.1 Methodology for Dataset with Truth 23

3.2 Methodology for Dataset Without Truth 24

3.2.1 Absolute Radiometric Error 24
3.2.2 Visual Examination of ″Banding″ Effect 24
3.3 Summary 25

4 Pre-Processing of MODIS **30**
4.1 MODIS Specification 31
4.2 Band Shape Adjustment 32
4.2.1 Procedure and Parameters 32
4.2.2 Result and Analysis 38
4.3 MODIS View Angle Study 41
4.3.1 Parameters in MODTRAN 42
4.3.2 Data Processing 43
4.3.3 Result and Analysis 44
4.4 Summary 61

5 Result and Analysis **63**
5.1 Dataset With Truth 63
5.1.1 Best Scenario 64
5.1.2 Landscape Issue 69
5.1.3 Cloud Issue 74
5.1.4 Residual Error from Best Scenario 79
5.2 Dataset Without Truth 80
5.2.1 Absolute Radiance Error Consistency 81
5.2.2 Visual Examination of ″Banding″ Effect 82
5.3 Summary 103

6 Summary and Future Work **108**
6.1 Summary 108
6.2 Future Work 111

Appendices **117**

A Band Shape Adjustment of GOES to TIRS **118**

B View Angle Study of GOES **121**

List of Figures

2.1 Illustration of a push broom system. 5
2.2 Illustration of the focal plane of TIRS, formed by three SCAs: band 10 (green block), band 11 (red block) and dark band (black block). . 6
2.3 Example of the "banding" effect (band 11 image of west of Los Angeles and Pacific Ocean) [7]. 8
2.4 Radiance difference between the TRIS data and the derived sensor-reaching radiance based on buoy in Lake Tahoe. Dash line shows the error of band 10 and solid line shows error of band 11 [6]. . . . 9
2.5 An example of special lunar collect [21]. Though the Moon is out of the FOV of TIRS some sensors (white in the figure) in SCA-A still read out signals as named ghost signal. 11
2.6 An example of stray light source locations of two different detectors. Left is one detector from SCA-C and right is one detector from SCA-B. Dots are the source locations from the optical model and open circles represent the source locations from the special lunar collection [18]. 12
2.7 Example of sampling radiance for pixel j, red dot. For pixel j in this image, the yellow arch represents the region contributing to *stray light radiance*. 14

2.8 Example of sampling radiance for pixel j using internal data algorithm. For pixel j in this image, the red line represents the approximation to yellow arch. L_i should be the radiance sampled of the pixels in red line. 16
2.9 Example of landscape issue: yellow arch represents the region contributing stray light effect for the pixel i. The red line represents the area where the landscape is water while corresponding area in yellow arch is land. 18
2.10 For pixel j, the material of out of FOV (yellow arch) is almost the same as pixels on the boundary of TIRS (red line). If the atmosphere of the two areas are different, the *TIRS-on-TIRS* algorithm will introduce some error. 19

3.1 Flowchart of steps for evaluate the *TIRS-on-TIRS* algorithm with truth. 26
3.2 Flowchart of steps for evaluate *TIRS-on-TIRS* algorithm with no truth on absolute radiometric error. 26
3.3 Flowchart of steps for evaluate the *TIRS-on-TIRS* algorithm with no truth on "banding" effect. 26

4.1 Relative Sensor Response (RSR) of band 31, 32 of MODIS and TIRS. 33
4.2 Emissivity plot of the materials, snow, water, sand and vegetation (conifer and tree). The solid line is the sensor response window of band 31 and 32. 35
4.3 Resample sensor response: Left is the original sensor response data and right is the resampled (0.01 μm) sensor response. Roughly the sensor reponse of TIRS is upsampled from 0.05 μm to 0.01 μm and that of MODIS is downsampled from 0.003 μm to 0.01 μm. 37

4.4 Example of simulated TOA spectral radiance from MODTRAN. Four different color lines stand for four different water vapor scalars as indicated by the legend in the plot. Other symbols: black dot line is the RSR of band 10, black solid line is the RSR of band 31, blue dot line is the RSR of band 11, blue solid line is the RSR of band 32. 38
4.5 Plots for linear regression of *Band 10 Vs Band 31* (A), and *Band 11 vs Band 32* (B). Blue stars are the original data and red line is the best fit-in function. C, Plot of $Rad_{B10} - Rad_{B31}$ (red diamond), $Rad_{B10} - f(Rad_{B31})$ (blue star). D, Plot of $Rad_{B11} - Rad_{B32}$ (red diamond), $Rad_{B11} - f(Rad_{B32})$ (blue star). Here f is the best fit-in function. . . . 40
4.6 Plot for simulated TOA spectral radiance of view angle from 0° to 60° indicated as different line type or color. The solid black lines show the RSR of band 31 and 32. The parameters used are: water, 300 K, midlatitude summer atmosphere model, 1.0 water vapor scalar (default water vapor). 44
4.7 *Normalized Radiance vs View Angle* for different materials. Plots of **band 31** of sand (A), water (B) and snow (C). Plots of **band 32** of sand (D), water (E) and snow (F). In each plot, horizontal axis is view angle (0° to 60°) and vertical axis is normalized radiance. First row is for band 31 and second row is for band 32. First column is sand, second column is water and last column is snow. Each subplot contains 312 contours. 47
4.8 Plots of *Normalized Radiance vs View Angle* for **band 31** of different *black-body temperature*: 220 K (A), 240 K (B), 270 K (C), 280 K (D), 310 K (E), and 340 K (F). Red dash line is the average. Each subplot contains 72 contours. 48

4.9 Plots of *Normalized Radiance vs View Angle* for **band 32** of different *black-body temperature*: 220 *K* (A), 240 *K* (B), 270 *K* (C), 280 *K* (D), 310 *K* (E), and 340 *K* (F). Red dash line is the average. Each subplot contains 72 contours. 49
4.10 Plots of all six atmosphere models (**band 31**): tropical model (A), mid-latitude summer model (B), mid-latitude winter model (C), subarctic summer model (D), subarctic winter model (E), and US standard 1976 model (F). Each subplot contains 156 different combinations. 50
4.11 Plots of all six atmosphere models (**band 32**): tropical model (A), mid-latitude summer model (B), mid-latitude winter model (C), subarctic summer model (D), subarctic winter model (E), and US standard 1976 model (F). Also each subplot contains 156 different combinations. 51
4.12 Plots of four different water vapor scalars for **band 31**. Each subplot includes the same water vapor scalar for all six different atmosphere model (shown in six different linetypes): 0.5 water vapor scalar (A), 1.0 water vapor scalar (B), 1.5 water vapor scalar (C), and 2.0 water vapor scalar (D). The meanings of the numbers in each subplot are: '1' is tropical model, '2' is mid-latitude summer model, '3' is mid-latitude winter model, '4' is subarctic summer model, '5' is subarctic winter model, and '6' is US standard 1976 model. 53
4.13 Plots of four different water vapor scalars for **band 32**: 0.5 water vapor scalar (A), 1.0 water vapor scalar (B), 1.5 water vapor scalar (C), and 2.0 water vapor scalar (D). Numbers in each subplot share the same meanings as it in Figure 4.12. 54

4.14 Plots of upwell radiance (green line), surf radiance (direct radiance, blue line) and total radiance (TOA radiance, red line) at view angle at 0° (A), 20° (B), 40° (C) and 60° (D). The settings are water, 300 K, midlatitude summer atmosphere model and default water vapor. . 56
4.15 Preview of the chosen MODIS scene around the equator (red line). 58
4.16 Plots of the uplimit and the downlimt of *Normalized Raidance vs View Angle* for operational example of band 31 (left) and band 32 (right). 59
4.17 Plots of results of applying the up-limit and the down-limit in Figure 4.16 for band 31 (left) and band 32 (right). Several different types of lines are: original GOES, shifted GOES, original MODIS and corrected MODIS (up-limit and down-limit). 59
4.18 *Normalized Radiance vs View Angle* for snow scene situation, with 0.05 cm, 0.07 cm and 0.09 cm water vapor, subarctic summer atmosphere model and aubarctic winter atmosphere mdoel. The first row is band 31 and the second row is band 32. From left to right are 230 K, 240 K, 250 K and 260 K for blackbody temperature setting. The red line is *1.02* and the cyan line is *0.99*. 61

5.1 Example of best scenario. Left is the three-layer image: red background is MODIS, white area is TIRS. Right is the preview of the geographic location of this scene. White dashed box shows area contributing to the *stray light radiance* of the red line across the scene. 65
5.2 Plots of $TIRS_{orig} - MODIS_{adjust}$ (red), $TIRS_{correct} - MODIS_{adjust}$ (green) of band 10 (left), and band 11 (right). $TIRS_{orig}$ is the original TIRS, $TIRS_{correct}$ is the corrected TIRS using the *TIRS-on-TIRS* algorithm, and $MODIS_{adjust}$ is the MODIS data after applying the band shape adjustment. 65

5.3 Left is the mean changes for band 10 (red circle: $TIRS_{orig}-MODIS_{adjust}$, blue star: $TIRS_{correct} - MODIS_{adjust}$). Right is the same for band 11. *TIRS* in the legend means original TIRS and *SLC* is *Stray Light Corrected*. 67
5.4 Left is the standard deviation changes for band 10(red circle: $TIRS_{orig}-MODIS_{adjust}$, blue star: $TIRS_{correct} - MODIS_{adjust}$). Right is the same for band 11. 68
5.5 Left shows the screenshot of the three-layer image. Right is the geographic of the profile. 71
5.6 Plots of $TIRS_{orig} - MODIS_{adjust}$ (red), $TIRS_{correct} - MODIS_{adjust}$ (green) of band 10 (left) and band 11 (right). 71
5.7 Left is mean changes for band 10 (red circle: original, blue star: corrected). Right is the same for band 11. 72
5.8 Left is the mean changes for band 10 (red circle: original, blue star: corrected). Right is the same for band 11. 73
5.9 Left is the three-layer image of the example as well as previous example. Right is the geographic situation of this example. 75
5.10 Plots of $TIRS_{correct} - MODIS_{adjust}$ (green line), $TIRS_{orig} - MODIS_{adjust}$ (red line) of band 10 (left) and band 11 (right). 75
5.11 Red circle: mean of ($TIRS_{orig} - MODIS_{adjust}$), blue star: mean of ($TIRS_{correct} - MODIS_{adjust}$). Left is band 10 and right is band 11. . . . 77
5.12 Red circle: standard deviation of ($TIRS_{orig} - MODIS$), blue star: standard deviation of ($TIRS_{correct} - MODIS$). Left is for band 10 and right is band 11. 78
5.13 Residual error of band 10 (left) and band 11 (right). 79
5.14 Left is the mean changes for band 10 (red star: dataset with truth, blue circle: dataset without truth). Right is the same for band 11. . 81

5.15 Geographic location preview for LC82230852015054LGN00 (**A**). Landscape issue shows in the left. Profile plots of band 10 (B) and 11 (C). 83
5.16 Geographic location preview for LC82050322014133LGN00 (A). Landscape issue shows on the right. Profile plots of band 10 (B) and 11 (C). 85
5.17 Geographic location preview for LC81960312015041LGN00 (A). Landscape issue shows on the left. Profile plots of band 10 (B) and 11 (C). 86
5.18 Geographic location preview of LC81910212015230LGN00 (A). Landscape issue shows on both the left and right. Profile plots of band 10 (B) and 11 (C). 87
5.19 Geographic location preview of LC81600702015253LGN00 (A). Landscape issue shows on the right. Profile plots of band 10 (B) and 11 (C). 88
5.20 Geographic location preview of LC81600702015221LGN00 (A). Landscape issue shows on the right. Profile plots of band 10 (B) and 11 (C). 89
5.21 Geographic location preview of LC81600532014170LGN00 (A). Landscape issue shows on the left. Profile plots of badn 10 (B)and 11 (C). 90
5.22 Geographic location preview of LC81160762015281LGN00 (A). Landscape issue shows on the right. Profile plots of band 10 (B) and 11 (C). 92
5.23 Geographic location preview of LC80300162015222LGN00 (A). Landscape issue shows on the left. Profile plots of band 10 (B) and 11 (C). 93

5.24 Stacked image of GOES and TIRS of the cloud-issue example as LC80150372014322LGN00 (left), and the no-cloud-issue example as LC80150372014114LGN00 (right). The small images show the geographic situation. 94
5.25 Profile plots of band 10 (A) and 11 (C) of LC80150372014322LGN00, and band 10 (B) and 11 (D) of LC80150372014114LGN00. Red lines are the original TIRS and blue lines are the corrected TIRS. 95
5.26 Stacked image of GOES and TIRS of the cloud issue example as LC80150372016120LGN00 (left), and the no cloud isseue examle as LC80150372014114LGN00 (right). Small image shows the geographic location of the scene presenting slight landscape issue on the left side. 96
5.27 Profile plots of band 10 (A) and 11 (C) of LC80150372016120LGN00, and band 10 (B) and 11 (D) of LC80150372014114LGN00. Red lines are the original TIRS and blue lines are the corrected TIRS. 97
5.28 Stacked image of GOES and TIRS of the cloud-issue example as LC80200392016219 (left), and the no-cloud-issue example as LC80200392016283LGN00 (right). Small image shows the geographic situation. 99
5.29 Profile plots of band 10 (A) and 11 (C) of LC80200392016219LGN00, and band 10 (B) and 11 (D) of LC80200392016283LGN00. Red lines are the original TIRS and blue lines are the corrected TIRS. 100
5.30 Stacked image of GOES and TIRS of the cloud issue example LC80240402014017LGN00 (left), and the no cloud issue example as LC80240402014289LGN00 (right). Small image shows the geographic situation. 101
5.31 Profile plots of band 10 (A) and 11 (C) of LC80240402014017LGN00, and band 10 (B) and 11 (D) of LC80240402014289LGN00. Red lines are original TIRS and blue lines are corrected TIRS. 102

A.1 Relative Sensor Response (RSR) of band 4 of GOES 15 and band 10, 11 of TIRS. 119
A.2 Plots of the linear regression of band adjustment function between band 4 of GOES and band 10 of TIRS (A), and between band 4 of GOES and band 11 of TIRS (B). Plots of the error before and after linear regression for band 10 (C) and 11 (D). 120

B.1 Illustration of GOES effective view angle (left) and the relationship between effective view angle and sensor view angle (right). 122
B.2 Plot of *Effective View Angle vs Sensor View Angle*. 122
B.3 Effective view angle for GOES13 (left) and GOES15 (right) with coast line of the continents in green dot line. 123
B.4 Normalized radiance uncertainty for GOES 13 for ground temperature as 220 K (A), 250 K (B), 280 K (C), 290 K (D), 320 K (E) and 340 K (F). Red circle represents 0.05 and cyan circle represents 0.10. For all subplots, the horizontal axis is longitude and the vertical axis is latitude. 125
B.5 Normalized radiance uncertainty for GOES 15 for grounp temperature as 220 K (A), 250 K (B), 280 K (C), 290 K (D), 320 K (E) and 340 K (F). Red circle represents 0.05 and cyan circle represents 0.10. For all subplots, the horizontal axis is longitude and the vertical axis is latitude. 126

List of Tables

2.1 Spectral details of TIRS. 6

3.1 Landsat IDs of chosen scenes with truth. 27
3.2 Landsat IDs of chosen scenes without truth for absolute radiometric error. 28
3.3 Landsat IDs of chosen scenes without truth for ″banding″ effect of landscape issue. 28
3.4 Landsat IDs of chosen scenes without truth for ″banding″ effect of cloud issue. 29

4.1 Constant parameters used in MODTRAN simulations. 34
4.2 Variables used in Band Shape Adjust(MODIS) MODTRAN simulations 36
4.3 Corresponding simulated sensor reaching radiance of spectral plot in Figure 4.4. **wvs** stands for Water Vapor Scalar. 39
4.4 Parameters used in MODTRAN simulations for View Angle Study 42
4.5 Simulated sensor reaching radiance for spectral radiance plot in Figure 4.6. First two rows are the absolute radiance ($W/m^2 \cdot sr \cdot \mu m$) for band 31 and 32. The last two rows are the normalized radiances (unitless). 45

5.1 Statistic results of profile of best scenario example. Mean is the mean of radiance difference and standard deviation is that of radiance difference. Before refers to using original TIRS and after means using corrected TIRS. 66
5.2 Absolute radiance error for profiles of best scenario. (Numbers in parentheses are the numbers of profiles) 67
5.3 Standard deviations (”banding” effect) for profiles of best scenario. (Numbers in parentheses are numbers of profiles) 69
5.4 Statistic results of profiles of this landscape issue example. Notes are the same as in Table5.1. 72
5.5 Absolute radiance errors for profiles of landscape issue. (Numbers in parentheses are numbers of profiles) 73
5.6 Standard deviations (”banding” effect) for profiles of landscape issue. (Numbers in parentheses are numbers of profiles) 74
5.7 Absolute radiance errors for profiles of cloud issue. (Numbers in parentheses is numbers of profiles) 77
5.8 Standard deviations (banding effect) for profiles of cloud issue. (Numbers in parentheses is numbers of profiles) 78
5.9 Absolute radiometric error changes in percentage $(|Before|-|After|)/|Before|*100\%$, negative means absolute error increases after correction. (Numbers in parentheses is absolute error after correction, also convert to K unit.) 105
5.10 Standard deviation changes in percentage $(|Before|-|After|)/|Before|*100\%$, negative means standard deviation increases after correction.(numbers in parentheses is standard deviation of the profile after correction) 106

B.1 Uncertainty Look-Up Table (LUT) in unit of *Normalized Radiance*. . 124

Chapter 1

Introduction

Remote sensing, a field of study associated with extracting information about an object without coming into physical contact with it [1], is a widely used technology to collect data. Satellites are one of the most powerful remote sensing tools to collect data from space [2]. The Landsat program is the longest running satellite enterprise for acquisition of satellite imagery of Earth, mostly collecting images of the land. The first of the Landsat program satellites, Earth Resources Technology Satellite, was launched on July 23, 1972, then renamed to Landsat [3]. The most recent Landsat program, Landsat 8, as a collabration of the National Aeronautics and Space Administration (NASA) and the U.S. Geological Survey (USGS) was launched February 11, 2013 [4]. Landsat 8 carries two instruments: the Operational Land Imager (OLI) sensor with 8 bands and the Thermal Infrared Sensor (TIRS) with two thermal bands [5].

1.1 Problem to be Stated

The Thermal Infrared Sensor (TIRS) has been showing good performance in terms of noise and stability [6]. Despite this, a ”banding” effect and absolute radiometric

error have been found associated with TIRS data that varies from scene to scene. The "banding" effect refers to the low frequency changes across the whole focal plane, and absolute radiometric error is the above noise error after the regular radiometric calibration of TIRS. After exploration, stray light; radiance from out of field-of-view (FOV) reflected onto detectors, is confirmed to be the reason causing both artifacts [7]. In the following, radiance from out of field of view (FOV) reflected onto the detector will be termed **stray light radiance**.

Two correction algorithms have been proposed and explored: using an external data algorithm and using an internal data algorithm. Using an external data algorithm requires data from an instrument different from TIRS to correct *stray light radiance* while using internal data algorithm only needs the data from the TIRS itself to correct *stray light radiance*, [8]. Using an internal data algorithm is referred to as the **TIRS-on-TIRS** algorithm. The details of how the two algorithms work will be described in Chapter 2. Using an external data algorithm has several obvious disadvantages: large computations including accessing external data, format conversion, error caused by time difference between collection of external data and collection of TIRS data; multiple-external datasets are necessary in order to correct the TIRS scene globally [8]. The advantage of using an external data algorithm is the expected high level of precision that may be obtained. WHen using an internal data algorithm, the biggest advantage is that the disadvantages in using external data algorithm do not exist as all data coming from the TIRS itself. The disadvantage would be the unknown precision. Though several examples already demonstrated the feasibility of using an internal data algorithm [6], there is still a lack of a comprehensive evaluation of using an internal data algorithm.

1.2 Organization of Thesis

In this thesis, the goal is to provide a comprehensive evaluation of the **TIRS-on-TIRS** algorithm. Two datasets will be used: dataset with truth and dataset

without truth. Correspondingly, two methodologies will be applied. MODIS will provide the truth for the first dataset. The thesis is organized as follows: Chapter 2, background information will be presented including knowledge of TIRS, Stray Light artifacts, Stray Light correction methodologies, and analysis of the **TIRS-on-TIRS** algoirthm; Chapter 3, methodologies used to evaluate the performance of the **TIRS-on-TIRS** algorithm will be described; Chapter 4, pre-processing of MODIS data will be explained; Chapter 5 will present results and analyses; Chapter 6 will focus on a summary and future work.

Chapter 2

Background

This chapter will introduce the necessary background information: 1) overview of the TIRS instrument: band information and the structure of the focal plans; 2) stray-light artifacts: "banding" effect and absolute radiometric error; 3) stray light correction methodologies: methodology of using an external data algorithm and using an internal data algorithm (*TIRS-on-TIRS* algorithm); 4) analysis of *TIRS-on-TIRS* correction algorithm: two main issues associated with *TIRS-on-TIRS* algorithm, will be discussed.

2.1 Overview of Thermal Infrared Sensor (TIRS) Instrument

Landsat 8 is a typical pushbroom system. Figure 2.1 is an illustration of this type of system. A pushbroom system reads in one row of data at a time, then moves forward, reads another row of data and so on. Correspondingly, the sensors on the focal plane of a pushbroom system can be arranged in two ways: a long continuous array of sensors or several arrays of sensors staggered one by one. Sensors in TIRS are formed utilizing the staggered approach.

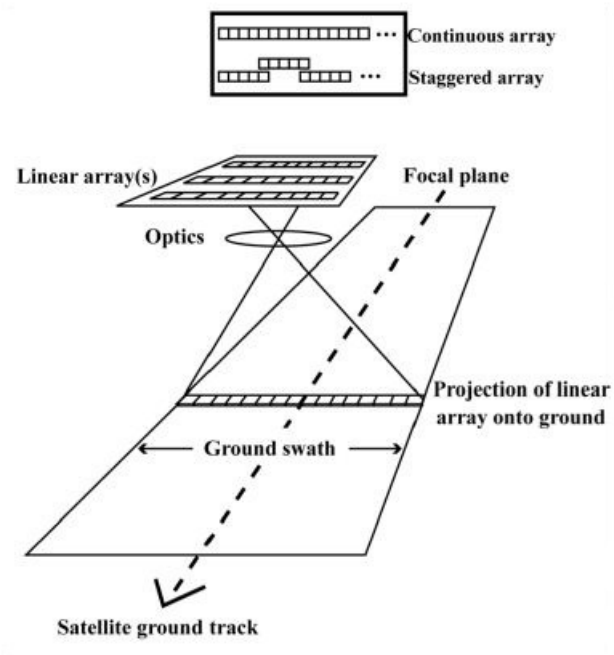

Figure 2.1: Illustration of a push broom system.

The focal plane of TIRS is formed by three arrays of Quantum Well Infrared Photodetector (QWIP) [9]. Each array is called Sensor Chip Assemblies (SCA). SCAs are staggered one by one as shown in Figure 2.2. They are named as SCA-3, SCA-1 and SCA-2 in the figure, or SCA-A, SCA-B and SCA-C. Each SCA consists of 512*640 pixels. SCA-A and SCA-B are offset slightly from SCA-C in the along-track direction by 300 pixels for band 10 and 200 pixels for band 11. Both SCA-A and SCA-B have about 28 pixels overlapping with SCA-C in cross-track direction [10]. The spectral interference filter, spectrally dispersing the incoming energy onto the sensors, can cover about 35 rows. Among the 35 rows, only one row in each band can generate a signal, providing the image product. Another row of each band is designed as back-up for the primary row. Some of the rows, depicted as black in the figure, totally block any outside energy and are used to

characterize the internal dark signal. Temperature of the whole focal plane is controlled by a cooler and is kept within within 0.01 K of 40 K [11]. Table 2.1 lists the spectral windows of the two bands. All TIRS products are available for browse and download in GloVis, EarthExplorer, and the LandsatLook Viewer [12–14].

Spectral Band	Wavelength (μm)	Ground Resolution (m)
Band 10	10.30 - 11.30	100
Band 11	11.50 - 12.50	100

Table 2.1: Spectral details of TIRS.

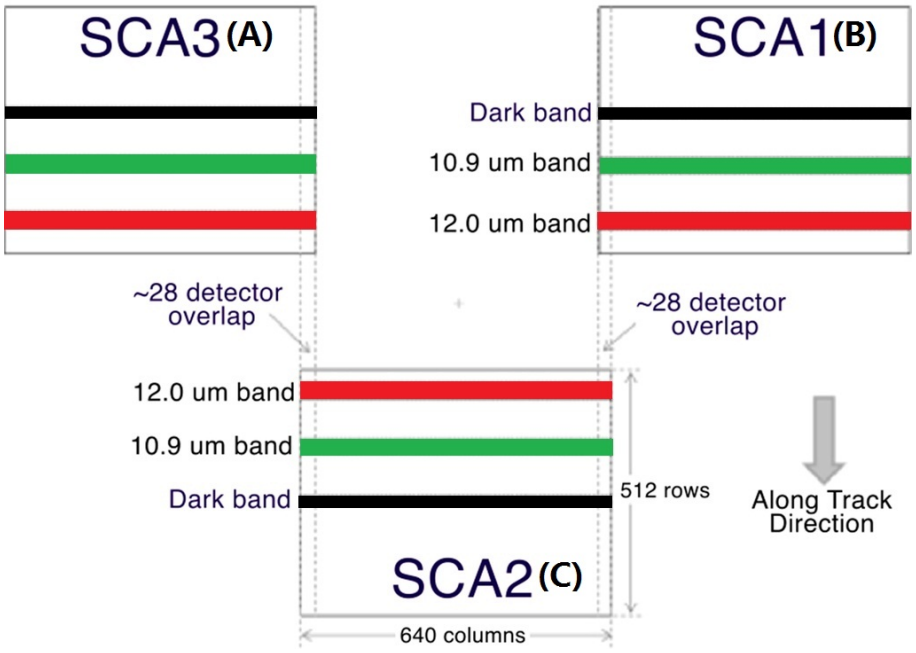

Figure 2.2: Illustration of the focal plane of TIRS, formed by three SCAs: band 10 (green block), band 11 (red block) and dark band (black block).

2.2 Stray Light Artifacts of TIRS

Of the two instruments carried by Landsat 8, Operational Land Imager (OLI) has been working well [15, 16], but there are two anomalous characteristics found from the Thermal Infrared Sensor (TIRS): ”banding” effect and absolute radiometric error. Special lunar collections confirms that the stray light issue results in the two characteristics [6]. Following the lunar collections, an optical model was built and analyzed by the NASA calibration team. The model further confirms that the defect is in hardware, and originally from the ring of the third-order lens, making it responsible for the two degradations observed.

2.2.1 ”Banding” Effect

The ”banding” effect is refered as the low frequency variation along the cross track direction (recall Figure 2.2) over the uniform area [10]. This was found to vary from scene to scene after the pre-launch calibration and regular on-orbit calibration [7, 17–19].

Figure 2.3 shows an example of the ”banding” effect. This is a band 11 image of an open sea area west of Los Angeles, CA, USA. Large open sea is usually considered as highly uniform thermal area on the earth. Therefore, the image is supposed to be highly uniform, however, there is obvious variance across the focal plane (cross track direction). As seen in the figure, the image can be divided into three parts, corresponding to the arrangement of the SCAs on the focal plane. Firstly, it is obvious that the average radiance of SCA2 in this example is higher than that of SCA1 and SCA3. In addition, within SCA3, the middle area has lower radiance than the surrounding regions. Within SCA2, the middle area has higher radiance than the edges. Variance of radiance level from position 1 to 5 is a vivid example of the ”banding” effect: radiance increases smoothly from position 1 to 2, a big up jump from position 2 to 3 on the boundary between SCA3 and SCA2, increasing gently from position 3 to 4, and a fall from position 4 to 5 on boundary

between SCA2 and SCA1. Again this low-frequency variation and the jump on the boundary of SCAs vary from scene to scene, which means the ”banding” effect is a scene-dependent phenomenon.

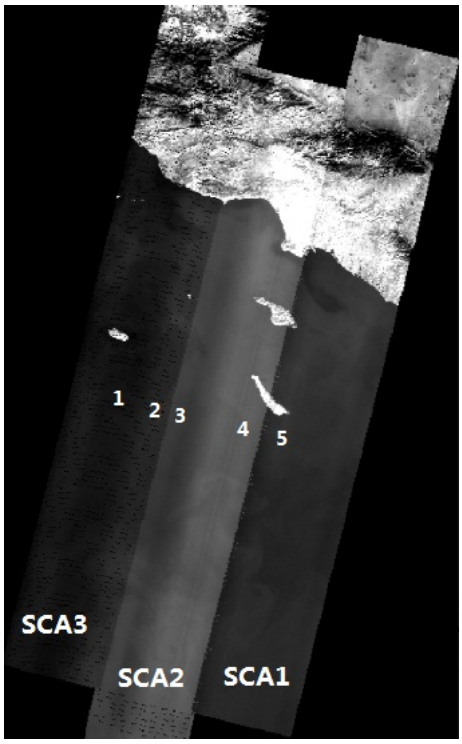

Figure 2.3: Example of the ”banding” effect (band 11 image of west of Los Angeles and Pacific Ocean) [7].

2.2.2 Absolute Radiometric Error

Another anomulous characteristic found with TIRS is absolute radiometric error. After the regular pre-launch and onboard calibration, above noise absolute error still exits [18]. Buoys in the body of water in the lake area and near shore open sea are used to measure the surface water temperature directly. Together with real-time atmosphere paramters, sensor-reaching radiance can be derived to compare

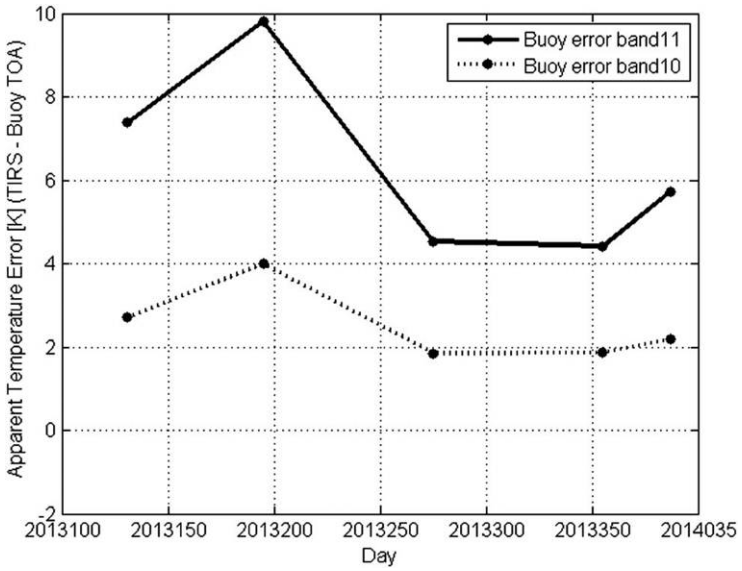

Figure 2.4: Radiance difference between the TRIS data and the derived sensor-reaching radiance based on buoy in Lake Tahoe. Dash line shows the error of band 10 and solid line shows error of band 11 [6].

to the data from a satellite instrument, like TIRS. This method has been used for absolute radiometric calibration for the thermal band of Landsat 5, 7 and 8 [19, 20]. Radiance from TIRS was found to be always higher than the derived sensor-reaching radiance. Additionaly, the error has seasonal effect, error is higher in the summer and lower in the winter [6]. Figure 2.4 gives an example of the error between TIRS and buoy derived radiance in Lake Tahoe. The horizontal axis is the date and vertical axis is the error between the TIRS data and the predicted data from the buoy. The error is higher in the summer, lower in the winter, and higher in band 11 than band 10 all the time.

2.2.3 Special Lunar Collection and Optical Model

With some further steps taken ruling out the stability of the instrument from contributing to "banding" effect and absolute radiometric error [7, 8, 18], radiance from out of the field-of-view (FOV) reflecting onto the sensors (stray light) is suspectted to be the reason causing the "banding" effect and the absolute radiometric error. Special lunar collection, turning the Landsat 8 toward Moon to collect data, confirmed that *stray light radiance* is the reason for the "banding" effect and the radiometric error [10]. The Moon is considered as a condense source, 0.5° as compared to 15° FOV of TIRS. When the Moon is put outside of FOV of TIRS, clear signal was recored by some detectors, which is not supposed to happen for a well designed instrument. Figure 2.5 is an example of the special lunar collection, where the Moon is out of FOV of TIRS while there are clear signals from some detectors in SCA-A. A complete lunar collection includes full list of read out signal when the Moon is put in all the possible location out of FOV. More details can be found in [10].

Based on the special lunar collection data, an optical model was built and fitted with the special lunar collection data by the calibration team of NASA. Finally the defect in ring of the third-order lens was found to be responsible for the two artifacts. The ring reflects out of the FOV radiance into the optical system, recorded by the sensors [6]. Also it was found that source location contributing to *stray light radiance* varies from detector to detector. However, the source location from the lunar collection is not exactly the same as the optical model was predicting. Figure 2.6 shows an example comparison between the lunar collection and the optical model. In this example, in general the source locations from the optical model align well with the special lunar collection while more source locations were predicted by the optical model. Again this is just an example of two detectors. The source locations vary from detector to detector.

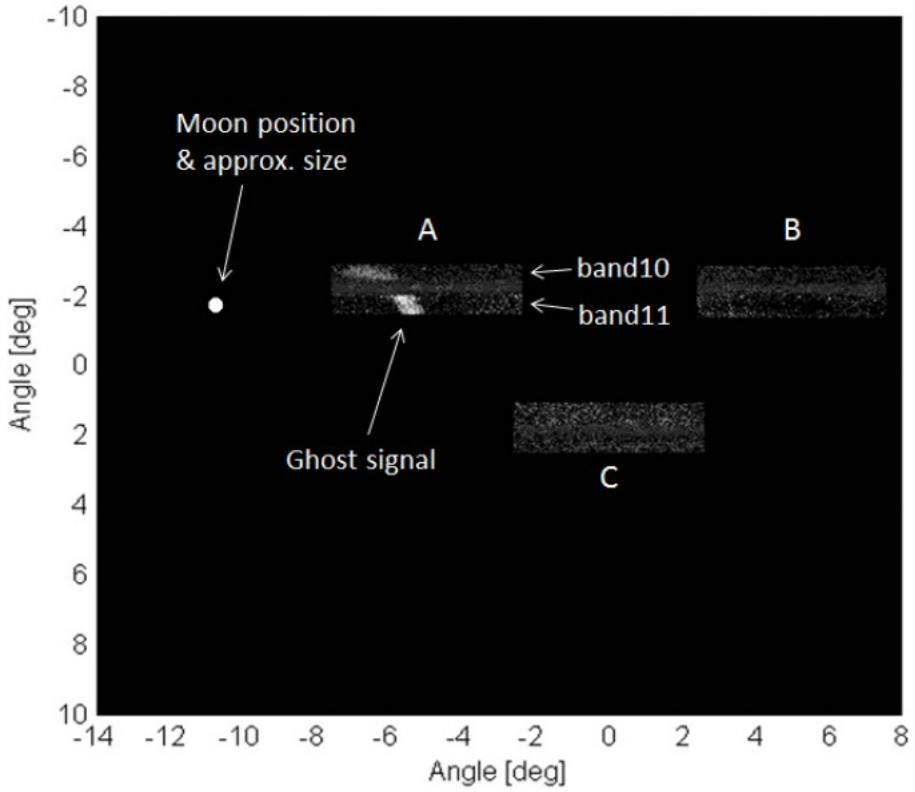

Figure 2.5: An example of special lunar collect [21]. Though the Moon is out of the FOV of TIRS some sensors (white in the figure) in SCA-A still read out signals as named ghost signal.

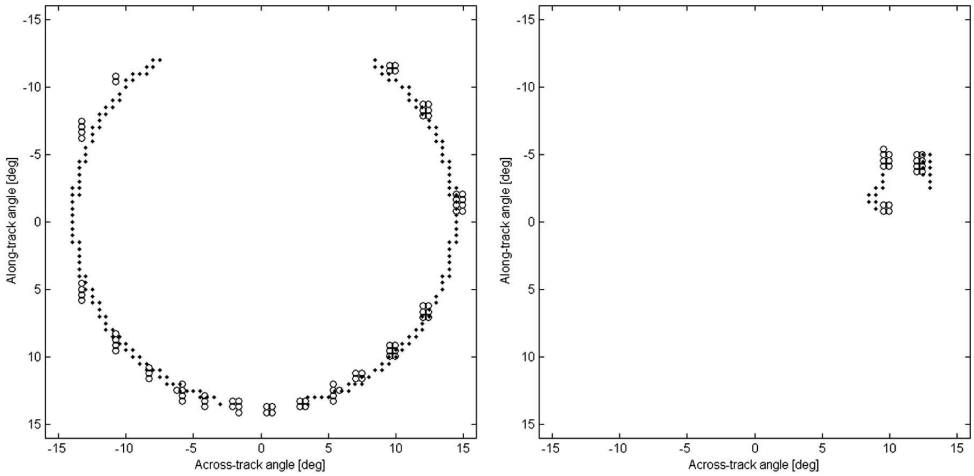

Figure 2.6: An example of stray light source locations of two different detectors. Left is one detector from SCA-C and right is one detector from SCA-B. Dots are the source locations from the optical model and open circles represent the source locations from the special lunar collection [18].

2.3 Stray Light Correction Methodology

Stray light radiance varies from detector to detector, in turn it varies from scene to scene. So the correction has to be pixel-based. The straightforward strategy is: calculating the *stray light radiance* for each detector, subtracting *stray light radiance* from the total radiance. In terms of acquiring *stray light radiance*, there are two different methodologies: using an external data algorithm and using an internal data algorithm.

Using an external data algorithm acquires radiances from all source locations contributing to the *stray light radiance* of each detector. While using an internal data algorithm will approximate the radiances from source locations with co-incident radiance from the boundary of TIRS. So using an internal data makes an assumption that the radiances along the boundary of TIRS are close to the radiances from source locations. For both methodologies, there are two steps:

deriving the parameters for each detector and implementing the algorithm. Deriving the parameters is building the relationship between the radiances from source locations and the *stray light radiance* for each detector. Implementing the algorithm is applying the derived parameters onto each scene.

2.3.1 Using External Sensor Data

Derivation of Parameters for Each Detector

For deriving parameters for each detector, there are two sub-steps: 1) sampling and weighting the external sensor data based on the optical model; and 2) deriving parameters through linear regression. Figure 2.7 shows an example of sampling the external sensor data. For the red dot pixel, j, the yellow arch approximately highlights the region contributing to the *stray light radiance* for this. The *stray light radiance*, $Rad_{straylight}$, can be written as $f([\sum(L_i * w_i)])$, where sample radiance L_i is radiance sampled along the yellow arch at each source location and w_i is the corresponding weight provided by the optical model.

The function f is found to be a linear relationship [6]. For each detector, a number of chosen pixels with the known truth radiance Rad_{truth}, will be used to derive linear function f. Equation 2.1 shows the method, where Rad_{truth} is the known truth radiance, Rad_{total} is radiance recorded by TIRS, $\sum(L_i * w_i)$ is the sum of weighted radiance, and a, b, are unknown linear parameters. With the chosen pixels providing known Rad_{total}, Rad_{truth}, $\sum(L_i * w_i)$, linear regression between $Rad_{total} - Rad_{truth}$ and $[\sum(L_i * w_i)]$ will yield a and b for each detector.

Band 31 and 32 from MODIS are the typical external sensor data used as the truth to derive the parameters. A wide FOV instrument will usually be used for sampling source locations in the out of FOV region.

$$Rad_{total} - Rad_{truth} = a * [\sum(L_i * w_i)] + b \tag{2.1}$$

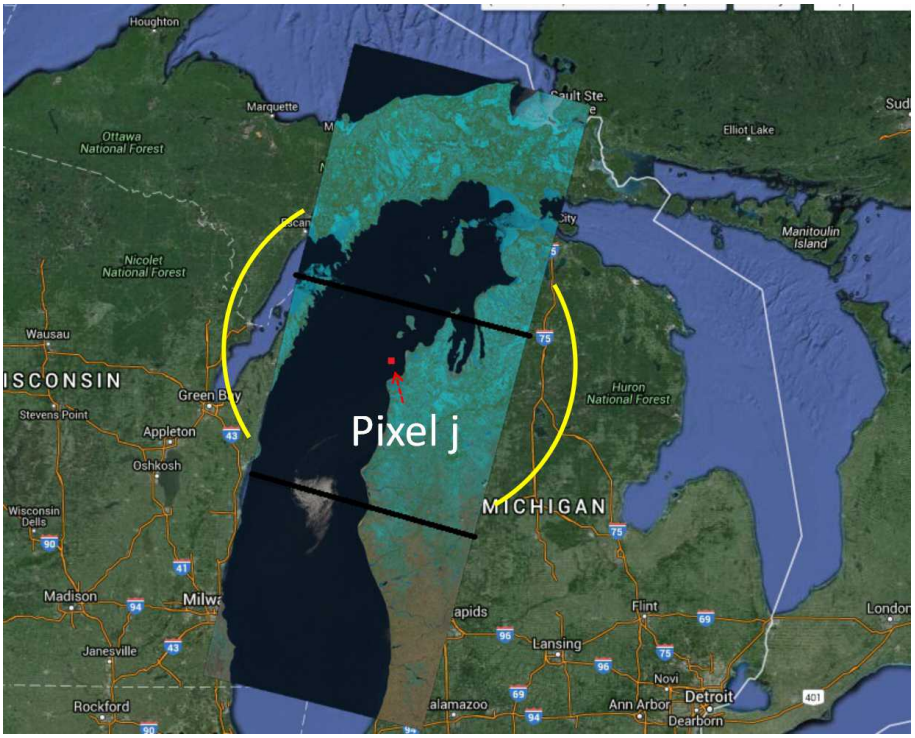

Figure 2.7: Example of sampling radiance for pixel j, red dot. For pixel j in this image, the yellow arch represents the region contributing to *stray light radiance*.

Implement Correction Algorithm

With the derived parameters a and b, the algorithm can be implemented to correct for the *stray light radiance*. For each pixel, *stray light radiance*, $Rad_{stray-light}$ can be calculated according to Equation 2.2, where L_i is the sample radiance of source locations from the external sensor, w_i is the corresponding weight, and a adn b are the derived parameters for the corresponding detector.

$$Rad_{stray-light} = a * [\sum (L_i * w_i)] + b \tag{2.2}$$

Finally, subtract this *stray light radiance* from the total radiance giving the corrected radiance using Equation 2.3. For obtaining sample radiance, GOES can

provide L_i globally but not with high precision [6].

$$Rad_{corrected} = Rad_{total} - Rad_{stray-light} \tag{2.3}$$

2.3.2 Using Internal Data

Derive Parameters for Each Detector

Equation 2.4 is used to derive the parameters for each detector. Rad_{total} is the measured radiance from TIRS, Rad_{truth} is the truth radiance, a and b are linear parameters, L_i is the sample radiance along the boundary of TIRS, w_i is the corresponding weight. So the key difference from using an external data algorithm is that L_i is along the boundary of TIRS when using an internal data algorithm.

$$Rad_{total} - Rad_{truth} = a * [\sum(L_i * w_i)] + b \tag{2.4}$$

Figure 2.8 illustrates an example of obtaining sample radiance. For pixel j, the yellow arch is the region contributing to *stray light radiance* and it is the region where using an external data algorithm obtains *stray light radiance*. Using an internal data algorithm will utilize radiance along the boundary of TIRS, the red line, to obtain *stray light radiance*. L_i in Equation 2.4 is the sampled radiance along the red line, and is used as approximation to the radiance from the yellow arch. This approximation is made on pixel-wise, that is substituting each sample radiance from the yellow arch with a radiance from the nearest location on the red line. The weights, w_i, retain the same without any adjustment.

As the procedure using the external data algorithm, for each detector, a number of pixels will be selected to derive parameters. The chosen pixels should have known true radiance, Rad_{truth}, and be obtained from well-calibrated instrument data. Therefore for all of these chosen pixels, $\sum(L_i * w_i)$, Rad_{truth} and Rad_{total} are available. Then unknown parameters a and b can be obtained through linear regression. Again, these parameters are detector-based. So a and b should be

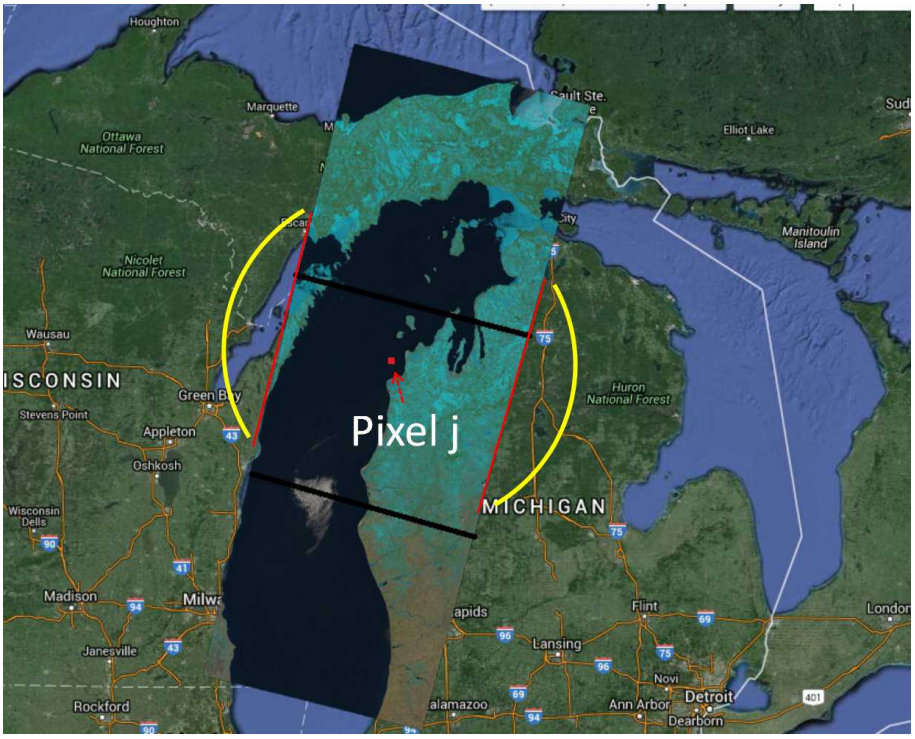

Figure 2.8: Example of sampling radiance for pixel j using internal data algorithm. For pixel j in this image, the red line represents the approximation to yellow arch. L_i should be the radiance sampled of the pixels in red line.

derived for each detector.

Implement Correction Algorithm

As with derived parameters for each detector, applying the algorithm would be the reverse procedure of deriving the parameters. For each pixel in the TIRS image, *stray light radiance*, $Rad_{stray-light}$, can be calculated through Equation 2.5, where L_i stands for the sampled radiance along the boundary of TIRS, w_i is the weight from optical model, a and b are the derived parameters from section above.

$$Rad_{stray-light} = a * [\sum (L_i * w_i)] + b \tag{2.5}$$

Then subtracting the stray-light radiance from the total radiance would give the corrected radiance as in Equation 2.6.

$$Rad_{corrected} = Rad_{total} - Rad_{stray-light} \tag{2.6}$$

More details of using the internal data algorithm is available in [6]. Through the following article, we will term using the internal data algorithm as the **TIRS-on-TIRS** algorithm.

2.4 Analysis of the *TIRS-on-TIRS* algorithm

The *TIRS-on-TIRS* algorithm simplifies the procedure to obtain data which reduces the computations and complexity dramatically compared to using the external data algorithm. Moreover, the *TIRS-on-TIRS* algorithm provides precise coincident data globally which is a big drawback for using the external data algorithm. When applying the algorithm with the derived parameters, the TIRS image itself can provide all the necessary data, while using the external data algorithm requires accessing near-coincident external data and image format conversion. Therefore, the *TIRS-on-TIRS* algorithm has a big advantage when implemented as an operational approach.

Along with the big advantage the *TIRS-on-TIRS* algorithm has, it may also introduce error, especially when the approximation is not accurate. Generally speaking, if the sensor-reaching radiance from out of the scene's FOV (recall yellow arch in Figure 2.8) can exhibit a large difference from the radiance on boundary of TIRS (recall the red line in Figure 2.8). There could be some error introduced by this approximation. This will be a key factor when the performance of the algorithm is evaluated. A lot of situations, geographic layout of the scene, that may introduce the radiance difference between the two area exist. Two examples will be referred to as: *landscape* and *atmosphere*.

2.4.1 Main Issues with the *TIRS-on-TIRS* algorithm

Landscape

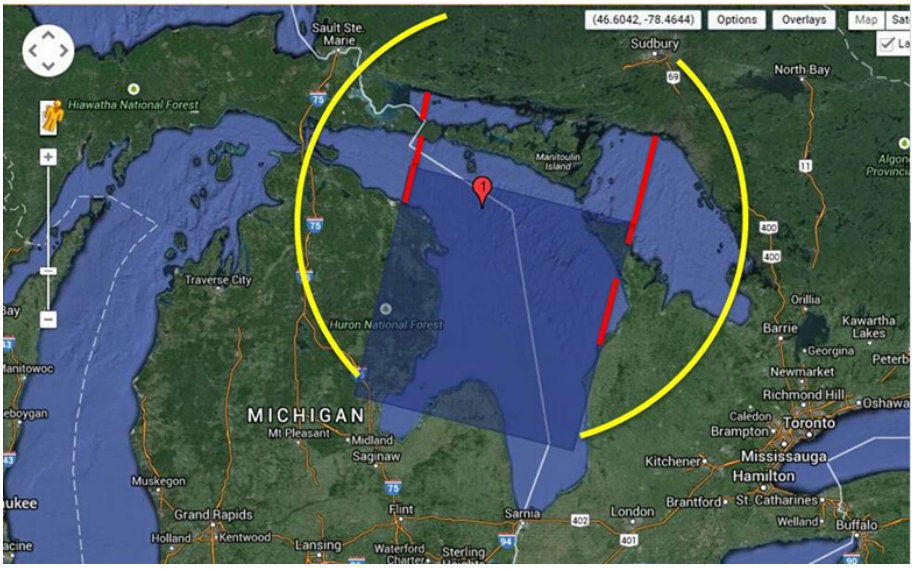

Figure 2.9: Example of landscape issue: yellow arch represents the region contributing stray light effect for the pixel *i*. The red line represents the area where the landscape is water while corresponding area in yellow arch is land.

Landscape issue is referred as the situations where the landscape of the outside of FOV is different from that on the boundary in TIRS. Different landscapes usually have different material properties and different temperature. These two differences will yield an incoming radiance difference between the two areas. The approximation made by the *TIRS-on-TIRS* algorithm brings some uncertain error, the *stray light radiance* can be underestimated or overestimated to some extent. As you might expect, this error is variant on pixel-wised bias. An example is shown in figure 2.9. Red line in the Figure is water while the corresponding part in out of FOV region (yellow arch) is land. As is known water usually has a lower temperature than land during daytime for many environments. Within the TIRS

spectral windows, these two materials have similar emissivities. Consequently, the pixel on the red line would have lower radiance than that along the yellow arch. Substituting the radiance of yellow arch with that of red line will underestimate the sampled radiance, hence underestimate the *stray light radiance*. As for how much the *TIRS-on-TIRS* algorithm underestimates the *stray light radiance*, it depends on the radiance difference between the red line area and corresponding part in yellow arch. Also this effect would vary from pixel to pixel even with the same scene. So, the landscape will add a pixel-wised nonuniformity error to the scene. We will term this situation as, the *landscape issue* in the remainder of this document.

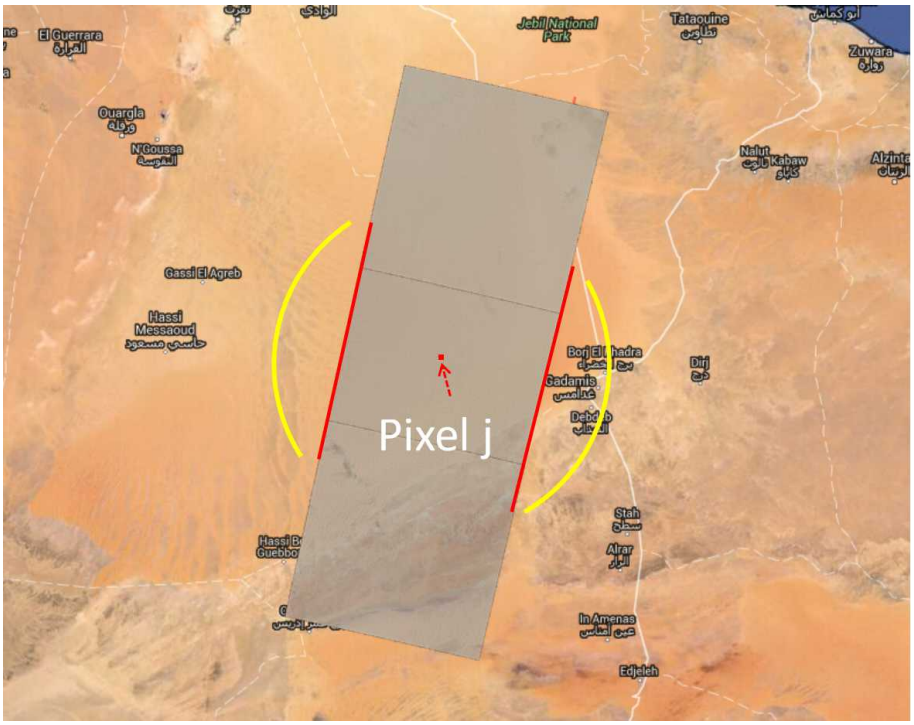

Figure 2.10: For pixel j, the material of out of FOV (yellow arch) is almost the same as pixels on the boundary of TIRS (red line). If the atmosphere of the two areas are different, the *TIRS-on-TIRS* algorithm will introduce some error.

Atmosphere (cloud)

In addition to the *landscape issue*, another common issue is the atmosphere issue. The atmosphere issue refers to situations that the outside of FOV region has the same material as the boundary of TIRS, but the atmospheric makeup of the two areas are different. The same materials will have similar properties, usually exhibit similar temperatures, in turn produce equivalent ground leaving radiances. From ground leaving to sensor reaching radiance, atmospheric conditions attenuate the signal. In homogeneous atmospheric conditions will result in different sensor reaching radiances for the same ground leaving radiances. For example, heavy cloud can reduce $9W/m^2 \cdot sr$ radiance to 3-4 $W/m^2 \cdot sr$. For example, the outside of FOV region contributing to *stray light radiance* of pixel, j, in figure 2.10 has the same material, sand, as the boundary of the TIRS field-of-view. If there is a significant difference in atmospheric conditions between the yellow arch and red line, a degree of error will also be introduced by the approximation. Considering the ground swath of TIRS, different atmospheric conditions are common: cloud-free on one side and cloudy on the other. This error will depend on the exact atmosphere situation. So this is also of pixel-wised concern. Clouds would be the main factor causing a difference in atmosphere. We will term this situation as the *cloud issue* in remainder of this document.

2.4.2 Other Issues

In addition to the two issues discussed so far and the combination, there are some additional situations which may introduce error. For example, in consideration of the sprawling ground coverage area of TIRS image (around $170km * 185km$), there is high chance that the radiance of the two areas are different from each other, simply due to geographic distance, even for the same material and atmospheric conditions. Moreover, besides the approximation error made by the *TIRS-on-TIRS* algorithm, the optical model is not perfect and deriving parameters will also introduce a degree of uncertainty. More about the optical model and deriving

these parameters can be found in [8].

Comparing the landscape issue and the cloud issue, cloud issue is high unpredictable while landscape issue usually occurs in specific locations, like in-land lakes and near shore areas. Both issues will be taken into consideration for evaluation of the *TIRS-on-TIRS* algorithm.

2.5 Summary

Two main artifacts, the "banding" effect and the absolute radiometric error, are introduced and illustrated. Special lunar collection confirmed that, the *stray light issue* exists. The optical model found that the defect in ring of the third order lens is the responsible contributing factor for the stray light issue. Two proposed correction methodologies, using external data and using internal data, were introduced and summarized. Using internal data, also called the *TIRS-on-TIRS* algorithm, makes an assumption by approximating the radiance from out of the FOV with the radiance along the boundary of TIRS. This assumption gives the *TIRS-on-TIRS* algorithm an advantage, simplifying the procedure and having coincident data, making itself highly operational possible.

If there is negligible difference between out of the FOV and the boundary of TIRS, it would be considered as the best scenario, which minimize the error from the assumption. But two main factors would bring in some error by the assumption, the landscape issue and the cloud issue. Both will bring in pixel-based nonuniformity error. The landscape issue will occur on some specific area but the cloud issue is unpredictable. Both will be taken into consideration for evaluation of the performance of the *TIRS-on-TIRS* algorithm.

Chapter 3

Methodology

There are two critical considerations when it comes to evaluating algorithm result, the truth data to compare with the measured data, and the criteria used for comparison. In terms of truth data, usually there are two ways: one is measuring the truth directly, which is used mostly in the lab, and the other is utilizing auxiliary existing data as the truth, which is used mostly for situations where the truth is difficult to measure directly. For TIRS, with its 100m by 100m resolution, it is difficult to measure the ground truth simultaneously when TIRS collects data. The buoy method discussed in Chapter 2 can only provide limited data and within limited areas. Therefore using the data from a well calibrated instrument would be a good choice to obtain enough truth data. For this study, the Moderate Resolution Imaging Spectrometer (MODIS) is chosen for this purpose. But not all data have corresponding truth data. So there is one methodology for the TIRS data with truth and there will be another methodology for the TIRS data without truth. The two methodologies will use slightly different analysis procedures and different metrics to evaluate the performance of the *TIRS-on-TIRS* algorithm.

3.1 Methodology for Dataset with Truth

For the dataset with truth, as stated above, MODIS is the chosen instrument for providing the truth. The details of MODIS will be stated and explored in the next chapter. As shown in the introduction of the stray light issue, there are two main artifacts brought by stray light: the ”banding” effect and the absolute radiometric error. Therefore two corresponding metrics will be used and examined to evaluate the performance of *TIRS-on-TIRS* algorithm. Mean radiance difference can represent the absolute radiometric error before and after correction. Then comparison between these two mean radiance differences can reveal the performance of the *TIRS-on-TIRS* algorithm. The standard deviation of the radiance difference of profile across the focal plane on a relatively high uniform area will demonstrate the ”banding” effect. Similarly comparison between the two standard deviations can present how the ”banding” effect changes. Radiance difference here refers to the difference between TIRS or corrected TIRS and the truth.
The general steps are shown in Figure 3.1:
Step 1: Obtain the corresponding original TIRS image, corrected TIRS image and MODIS image.
Step 2: Correct the three images to a geographically stacked layer.
Step 3: Extract multiple profiles across the focal plane using the three-layer image.
Step 4: Apply adjustment for MODIS. (details in next chapter)
Step 5: Calculate the mean and the standard deviation of ($TIRS_{orig} - MODIS_{adjust}$) and ($TIRS_{correct} - MODIS_{adjust}$).
Table 3.1 lists all the Landsat IDs of the chosen scene that have corresponding truth. Due to the limited available scenes, three profiles will be taken for each scene from northern, middle, and southern region of the scenes.

3.2 Methodology for Dataset Without Truth

In addition to the TIRS data with corresponding truth, TIRS data without truth also need to be examined. Because there is no truth to compare, the only available data would be original TIRS and corrected TIRS. Then only relative change can be computed and analyzed. This methodology also evaluates the performance in two parts: indirect evaluation of the absolute radiometric error and visual examination of the ”banding” effect.

3.2.1 Absolute Radiometric Error

For absolute radiometric error, no truth data makes direct evaluation of radiometric error impossible. The only remaining approach is an indirect evaluation method. We will evaluate the consistency of relative change between data with truth and data without truth. Here relative change means the radiance changes after the correction. If these two relative changes are consistent with each other, then the *TIRS-on-TIRS* algorithm has stable performance through both. Otherwise, the stability of the *TIRS-on-TIRS* algorithm needs to be examined. Figure 3.2 shows the flowchart for the absolute radiometric error analysis of the *TIRS-on-TIRS* algorithm for data without corresponding truth data. Table 3.2 lists the Landsat IDs of chosen scenes without truth for this indirect evaluation.

3.2.2 Visual Examination of ”Banding” Effect

”Banding”, low frequency signal across a uniform area, varies from scene to scene. So it is very difficult to examine the ”banding effect without truth in a quantitative way. But visual examination of the worst situations can be used to show how ”banding” changes in the worst cases indirectly. The data with the worst landscape issue will be used to present how the profile across the focal plane changes after correction. Theoretically, this should exhibit the worst performance

of the *TIRS-on-TIRS* algorithm. Again there is no truth data, this is just presenting and comparing profiles of the original TIRS and the corrected TIRS. Figure 3.3 shows a flowchart which is similar to the flowchart shown in Figure 3.2. Table 3.3 gives the Landsat IDs of the scenes used for this analysis. In addition, we will also investigate the cloud issue on ”banding” effect of the data without truth. We will find the scenes with cloud issue and the corresponding ones without cloud issue. The corresponding one has the same location as the one having cloud issue. Table 3.4 lists the cloud issue scenes on the first column and the corresponding no cloud issue scenes on the second column.

3.3 Summary

Two methodologies are proposed and stated: data with truth and data without truth. For the dataset with truth, two metrics are used: mean of radiance difference, corresponding with the absolute radiometric error, and standard deviation of radiance difference, corresponding with the ”banding” effect. These two metrics will show how the *stray light radiance* is removed by the *TIRS-on-TIRS* algorithm. For the dataset without truth, the evaluation will also take two approaches: indirect evaluation of the absolute radiometric error and visual examination of the ”banding” effect. Comparing the radiance change of this dataset, and that of the dataset with truth data, can show the stability of the *TIRS-on-TIRS* algorithm. For the ”banding” effect, scenes without truth with the most severe landscape issue will be chosen to show the worst performance of the *TIRS-on-TIRS* algorithm. A visual examination will show how the ”banding” effect changes after applying the *TIRS-on-TIRS* algorithm. Together, the dataset with truth can provide a quantitative result of the performance of the *TIRS-on-TIRS* algorithm and the dataset without truth can present the stability of the *TIRS-on-TIRS* algorithm and the worst cases.

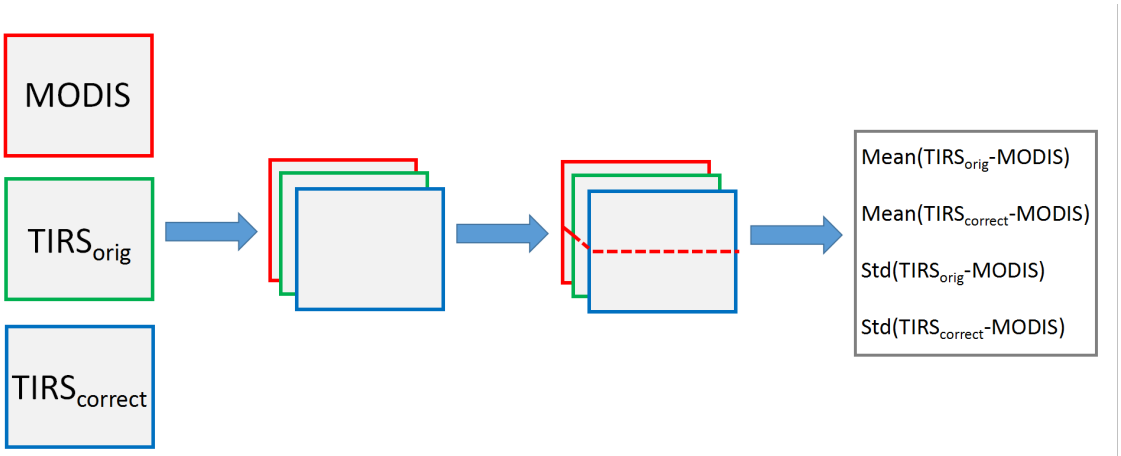

Figure 3.1: Flowchart of steps for evaluate the *TIRS-on-TIRS* algorithm with truth.

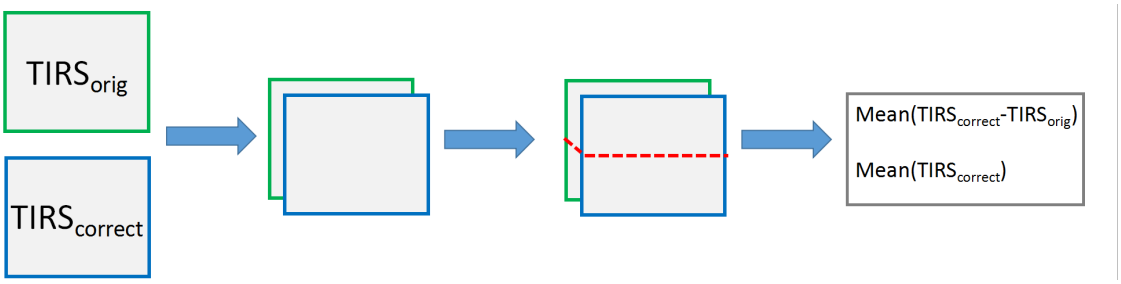

Figure 3.2: Flowchart of steps for evaluate *TIRS-on-TIRS* algorithm with no truth on absolute radiometric error.

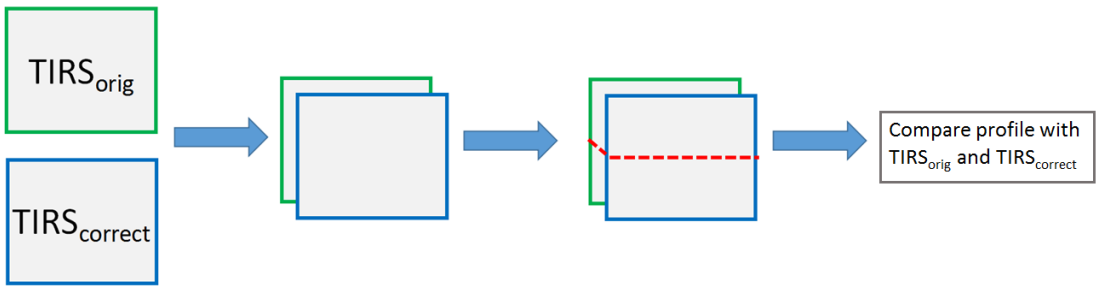

Figure 3.3: Flowchart of steps for evaluate the *TIRS-on-TIRS* algorithm with no truth on ”banding” effect.

Landsat ID	
LC81910462013088LGN01	LC81910472013088LGN01
LC81980482013089LGN01	LC81820402013089LGN01
LC81820412013089LGN01	LC81820422013089LGN01
LC81980462013089LGN01	LC81980472013089LGN01
LC80871132015045LGN00	LC80881132015052LGN00
LC80891132015043LGN00	LC80901132015035LGN00
LC80140032015126LGN00	LC80150042015117LGN00
LC80200022015120LGN00	LC80230022015125LGN00
LC80270022015121LGN00	LC80270032015121LGN00
LC80270042015121LGN00	LC80310032015117LGN00
LC80320022015124LGN00	LC80320032015124LGN00
LC80060112013093LGN01	LC80060122013088LGN03
LC80060122013093LGN01	LC80130072013089LGN01
LC80130082013089LGN01	LC80060712013088LGN02
LC80220402013088LGN01	LC81720422013090LGN01
LC81720432013090LGN01	LC81760362013088LGN01
LC81910332013088LGN01	LC80160382013087LGN01
LC80220282013088LGN01	LC80220292013088LGN01
LC80220302013088LGN01	LC80220312013088LGN01
LC81600422013088LGN01	LC81600422013088LGN01
LC81980342013089LGN01	LC82300472013089LGN01
LC82300482013089LGN01	

Table 3.1: Landsat IDs of chosen scenes with truth.

Landsat ID	
LC80060122015054LGN00	LC80130072014100LGN00
LC80130072015151LGN00	LC80130072015279LGN00
LC80130082014068LGN00	LC80140072015078LGN00
LC80160382014089LGN00	LC80160382014137LGN00
LC80220402013352LGN00	LC80220402014099LGN00
LC80220402015262LGN00	LC81720422015081LGN00
LC81720432015209LGN00	LC81720432015225LGN00
LC81720432015273LGN00	LC81760372014090LGN00
LC81760372014170LGN00	LC81910332015006LGN00
LC81910332015182LGN00	LC81910332015230LGN00
LC81910462014067LGN00	LC81910472014067LGN00
LC81980342015087LGN00	LC81980462014068LGN00
LC81980462015087LGN00	LC81980472014068LGN00
LC81980472015087LGN00	LC81980482014068LGN00
LC81980482015087LGN00	

Table 3.2: Landsat IDs of chosen scenes without truth for absolute radiometric error.

Landsat ID	
LC82230852016041LGN00	LC82230852015054LGN00
LC82050322014133LGN00	LC81960312016124LGN00
LC81960312015041LGN00	LC81910212015230LGN00
LC81600702015253LGN00	LC81600702015221LGN00
LC80300162015222LGN00	LC81600532014170LGN00
LC81160762016044LGN00	LC81160762015281LGN00
LC80300162016033LGN00	

Table 3.3: Landsat IDs of chosen scenes without truth for ”banding” effect of landscape issue.

Landsat ID	
LC80150372014322LGN00	LC80150372014114LGN00
LC80150372016120LGN00	LC80150372014114LGN00
LC80200392016219LGN00	LC80200392016283LGN00
LC80240402014017LGN00	LC80240402014289LGN00

Table 3.4: Landsat IDs of chosen scenes without truth for ”banding” effect of cloud issue.

Chapter 4

Pre-Processing of MODIS

Choosing an appropriate true radiance is very important for evaluating the performance of the *TIRS-on-TIRS* algorithm. Due to the ground size of TIRS, around $170\ km * 185\ km$ with $30\ m$ resolution, it is impossible to measure massive ground truth simultaneously. Moreover, in order to evaluate the "banding" effect quantitatively the definition requires truth across the whole focal plane.

As stated in last chapter, alternatively utilizing data from another well-calibrated instrument would be a good choice. When deciding what kind of remote sensing instrument should be used, some factors need to be taken into consideration.
1) The ground track of the remote sensing instruments should have overlap with that of TIRS, and have a wider FOV than that of TIRS.
2) Sensor response of the remote sensing instrument should be close to that of TIRS in order to reduce errors from differences in sensor response.
3) Time difference between the time when the TIRS scene is taken and that from when truth data is collected should be kept to a minimum. As is known, the sensor-reaching radiance changes as a function of time, due to the changes of the ground temperature and atmospheric conditions.
4) Spatial resolution and bit depth of the instrument should also be taken into consideration. Spatial resolution will have an effect when we stack the data with

the TIRS data. The bit depth will affect the quantization accuracy of the measured data.

Considering all four aspects above, MODIS (Terra) is the most suitable instrument. The reason for this will be discussed in the next section.

4.1 MODIS Specification

The Moderate Resolution Imaging Spectrometer (MODIS) instrument provides high radiometric sensitivity (12 bit) in 36 spectral bands, ranging in wavelength from $0.4\mu m$ to $14.4\mu m$. Among the 36 bands, two bands are imaged at a nominal resolution of 250 m at nadir, with five bands at 500 m, and 29 bands at 1 km [22]. MODIS is set at an orbit altitude, of 705 km, the same as TIRS. Additionally, a ±55-degree scanning pattern at the Earth Observation Satellite (EOS) orbit achieves a 2,330-km ground swath and provides global coverage every one to two days [22]. There are two MODIS flight instruments: the first MODIS flight instrument is integrated on the *Terra* spacecraft, which was launched successfully on December 18, 1991, and the second one is integrated on the *Aqua* spacecraft successfully launched, May 4, 2004 [22]. Both MODIS instruments offer an unprecedented look at terrestrial, atmospheric, and ocean phenomenology for a wide and diverse community of users throughout the world. More specifications of MODIS instrument can be found in [22].

Considering the four requirements to be used as truth data as analized above:
1: firstly, the ground track of *Aqua* overlaps with that of TIRS totally. But the track of TIRS is on the very periphery of *Terra*. However there are several days, when TIRS was on the center of *Terra*. These several days are those TIRS shifting to its operational orbit, called underflying days, from Mar 29, 2013 - Mar 31, 2013. Also when *Terra* and TIRS approach polar area, they overlap with each other.
2: Among the 36 bands, the sensor response of band 31 and 32 match that of TIRS band 10 and 11 very well.

3: Time difference between *Aqua* and TIRS varies from 45 minutes to several hours, while that between *Terra* and TIRS is around 10-25 minutes for underflying days. For the polar area, the time difference is within 15 – 40 minutes for *Terra*.
4: The spatial resolution is 1 km for both MODIS instruments. The data is 12-bit quantized, the same as TIRS. Both instruments are well-calibrated and have been used to calibrate other instruments in other studies [23–28].

Terra has its unique advantages, considering time difference and overlap. So MODIS (Terra) will be the chosen instrument, and providing truth. But before using MODIS as truth, there are two issues need to be investigated: band shape adjustment, correcting sensor response difference between MODIS and TIRS, and the effect of TIRS on the periphery of MODIS.

4.2 Band Shape Adjustment

Figure 4.1 shows the relative sensor response of band 31 and 32 of MODIS and band 10 and 11 of TIRS. Even with the high similarity between the sensor responses of band 31 and band 10, and between band 32 and band 11, it is necessary to investigate the effect of this difference and the necessity to correct for the difference. We will use the MODerate spectral resolution atmospheric TRANsmittance (MODTRAN) to simulate all kinds of atmospheric conditions, obtaining simulated sensor reaching radiance. These simulated radiances will be used to explore the effect of sensor response difference.

4.2.1 Procedure and Parameters

Procedure:
MODerate spectral resolution atmospheric TRANsmittance (MODTRAN) is going to be used to simulate atmospheric conditions. MODTRAN is a computationally rigorous radiation transfer algorithm that is used to model the spectral

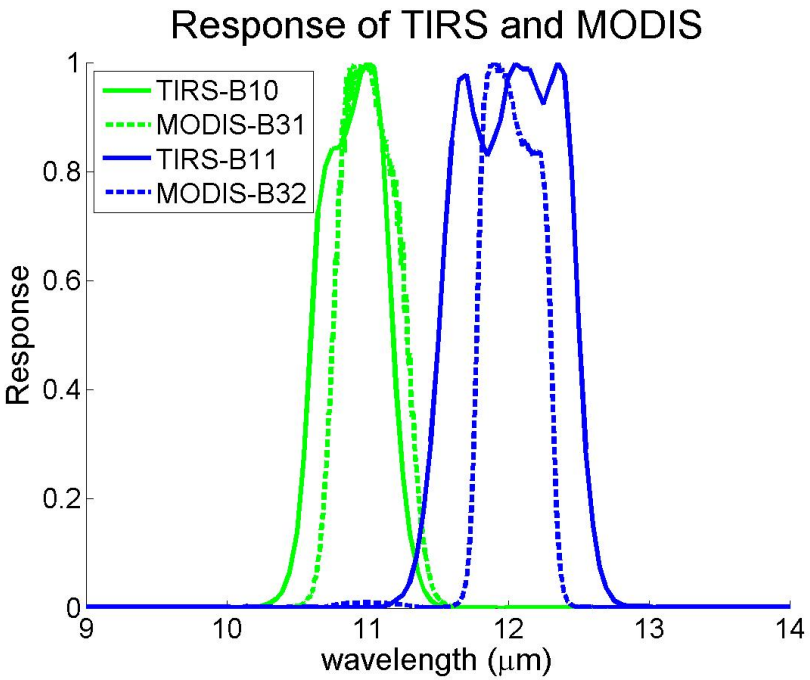

Figure 4.1: Relative Sensor Response (RSR) of band 31, 32 of MODIS and TIRS.

absorption, transmission, emission, and scattering characteristics of the atmosphere. MODTRAN models the atmosphere as a set of homogeneous layers [29]. User can use the internal model atmospheres (urban or rural, euqatorial or arctic, etc.) or provide the radiosonde data collected for a specific atmosphere as the characteristics of these layers. MODTRAN can calculate the atmospheric transmittance and radiance for wavelenth from 0 to $50,000\ cm^{-1}$ at a moderate spectral resolution, $2\ cm^{-1}$ ($20\ cm^{-1}$ in the ultraviolet). It has been used frequenctly to simulate atmospheric conditions obtaining the Top-of-Atmosphere (TOA) radiance from ground truth [20].

Following are the steps how MODTRAN will be used for band shape adjustment analysis.

Step 1: Set all the necessary parameters for MODTRAN. For example, altitude of

sensor is 705 km.
Step 2: Run MODTRAN to simulate the Top-of-Atmosphere (TOA) spectral radiance and calculate the sensor reaching radiance for different bands.
Step 3: Derive the function for band adjustment.

Parameters: In our analysis all parameters are of two types: constant parameters and variable ones. Constant parameters are those parameters that do not change for all simulations in MODTRAN and variable ones are those change. Constant parameters are listed in Table 4.1. Here we assume 0° sensor view angle (object on the nadir of the sensor). Both TIRS and MODIS orbit the earth at 705 km. Then altitude of sensor is set as 705 km. $9-14$ μm covers all four band spectral windows with 0.01 μm resolution.

Four variables used in simulation are: material, ground temperature (blackbody temperature), atmosphere model, water vapor scalar. Material and ground temperature will generate a range of ground leaving radiance, and atmosphere model with water vapor scalar will simulate most atmosphere situations. The reason the water vapor scalar is included is water vapor may vary a lot and water has absorption over $9-14$ μm. So for each atmosphere model, we will include several water vapor scalars. All the relevant MODTRAN variables are listed in Table 4.1.

Name	Value
Altitude of Object (km)	0
Altitude of Sensor (km)	705
Sensor View Angle (°)	0
Wave Range (μm)	9 - 14
Spectral Resolution (μm)	0.01

Table 4.1: Constant parameters used in MODTRAN simulations.

Three types of material are used during the analysis: snow, water and sand.

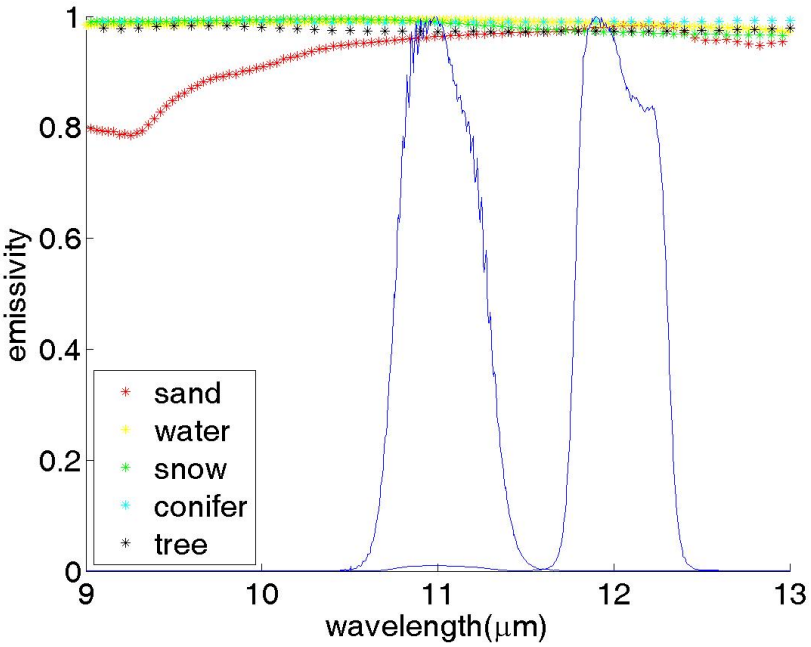

Figure 4.2: Emissivity plot of the materials, snow, water, sand and vegetation (conifer and tree). The solid line is the sensor response window of band 31 and 32.

High spectral resolution emissivity data of all three materials provided by MODIS UCSB material library are used [30]. Emissivities of the three materials are shown in Figure 4.2. It can be found that all three materials have very high emissivity within the band window, almost all higher than 95%. Snow, water and vegetation have similar emissivities as high as 98% across the wavelength range of interest. In the simulations, only three materials are used: water, snow and sand. But the result should still be valid for vegetation (conifer and tree in the plot) because the similarity between the emissivity of vegetation and that of water and snow.

Name	Value
Material	snow, water, sand
Black-body Temperature(K)	220-340(10 increment)
Atmosphere Models	Tropical Model Midlatitude Summer model Midlatitude Winter model Subarctic Summer model Subarctic Winter model US Standard 1976
Water Vapor Scalar	0.5, 1.0, 1.5, 2.0

Table 4.2: Variables used in Band Shape Adjust(MODIS) MODTRAN simulations

Black-body temperature (ground temperature) is set from 220 K to 340 K with 10 K increment, covering most terrestrial conditions. All six atmospheric models within MODTRAN are used. All combinations of the four variables are simulated through MODTRAN.

Calculate Sensor Reaching Radiance:
For each combination MODTRAN will generate a TOA spectral radiance. With TOA spectral radiance and sensor response function, sensor-reaching radiance can be computed based on Eq. 4.1, where λ_1, λ_2 are the $9\mu m$, $14\mu m$ in our case, L_λ

is the TOA spectral radiance and R_λ is sensor response function.

$$L = \frac{\sum_{\lambda_1}^{\lambda_2} L_\lambda * R_\lambda}{\sum_{\lambda_1}^{\lambda_2} R_\lambda} \tag{4.1}$$

We then need to align the resolution of R_λ with that of L_λ. Figure 4.3 shows the comparison between original *Relative Sensor Response* (RSR) and resampled relative sensor response. It can be found that the resampling step does not change the RSR function shape. This gives a more accurate result with high spectral resolution.

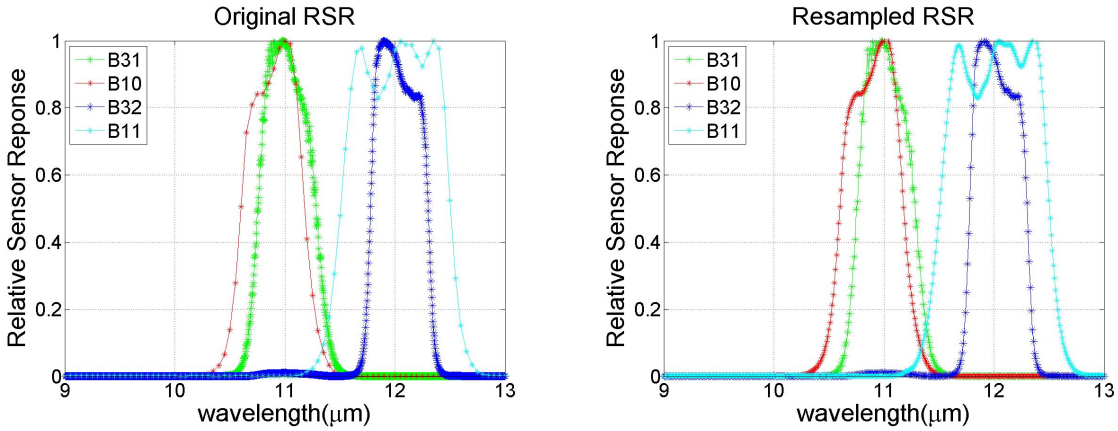

Figure 4.3: Resample sensor response: Left is the original sensor response data and right is the resampled (0.01 μm) sensor response. Roughly the sensor reponse of TIRS is upsampled from 0.05 μm to 0.01 μm and that of MODIS is downsampled from 0.003 μm to 0.01 μm.

4.2.2 Result and Analysis

Example

Figure 4.4 shows an example of the simulated TOA spectral radiance and Table 4.3 shows the integrated sensor reaching radiance based on Equation 4.1.

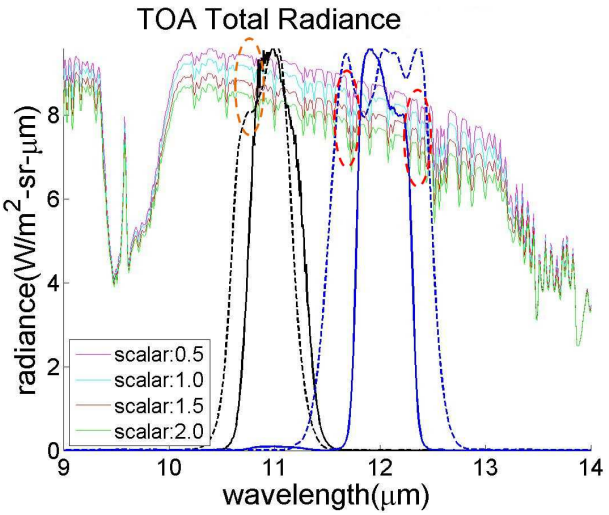

Figure 4.4: Example of simulated TOA spectral radiance from MODTRAN. Four different color lines stand for four different water vapor scalars as indicated by the legend in the plot. Other symbols: black dot line is the RSR of band 10, black solid line is the RSR of band 31, blue dot line is the RSR of band 11, blue solid line is the RSR of band 32.

In the plot, the brown dashed ellipse shows the spectral part which is only captured by band 10 but missed by band 31. The average radiance within the brown dashed ellipse area is higher than the average of the overlap between band 10 and band 31. Therefore, integrated radiance of band 10 should be higher than that of band 31. Also red dashed ellipses illustrate the spectral region which is only captured by band 11 but not by band 32. The two dips make radiance of band 11 lower than that of band 32. It is confirmed by data in Table 4.3.

Radiance($W/m^2 \cdot sr \cdot \mu m$)	0.5(wvs)	1.0(wvs)	1.5(wvs)	2.0(wvs)
Band 31	9.2236	8.9060	8.5101	8.1921
Band 32	8.5576	8.2207	7.8192	7.4776
Band 10	9.2779	8.9741	8.5869	8.2775
Band 11	8.4744	8.1258	7.7287	7.3849

Table 4.3: Corresponding simulated sensor reaching radiance of spectral plot in Figure 4.4. **wvs** stands for Water Vapor Scalar.

Comparing spectral radiance of different water vapor scalar shows that TOA radiance decreases from 10.2 μm to 13 μm when water vapor scalar increases, but it keeps constant from 9.2 μm to 10.2 μm. So water vapor has close continuous absorption across the band windows.

Linear Regression

There are **936** different combinations of parameters for MODTRAN simulations in total. 936 sets of simulated sensor-reaching radiance for band 10 and 11, and band 31 and 32 are calculated. Figure 4.5 shows the plot of all simulated sensor-reaching radiances and best linear fit-in functions for *band 10 vs band 31* and *band 11 vs band 32*.

First it is obvious that the band shape adjustment function should be a linear function. The gain of *band 10 vs band 31* is higher than 1 as shown in Figure 4.5 **A**. From Figure 4.5 C, the error without adjustment and with adjustment are calculated and plotted. It can be found that when Rad_{B31} is higher than 5.68, Rad_{B10} is higher than Rad_{B31}; when Rad_{B31} is lower than 5.68, Rad_{B10} is lower than Rad_{B31}. The *RMS* is 0.093 if there is adjustment but it can be reduced to 0.044 after the linear adjustment. Especially for high radiance, the maximum error is reduced from around 0.28 to 0.15 after the linear correction.

For *band 11 vs band 32* the gain of the function is lower than 1 as shown in

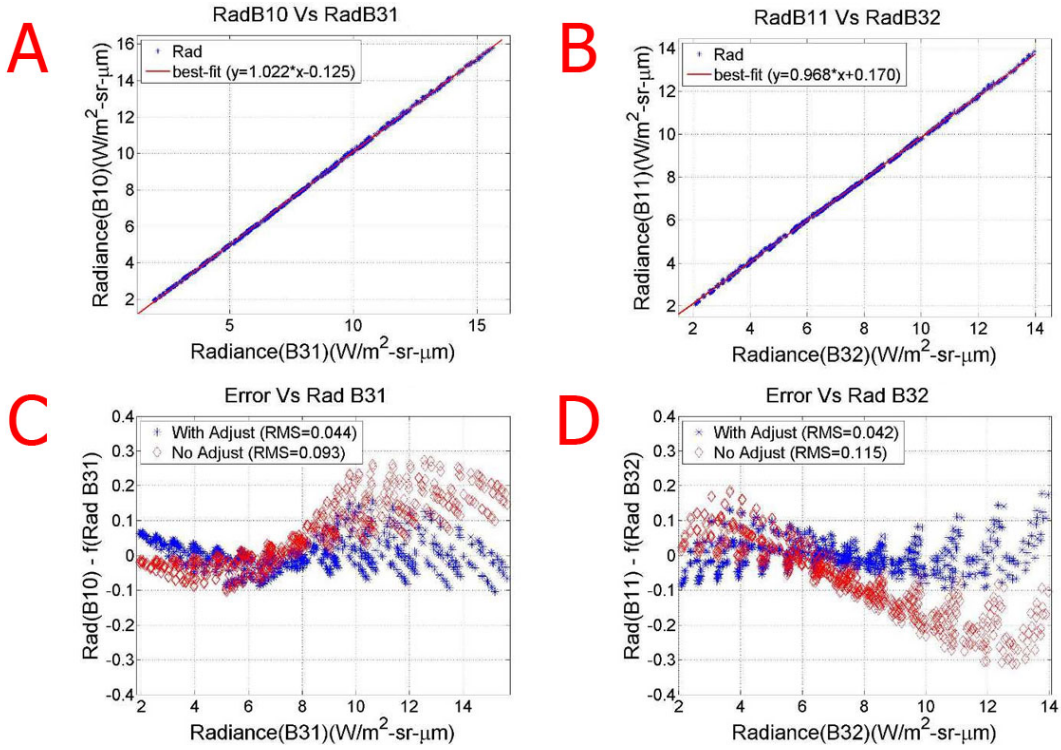

Figure 4.5: Plots for linear regression of *Band 10 Vs Band 31* (A), and *Band 11 vs Band 32* (B). Blue stars are the original data and red line is the best fit-in function. C, Plot of $Rad_{B10} - Rad_{B31}$ (red diamond), $Rad_{B10} - f(Rad_{B31})$ (blue star). D, Plot of $Rad_{B11} - Rad_{B32}$ (red diamond), $Rad_{B11} - f(Rad_{B32})$ (blue star). Here f is the best fit-in function.

Figure 4.5 B. Seen in the error plot in Figure 4.5 D, when Rad_{B32} is lower than 5.31, Rad_{B11} is lower than Rad_{B32}; when Rad_{B32} is higher than 5.31, Rad_{B11} is higher than Rad_{B32}. *RMS* is reduced from 0.115 to 0.042 after applying the linear adjustment function. The maximum error is reduced from 0.31 to 0.20.

For both bands, *RMS* decreases more than half after applying linear adjustment functions. The magnitude of the absolute error of TIRS is several K (recall Figure 2.4). Therefore, the uncertainty of band shape adjustment (RMS) is much smaller compared with the absolute error. Of course, more accurate result can be derived with more tightly constrained parameters, like for a certain material, specific atmosphere model, etc. For our purpose, these errors are small. Final band shape adjustment functions will be used are as shown in Eq. 4.2.

$$\begin{aligned} Rad_{B10} &= 1.022 * Rad_{Band31} - 0.125 \\ Rad_{B11} &= 0.968 * Rad_{Band32} + 0.170 \end{aligned} \tag{4.2}$$

4.3 MODIS View Angle Study

In addition to the band shape adjustment, view angle effect also need to be explored before using MODIS as the truth. View angle effect refers to a possible radiance change due to different view angles. For one instrument, different view angles usually have different atmosphere paths, resulting in different TOA radiances. This is common for all sensors. But usually if the field of view (FOV) of the instrument is small, like ±7.5° of TIRS, this effect is not taken into consideration as such a small difference in the radiance path. But MODIS has a ±55° FOV, which means the periphery of the image will have a significant different atmospheric path from that of the nadir. Considering the dataset with truth to be used: data from the underflying days, MODIS and TIRS almost have the same atmospheric path; data from the polar area, sensor view angle is ±7.5° for TIRS but ±30° for

MODIS. So view angle effect should be investigated for data from polar area. Here we will extend this study up to 60° sensor view angle of the whole MODIS FOV.

4.3.1 Parameters in MODTRAN

Name	Value
Altitude of Object (km)	0
Altitude of Sensor (km)	705
Wave Range (μm)	9 - 14
Spectral Resolution (μm)	0.01
Sensor View Angle	0° - 60°(10° increment)
Material	snow, water, sand
Black-body Temperature (K)	220-340 (10 increment)
Atmosphere Models	Tropical Model Midlatitude Summer model Midlatitude Winter model Subarctic Summer model Subarctic Winter model US Standard 1976
Water Vapor Scalar	0.5, 1.0, 1.5, 2.0

Table 4.4: Parameters used in MODTRAN simulations for View Angle Study

MODTRAN will also be used to simulate the atmospheric conditions, and generate the TOA spectral radiance. As well as in band shape adjustment analysis, two types of parameter, constant parameters and variable parameters, are used in MODTRAN simulations. Constant parameters are: *Altitude of Object*, *Altitude of Sensor*, *Wave Range*, and *Spectral Resolution*. Now *Sensor View Angle* is a variable,

along with *Material*, *Black-body Temperature*, *Atmosphere Models*, and *Water Vapor Scalar*. All parameters are listed in Table 4.4.

4.3.2 Data Processing

For each combination of the parameters listed in Table 4.4, MODTRAN will generate a TOA spectral radiance. Integrated sensor reaching radiance can be computed according to Eq. 4.1 as well as in band shape adjustment analysis section. As this is the MODIS view angle study, we will only calculate the sensor reaching radiances of band 31 and 32. Because the absolute radiance changes with different combination of the parameters. To analyze the data, for the same combination of the four variables, simulated radiances for view angle from 0° to 60° will be considered as one set. In other word, sensor view angle is the only variable in one set. The absolute radiance will change from set to set. Therefore, in order to compare different sets, we will normalize the radiance at 0° to 1 for each set. Following is an example of this processing.

Figure 4.6 is an example of the simulated TOA spectral radiance plot for one specific combination of parameters with sensor view angle from 0° to 60°. It can be found that the whole spectral plot shifts down almost the same amount within both band windows when view angle increasing. In this example, the spectral radiance in band 31 is higher than that in band 32 for the same view angle. As well as the example shown in band shape adjustment (recall Figure 4.4), there are several small dip features around 10.5 μm, 11 μm and 11.7 μm. The corresponding sensor reaching radiances, computed based on Eq 4.1, are listed in the first two rows in Table 4.5. It validates that radiance decreases with view angle increasing for both bands in this case. For the same view angle, the radiance for band 32 is always lower than that for band 31 in this example. The set of radiance is normalized at 0°, dividing the radiance from band 31 by *8.906* and dividing that from band 32 by *8.221*. The normalized radiance are shown in the last two rows

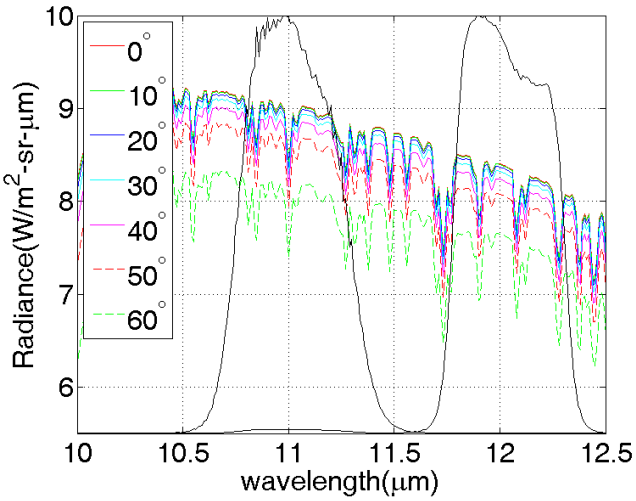

Figure 4.6: Plot for simulated TOA spectral radiance of view angle from 0° to 60° indicated as different line type or color. The solid black lines show the RSR of band 31 and 32. The parameters used are: water, 300 K, midlatitude summer atmosphere model, 1.0 water vapor scalar (default water vapor).

in Table 4.5. All data will be processed as this example.

4.3.3 Result and Analysis

Result and analysis includes two parts: determining the sensitivity order of the four variables and exploration of real scene view angle correction. There are four variables in the MODTRAN simulations. It would be reasonable and necessary to explore how the four variables affect sensor view angle. The real scene view angle correction examples are demonstrated.

Sensor View Angle	0°	10°	20°	30°	40°	50°	60°
Band 31	8.906	8.896	8.866	8.809	8.708	8.516	7.988
Band 32	8.221	8.211	8.182	8.126	8.029	7.850	7.392
Band 31	1.0000	0.9989	0.9956	0.9891	0.9778	0.9562	0.8969
Band 32	1.0000	0.9989	0.9953	0.9884	0.9767	0.9550	0.8992

Table 4.5: Simulated sensor reaching radiance for spectral radiance plot in Figure 4.6. First two rows are the absolute radiance ($W/m^2 \cdot sr \cdot \mu m$) for band 31 and 32. The last two rows are the normalized radiances (unitless).

Sensitivity Order and Analysis

There are four variables in all our MODTRAN simulations. In order to explore sensor view angle effect, we will need to investigate how these variables affect this issue. So the sensitivity order need to be analyzed at first. We will use control variant method to determine the sensitivity order of the four variables. Here are the steps:
Step 1: Choose one of the variant, like atmosphere model.
Step 2: Set the chosen variant constant. Do the plot of *Normalized Radiance vs View Angle* for all combinations. For example, we set the atmosphere model as mid-latitude summer atmosphere model, then plots for all combinations of different materials, different blackbody temperatures and different water vapor scalars.
Step 3: Change the value of the chosen variant. For example change it from mid-latitude summer atmosphere model to mid-latitude winter atmosphere model. Repeat step 2.
Step 4: Compare *Normalized Radiance vs View Angle* plot of different setting of the chosen variant.
Step 5: Choose another variant and repeat step 2 - 4.

Material is chosen as the first variant to explore. Theoretically, the only difference between the materials, snow, water and sand, would be the emissivity

(recall emissivity plot Figure 4.2). As analysis in band shape adjustment section, the emissivities of all the three materials are above 95% and keep almost constant within the spectral band window of both band 31 and 32. Therefore, very few difference would not be expected between the three types of material. Figure 4.7 demonstrates the plot for different materials of both bands. In the plot, the horizontal axis is *sensor view angle* and the vertical axis is *normalized radiance*. Firstly, as expected plot is almost the same for all three materials. Difference between the three materials almost has no effect on sensor view angle issue. But it surprises us that the *normalized radiance* at 60° varies from 1.6 to 0.7 for band 31 and from 1.55 to 0.68 for band 32, which means relatively the radiance at 60° can be 60% higher or 30% lower than the radiance at nadir.

Black-body Temperature is the second one to analyze. As well as the step described above, black-body temperature varies from 220 *K* to 340 *K*. Figure 4.8 shows *NormalizedRadiancevsViewAngle* band 31 plots of several selected black-body temperature setting, 220 *K*, 240 *K*, 270 *K*, 280 *K*, 300 *K* and 340 *K*. Firstly, we compare four subplots. The average line (red dash line) varies a lot along with *black-body temperature* increasing from 220 *K* to 340 *K*. The average *normalized radiance* (red line) at 60° decreases from 1.23 to 0.85 monotonically along with *black-body temperature* increasing from 220 *K* to 340 *K*. The same situation happens to band 32 (Figure 4.9). For band 32, the average *normalized radiance* decreases from 1.2 to 0.85 when *black-body temperature* increases from 220 *K* to 340 *K*. Obviously *normalized radiance* varies much more when *black-body temperature* changes than when material changes. In this sense, we would conclude that view angle issue is more sensitive to black-body temperature than material.

Atmosphere Model is the third variable to be explored. Here all six atmosphere models are used: the tropical model, the mid-latitude summer model, the mid-latitude winter model, the subarctic summer model, the subarctic winter model and the US standard 1976 model. Therefore, for each atmosphere model, *Normalized Radiance vs View Angle* of all combinations of material, black-body

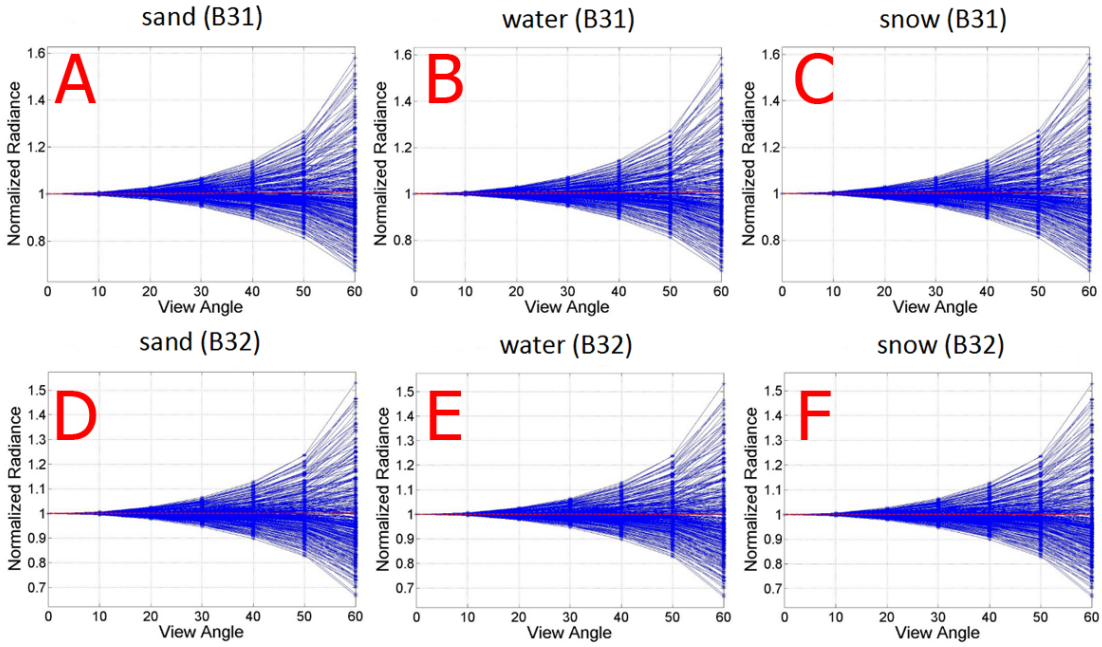

Figure 4.7: *Normalized Radiance vs View Angle* for different materials. Plots of **band 31** of sand (A), water (B) and snow (C). Plots of **band 32** of sand (D), water (E) and snow (F). In each plot, horizontal axis is view angle (0° to 60°) and vertical axis is normalized radiance. First row is for band 31 and second row is for band 32. First column is sand, second column is water and last column is snow. Each subplot contains 312 contours.

temperature and water vapor scalars is presented within one plot. Figure 4.10 and Figure 4.11 present the plots of all six atmosphere models for band 31 and 32 respectively. In each subplot, it contains 156 different combinations. It can be found that, for both bands the spread out of 156 combinations varies for different atmosphere models. Take band 31 for example: it spreads out from 1.6 to 0.72 for the tropical model, from 1.6 to 0.72 for the mid-latitude summer model, from 1.35

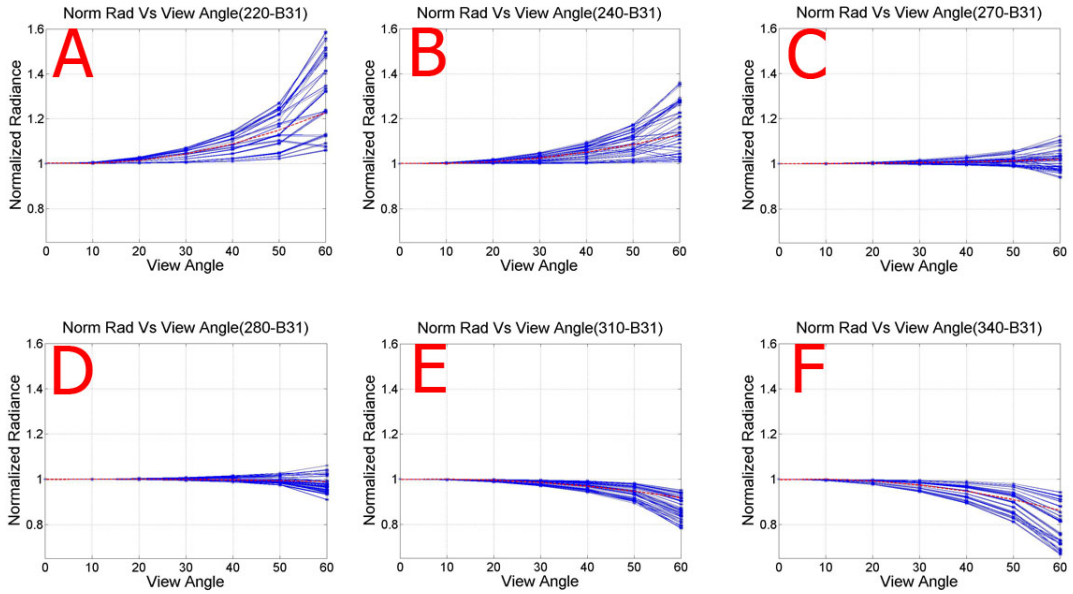

Figure 4.8: Plots of *Normalized Radiance vs View Angle* for **band 31** of different *black-body temperature*: 220 *K* (A), 240 *K* (B), 270 *K* (C), 280 *K* (D), 310 *K* (E), and 340 *K* (F). Red dash line is the average. Each subplot contains 72 contours.

to 0.8 for the mid-latitude winter model, from 1.5 to 0.72 for the subarctic summer model, from 1.1 to 0.9 for the subarctic winter model, and from 1.5 to 0.75 for the US standard 1976 model. Figure 4.11 shows the corresponding plots for band 32. The *normalized radiance* at 60° spreads out from 1.5 to 0.7 for the tropical model, from 1.45 to 0.7 for the mid-latitude summer model, from 1.35 to 0.8 for the mid-latitude winter model, from 1.5 to 0.6 for the subarctic summer model, from 1.15 to 0.9 for the subarctic winter model, and from 1.45 to 0.6 for the US standard 1976 model. But there is clear difference if we compare atmosphere model with black-body temperature. For each subplot in atmosphere model, *Normalized Radiance vs View Angle* spreads out from 1+ to 1− for all atmosphere models; but for different black-body temperature, *Normalized Radiance vs View Angle* can be all larger than

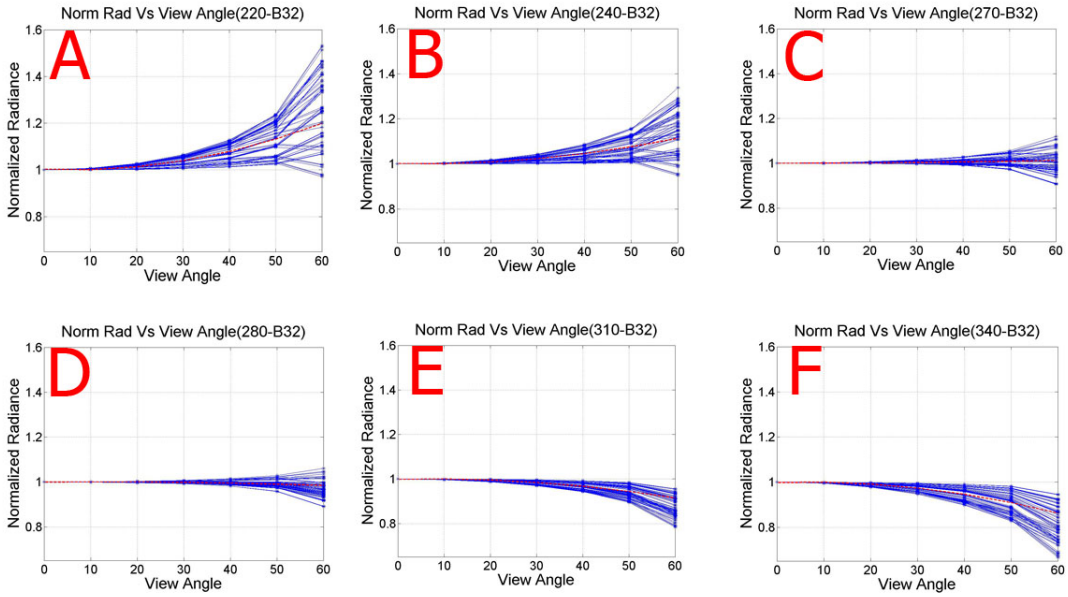

Figure 4.9: Plots of *Normalized Radiance vs View Angle* for **band 32** of different *black-body temperature*: 220 *K* (A), 240 *K* (B), 270 *K* (C), 280 *K* (D), 310 *K* (E), and 340 *K* (F). Red dash line is the average. Each subplot contains 72 contours.

1 or smaller than 1. This shows more effect from black-body temperature than atmosphere model generally.

Water Vapor Scalar is the last variant. As *water vapor scalar* is actually one parameter describing water vapor content within one atmosphere model. Therefore in this case, we will examine the effect of water vapor scalar on different atmosphere models. In this example we only put one specific setting: water, 300 *K*. Figure 4.12 and Figure 4.13 show plots of different *water vapor scalar* for all six atmosphere models for both band 31, 32 respectively. For band 31 in Figure 4.12, it can be found that along with *water vapor scalar* increasing, six curves spread out more, which means less difference between different atmosphere models for lower *water vapor scalar* and more difference between different atmosphere models

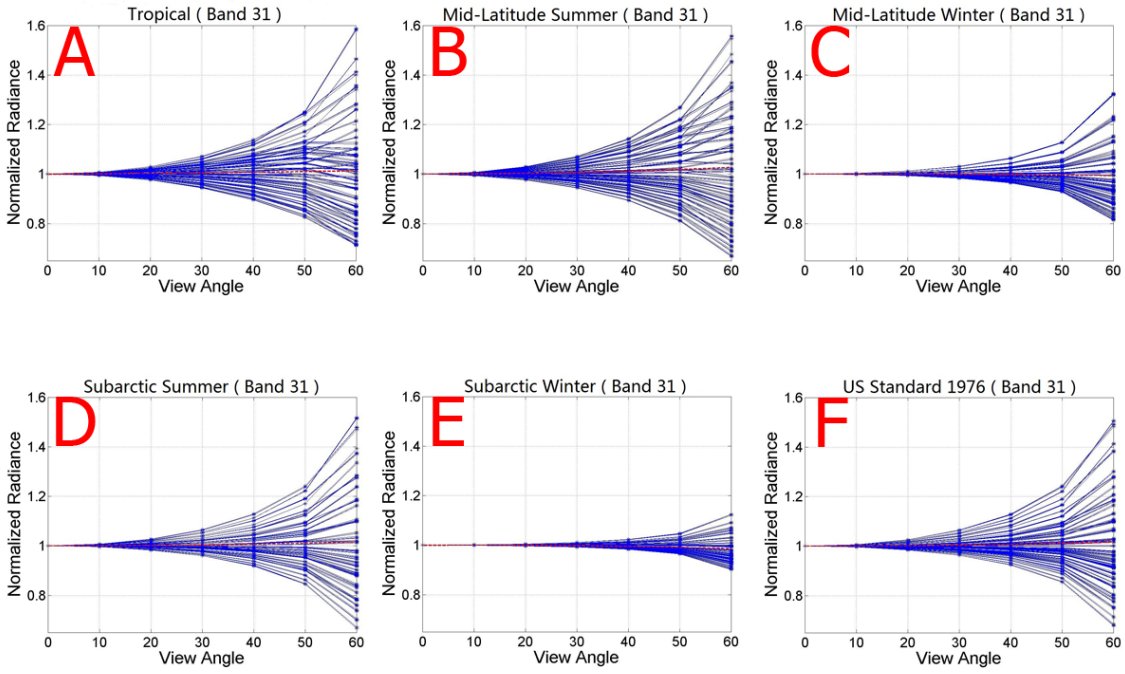

Figure 4.10: Plots of all six atmosphere models (**band 31**): tropical model (A), mid-latitude summer model (B), mid-latitude winter model (C), subarctic summer model (D), subarctic winter model (E), and US standard 1976 model (F). Each subplot contains 156 different combinations.

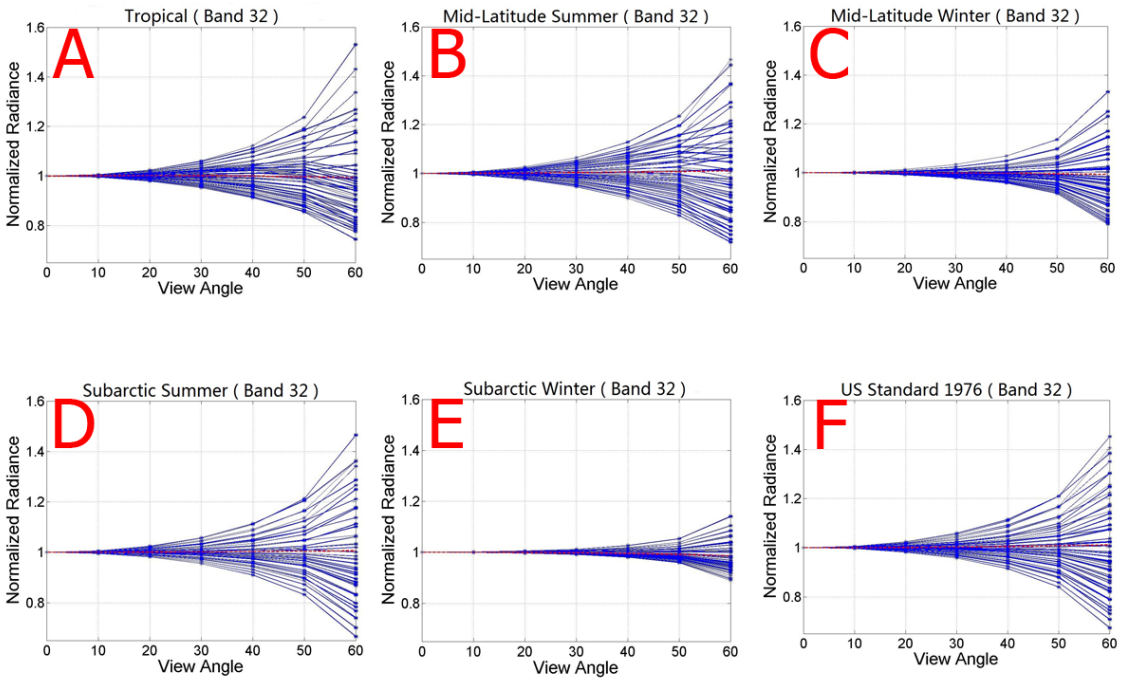

Figure 4.11: Plots of all six atmosphere models (**band 32**): tropical model (A), mid-latitude summer model (B), mid-latitude winter model (C), subarctic summer model (D), subarctic winter model (E), and US standard 1976 model (F). Also each subplot contains 156 different combinations.

for higher *water vapor scalar*. The *normalized radiance* at 60° spreads less than 0.02 for 0.5 *water vapor scalar*, 0.06 for 1.0 *water vapor scalar*, 0.10 for 1.5 *water vapor scalar*, and 0.10 for 2.0 *water vapor scalar*. The spread out is the same for 1.5 and 2.0 *water vapor scalar*. For 1.5 and 2.0 *water vapor scalar*, curve 3 (mid-latitude winter model), 4 (subarctic summer model), and 5 (subarctic winter model) keep the same. This tells us that water vapor is saturated for these three models but it still has effect on the other three models 1, 2 and 6. This demonstrated that water vapor scalar has different effect on different atmosphere models. Almost the same situation occurs for band 32 in Figure 4.13. The *normalized radiance* at 60° spreads less than 0.02 for 0.5 *water vapor scalar*, 0.06 for 1.0 *water vapor scalar*, 0.10 for 1.5 *water vapor scalar*, and 0.10 for 2.0 *water vapor scalar*. Also curve 3 (mid-latitude winter model), 4 (subarctic summer model) and 5 (subarctic winter model) keep the same for 1.5 *water vapor scalar* and 2.0 *water vapor scalar*.

Theoretical Analysis: To sum up, the sensitive order of the four variables is: blackbody temperature > atmosphere model ~ water vapor scalar > material. It surprises us that the *normalized radiance* at 60° changes that much from 220 K to 340 K. If we analyze how the TOA radiance changes with sensor view angle, the sensitive order is a reasonable result.

Usually the TOA radiance can be decomposed into three parts: direct radiance, up-well radiance and down-well radiance as in Eq. 4.3, where T is the black-body temperature, τ is the transmittance and ε is the emissivity of the material.

$$\begin{aligned} Rad_{TOA} &= Rad_{direct} + Rad_{Upwell} + Rad_{Downwell} \\ Rad_{dirct} &= \tau * \varepsilon * Rad_T \\ Rad_{Downwell} &\approx (1-\varepsilon) * Rad_{Upwell} * \tau \end{aligned} \tag{4.3}$$

Rad_{direct} is the direct radiance from the object, which depends on the emissivity(ε) of the material, the temperature of the object (T) and the transmittance of atmosphere(τ). Up-well radiance Rad_{Upwell} is the independent from Rad_{direct}, only depending on the atmospheric condition like atmospheric temperature, air pressure and total

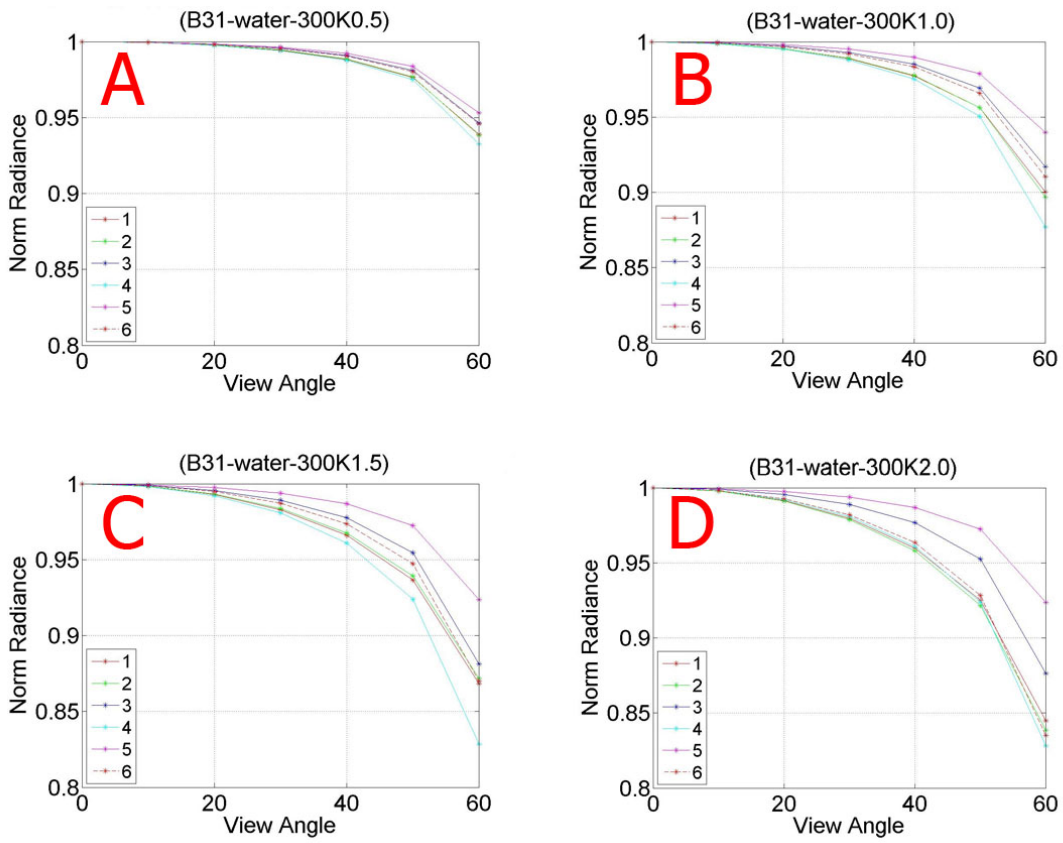

Figure 4.12: Plots of four different water vapor scalars for **band 31**. Each subplot includes the same water vapor scalar for all six different atmosphere model (shown in six different linetypes): 0.5 water vapor scalar (A), 1.0 water vapor scalar (B), 1.5 water vapor scalar (C), and 2.0 water vapor scalar (D). The meanings of the numbers in each subplot are: '1' is tropical model, '2' is mid-latitude summer model, '3' is mid-latitude winter model, '4' is subarctic summer model, '5' is subarctic winter model, and '6' is US standard 1976 model.

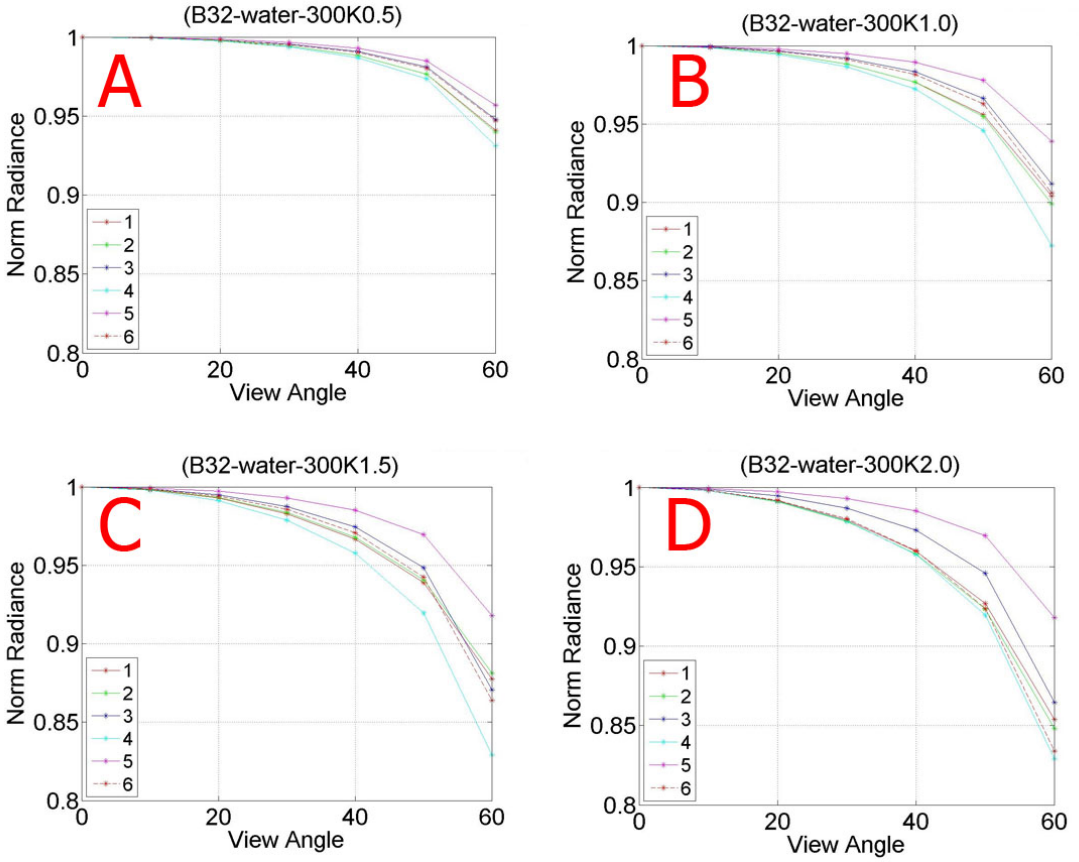

Figure 4.13: Plots of four different water vapor scalars for **band 32**: 0.5 water vapor scalar (A), 1.0 water vapor scalar (B), 1.5 water vapor scalar (C), and 2.0 water vapor scalar (D). Numbers in each subplot share the same meanings as it in Figure 4.12.

water vapor, etc. $Rad_{Downwell}$ is close to the multiplication of the reflectance of object $(1-\varepsilon)$, atmospheric transmittance (τ) and Rad_{Upwell}, for single reflectance model. Due to the high emissivity of the three materials (higher than 95%), in hence low reflectance (lower than 5%), $Rad_{Downwell}$ would only be several percent of Rad_{Upwell}. So for our case, $Rad_{Downwell}$ is such a small amount that is negligible. The TOA radiance can be rewritten as Eq. 4.4.

$$Rad_{TOA} \approx \tau * \varepsilon * Rad_T + Rad_{Upwell} \tag{4.4}$$

The higher the sensor view angle is, the longer the atmospheric path is. Longer atmosphere path results in lower τ, in hence lower Rad_{direct} and higher Rad_{Upwell}. Figure 4.14 shows an example. This is a series plots of water (material), 300 K (ground temperature), mid-latitude summer atmosphere model, default water vapor (1.0 water vapor scalar) for view angle at $0°$, $20°$, $40°$, $60°$. Seen in the plots, when view angle increasing, Rad_{Upwell} increases, Rad_{direct} decreases and Rad_{TOA}, as a sum of the two, decreases but less than that of Rad_{direct}.

As shown in the example Rad_{direct} decreases and Rad_{Upwell} increases when sensor view angle increases. The change of Rad_{total}, when sensor view angle increasing, depends on which part is the dominant part in Rad_{total}. Recalling Eq. 4.4 black-body temperature is the only parameter that could change Rad_{direct} and leaves Rad_{Upwell} intact (we assume ε is constant). Therefore, black-body temperature will determine Rad_{direct} or Rad_{Upwell} being the dominant part in Rad_{TOA}. The change of Rad_{TOA} will keep the same as that of the dominant part. For low black-body temperature, like 220 K in Figure 4.8 and 4.9, Rad_{Upwell} is the dominant part, resulting in Rad_{TOA} increasing along with view angle increasing. For black-body temperature around 270 K − 290 K, where Rad_{direct} is comparable with Rad_{Upwell}, Rad_{TOA} will keep more or less constant along with view angle increasing. For high black-body temperature over 300 K, Rad_{TOA} will decrease along with view angle increasing as the examples in Figure 4.8 and 4.9.

Additionally, atmospheric condition (atmosphere model and water vapor

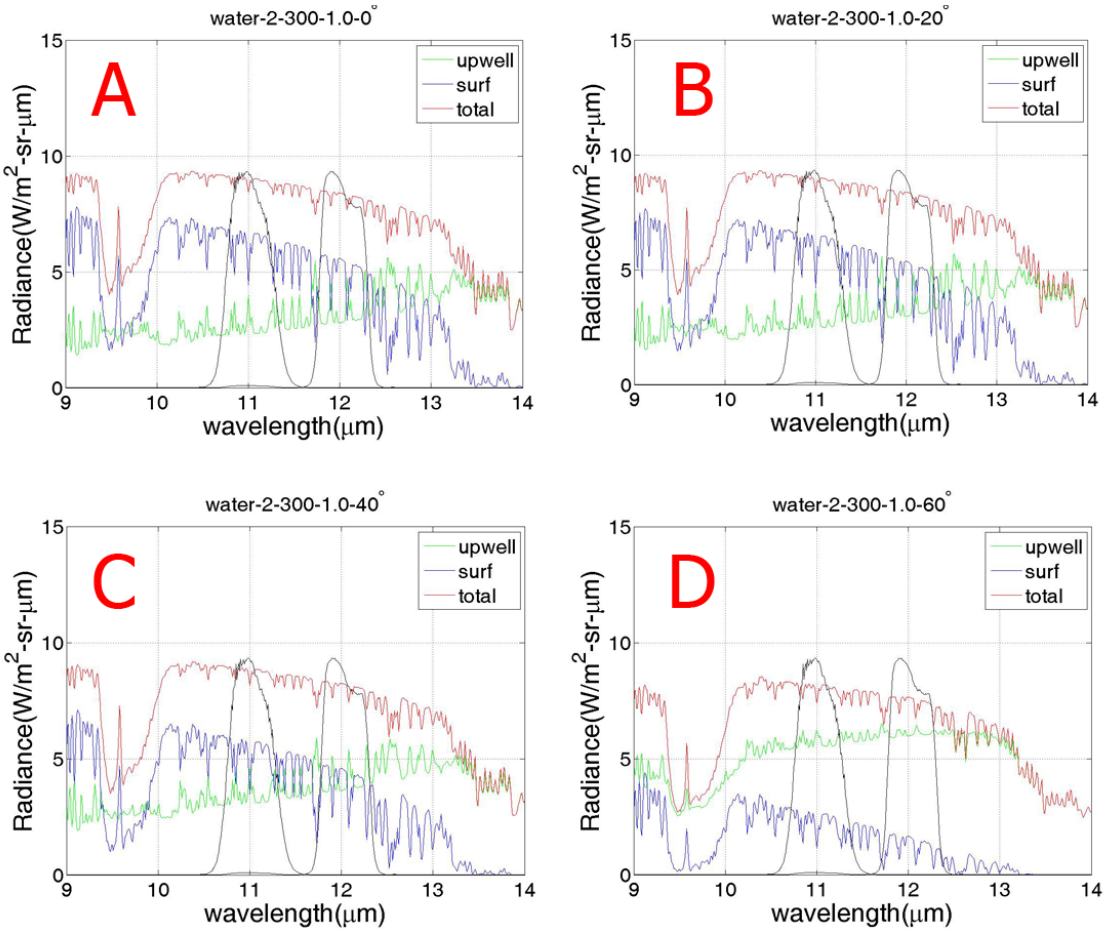

Figure 4.14: Plots of upwell radiance (green line), surf radiance (direct radiance, blue line) and total radiance (TOA radiance, red line) at view angle at 0° (A), 20° (B), 40° (C) and 60° (D). The settings are water, 300 *K*, midlatitude summer atmosphere model and default water vapor.

scalar) will make *Normalized Radiance vs View Angle* spreads out in some degree. Atmosphere model will affect both τ and Rad_{Upwell}. It can be found that for the subarctic summer model it spreads out the least at 60°, followed by the mid-latitude summer model then the other four are close to each other. To sum up, sensor view angle effect is a complex phenomena affected by many factors, as a sensitive order of our four variables: *black-body temperature* > *atmosphere model* ~ *water vapor scalar* > *material*.

Operational Example

Sensitivity order study shows how the view angle issue is affected by different variants from MODTRAN simulations. But for real scene, the atmospheric condition is more complex: atmospheric condition may vary within the same scene due to the large ground size of a satellite instrument. Also the ground temperature will also changes within the same scene. In this section, sensor view angle correction of real scenes is demonstrated.

Example 1: This a hot scene around the equator. Figure 4.15 illustrates the geographic location of this scene. One profile is obtained across the track direction. We will use MODTRAN again to generate the correction curve with several real time data. In order to evaluate the performance of the correction, Geostationary Operational Environment Satellite (GOES) data on the same area is used to show the trend line of the radiance. GOES orbits at altitude of $35,780\ km$, which is very far away from the earth. Therefore the ground swath of MODIS has very small view angle difference for GOES.

Sea surface temperature product from MODIS is used to provide the ground temperature of the scene. Sea surface temperature product is a product from MODIS instrument providing ocean surface temperature globally and this is widely used in many aspects [31]. In this scene sea surface temperature is around from $25°C$ to $29°C$, equal to $298\ K$ to $302\ K$. This is a scene around equator so tropical atmosphere model and mid-latitude summer atmosphere model are used. For

water vapor information, precipitate water vapor product from MODIS is used. This is also a product from MODIS providing the total precipitate water vapor in the atmosphere. For this example, the total precipitate water vapor is within $2\ cm - 4\ cm$ according to the precipitate water vapor product. In MODTRAN three different water vapor settings are used: 2.07 *cm*, 2.92 *cm* and 4.14 *cm*. So MODTRAN will take all these parameters. We will process and analyze the simulated sensor reaching radiance as well as before, normalizing the radiance at $0°$ to 1. Finally, the up-limit and the down-limit of *Normalized Radiance vs View Angle* curves of all the combinations are presented in Figure 4.16.

Figure 4.15: Preview of the chosen MODIS scene around the equator (red line).

Figure 4.17 shows the results after applying the up-limit and the down-limit in Figure 4.16. Because GOES is not well calibrated. In order to conduct a better comparison between GOES with others, a small step is processed with GOES data, subtracting a certain number to make it at the same level of MODIS for small view angle. Firstly, comparing the black line (shifted GOES) and blue dashed line (original MODIS), it is clear that the MODIS data decreases along with sensor view angle (also named sensor zenith) increasing for both bands. It becomes more significant when view angle reaches $40°$. MODIS is lower than shifted GOES for

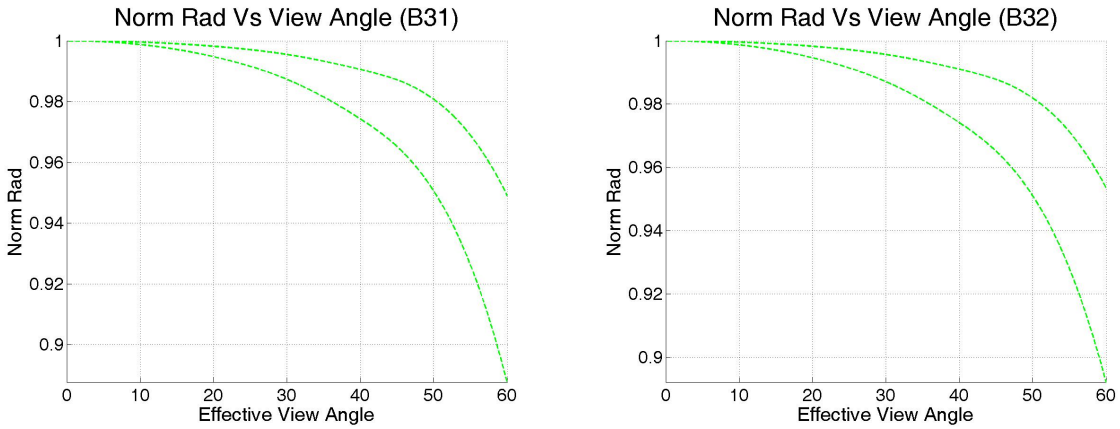

Figure 4.16: Plots of the uplimit and the downlimt of *Normalized Raidance vs View Angle* for operational example of band 31 (left) and band 32 (right).

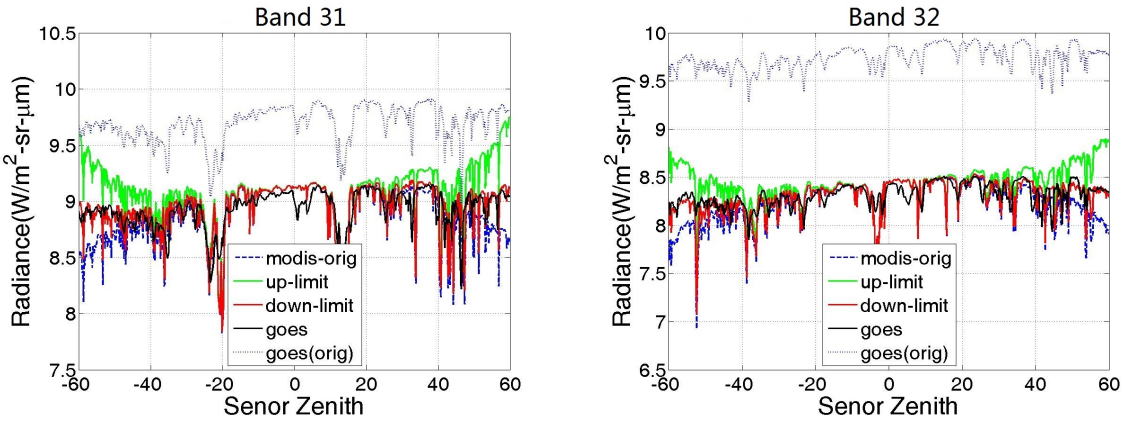

Figure 4.17: Plots of results of applying the up-limit and the down-limit in Figure 4.16 for band 31 (left) and band 32 (right). Several different types of lines are: original GOES, shifted GOES, original MODIS and corrected MODIS (up-limit and down-limit).

around 0.45 $W/m^2 \cdot sr \cdot \mu m$ (4.5 K) at 60° for both bands. After correction, shifted GOES is within the range of the up-limit and the down-limit, much close to the down-limit. This validates the simulations from the MODTRAN. Of course, the uncertainty (range between the up-limit and the down-limit) is still large, around 0.45 $W/m^2 \cdot sr$ at 60° for both bands in this situation. More atmospheric information and more exploration are necessary to narrow down the uncertainty for a more precise calibration.

Example 2: This is an exploration of snow scenes, which are from GreenLand Island or Dome C at Antarctic [32]. For these scenes, there is no GOES data. Therefore, only simulated data can be used. MODTRAN is used as well. The ground temperature is set as 230 K, 240 K, 250 K and 260 K. As the same for example 1 above, the total precipitate water vapor (from corresponding MODIS product) for the scene is used. For all the clear snow scenes from GreenLand Island and Dome C area, the total precipitate water vapor is within 0.05 $cm - 0.08$ cm. So water vapor is set as 0.05 cm, 0.07 cm and 0.09 cm. As snow scenes are from polar area, subarctic summer atmosphere model and subarctic winter atmosphere model are used. Figure 4.18 shows *Normalized Radiance vs View Angle* for these settings. It can be found that from 230 K to 260 K, the limits at 60° are mostly within 0.98 and 1.03. Moreover in each subplot, the curve spreads out very little. The *normalized radiance* at 60° only varies from 1.02 to 0.98 for all these combinations. This is very small compared with the water scene example. This is highly due to this very low water vapor. As the analysis result in last section, *Normalized Radiance vs View Angle* varies little for low water vapor content. But still for different black-body temperature, *Normalized Radiance vs View Angle* curve still changes in some degree.

As stated before, the chosen snow TIRS scenes are usually within the view angle of 30° of MODIS. According to Figure 4.18 difference between 0° and 30° would be around 0.005 $W/m^2 \cdot sr \cdot \mu m$. This is so small that can be negligible. In hence, for snow scene sensor view angle has no effect on using MODIS as truth.

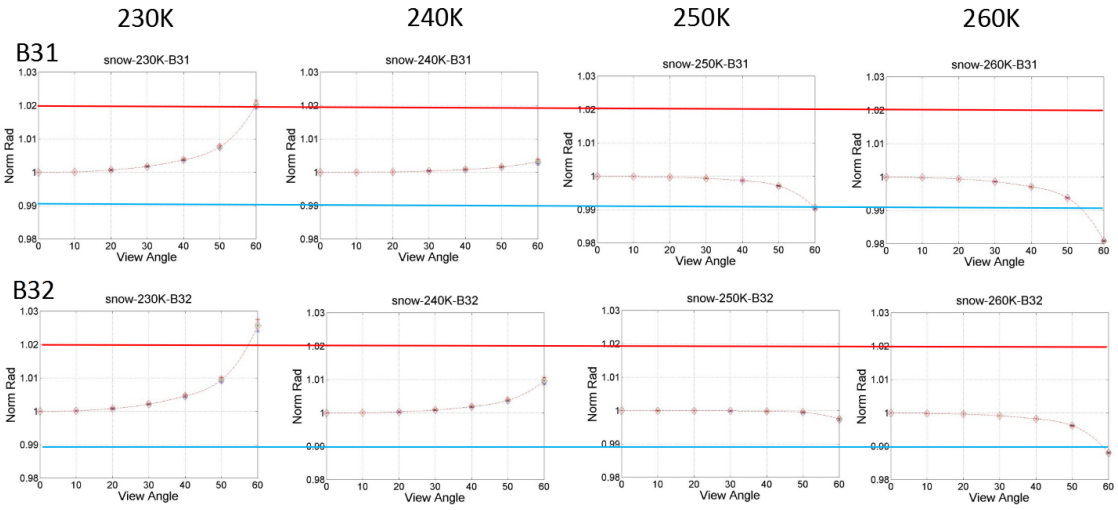

Figure 4.18: *Normalized Radiance vs View Angle* for snow scene situation, with 0.05 *cm*, 0.07 *cm* and 0.09 *cm* water vapor, subarctic summer atmosphere model and aubarctic winter atmosphere mdoel. The first row is band 31 and the second row is band 32. From left to right are 230 *K*, 240 *K*, 250 *K* and 260 *K* for blackbody temperature setting. The red line is *1.02* and the cyan line is *0.99*.

4.4 Summary

This chapter mainly addresses two pre-processing steps of using MODIS as truth: band shape adjustment and view angle effect. We use MODTRAN to simulate atmospheric conditions, obtaining the TOA spectral radiance and calculating the sensor reaching radiance. Hundreds of MODTRAN simulations take three different materials, all six atmosphere models and several different water vapor scalars. These 936 simulations cover all possible atmosphere situations for a solid result. Best fit-in linear function reduced the RMS by half, reaching a good accuracy for our purpose.

For view angle issue, similar to band shape adjustment, we use MODTRAN again to simulate and calculate the sensor reaching radiance for MODIS of sensor

view angle from 0° to 60° with 10° increment. Also all combinations of the four variables are included. Sensitivity order analysis shows that the ground temperature has the biggest effect on the view angle effect followed by atmosphere model and water vapor scalar. No difference on view angle effect is found between snow, water and sand. Correction of the real scene around the equator shows that it is difficult to apply an accurate view angle correction with the available information because the high variance of the atmospheric conditions. For snow scene analysis, results show that there is no necessary to do any correction for the data that we will use. Therefore, for our methodology, the TIRS data from underflying days (no view angle issue) and the TIRS data from polar areas (within 30° of MODIS) do not need any view angle correction. We have a similar view angle correction for GOES data in appendix. More explorations are necessary for a precise correction of sensor view angle issue.

Chapter 5

Result and Analysis

Two methodologies are used to evaluate the performance of the *TIRS-on-TIRS* algorithm as discussed. First is for the TIRS dataset where there is corresponding truth data (MODIS). The other is for the dataset that there is no available truth data. A brief review of the first methodology: compare the corrected TIRS, the original TIRS with the truth data (MODIS) respectively. Two metrics corresponding with the absolute radiometric error and the ”banding” effect will be used to evaluate the performance of *TIRS-on-TIRS* algorithm in a quantitative way. For the second data only the consistency of the absolute radiometric error with the first data set will be explored due to the lack of truth. In addition, profiles with the worst landscape issue can be visualized to evaluate the ”banding” effect.

5.1 Dataset With Truth

MODIS (Terra) is the source of the truth as discussed before. Recalling the two pre-processing steps exploration of MODIS, we will apply band shape adjustment to MODIS data before utilizing as truth, but no need of view angle correction as analyzed. According to the analysis of the *TIRS-on-TIRS* algorithm, three situa-

tions will be taken into consideration: best scenario, landscape issue and cloud issue. Best scenario refers to the situations that out of the FOV has similar radiance with that along the boundary of TIRS, which means that the approximation made by the *TIRS-on-TIRS* will not introduce error. Landscape issue refers to situations where out of FOV has different landscape from the boundary of TIRS yielding different radiance. Cloud issue refers to situations where it is cloudy out of the FOV while there is no cloud along the boundary of TIRS. Two metrics, mean and standard deviation of radiance difference will be used to demonstrate the performance of the *TIRS-on-TIRS* algorithm.

5.1.1 Best Scenario

Example

The key of the *TIRS-on-TIRS* algorithm is substituting the radiance from out of the FOV with that along the boundary of TIRS. For the best scenario, there is a very small radiance difference between out of the FOV and along the boundary of TIRS. Therefore, the *TIRS-on-TIRS* algorithm is expected to have the best performance on these situations. Following is an example. The Landsat ID of this example is LC80160382013087LGN01. Figure 5.1 shows the thermal-band image and the preview of the geographic location of this TIRS scene. Red line is the region of interest. Radiance difference ($TIRS_{orig} - MODIS_{adjust}$ and $TIRS_{correct} - MODIS_{adjust}$) of the red line is plotted in Figure 5.2.

Obviously, the radiance difference plot becomes more flat. The conspicuous "banding" effect is almost removed totally after correction for both bands. As for absolute radiance difference, it can be found that the absolute radiance difference changes more for band 11 than band 10. The absolute error is below 0 for the original and the correct TIRS for band 10. For band 11, the absolute error is below 0 for the original TIRS, but above 0 after correction. The mean and the standard deviation of the radiance difference are listed in Table 5.1. After correction, the

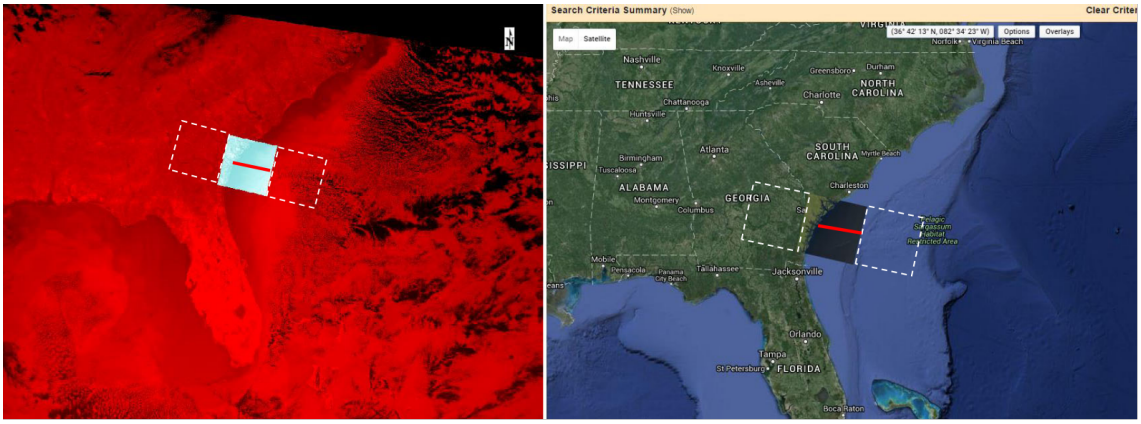

Figure 5.1: Example of best scenario. Left is the three-layer image: red background is MODIS, white area is TIRS. Right is the preview of the geographic location of this scene. White dashed box shows area contributing to the *stray light radiance* of the red line across the scene.

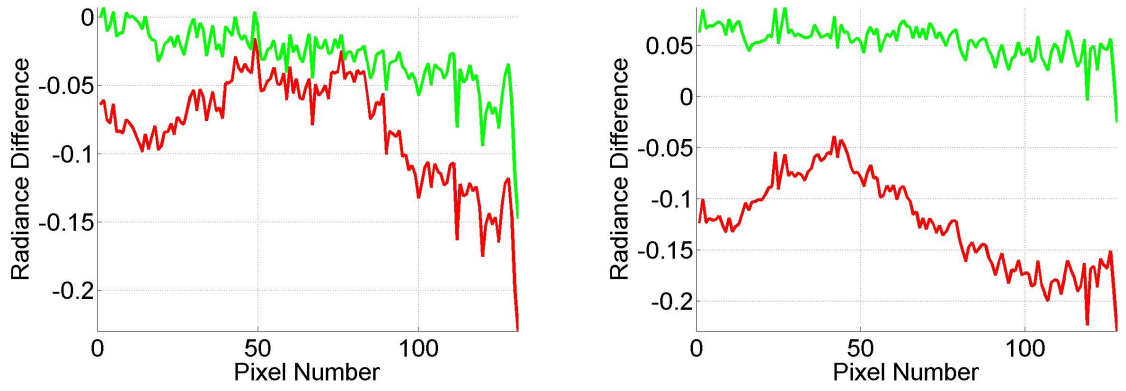

Figure 5.2: Plots of $TIRS_{orig} - MODIS_{adjust}$ (red), $TIRS_{correct} - MODIS_{adjust}$ (green) of band 10 (left), and band 11 (right). $TIRS_{orig}$ is the original TIRS, $TIRS_{correct}$ is the corrected TIRS using the *TIRS-on-TIRS* algorithm, and $MODIS_{adjust}$ is the MODIS data after applying the band shape adjustment.

	mean		standard deviation	
	before	after	before	after
Band 10	-0.0960	-0.0434	0.0356	0.0193
Band 11	-0.1081	0.0700	0.0491	0.0198

Table 5.1: Statistic results of profile of best scenario example. Mean is the mean of radiance difference and standard deviation is that of radiance difference. Before refers to using original TIRS and after means using corrected TIRS.

mean radiance difference increases 0.05 for band 10, and 0.15 for band 11. Both are closer to zero after correction. Also the standard deviation shows the change of the "banding" effect. The standard deviation decreases from 0.0356 to 0.0193 (45.8%, band 10), and from 0.0491 to 0.0198 (59.7%, band 11).

Summary of Best Scenario

There is one set of best scenario profiles. Figure 5.3 plots the absolute radiometric error change of all best scenario cases and Table 5.2 lists the mean of these data points in Figure 5.3. Figure 5.4 plots the standard deviation changes of all best scenario and Table 5.3 lists the mean of these data in Figure 5.4. In both figures, each red circle represents one profile $Rad_{TIRS} - Rad_{MODIS}$ and the corresponding blue star represents one profile applying the *TIRS-on-TIRS* algorithm, $Rad_{correct} - Rad_{MODIS}$. Corresponding red circle and blue star are connected by a green line. For the legend in both figures, *TIRS* represents the original TIRS data and *SLC* is short for *Stray Light Corrected* (TIRS after correction with the *TIRS-on-TIRS* algorithm). This legend note will be applied through the following of the analysis.

Left in Figure 5.3 is summary plot of band 10 and the right is band 11. The horizontal axis is the mean of $TIRS_{correct}$ of the profile. The vertical axis is the mean of ($TIRS_{orig} - MODIS_{adjust}$) (red circle) and ($TIRS_{correct} - MODIS_{adjust}$) (blue star). Points, whose SLC radiances are lower than 4, are profiles from the snow

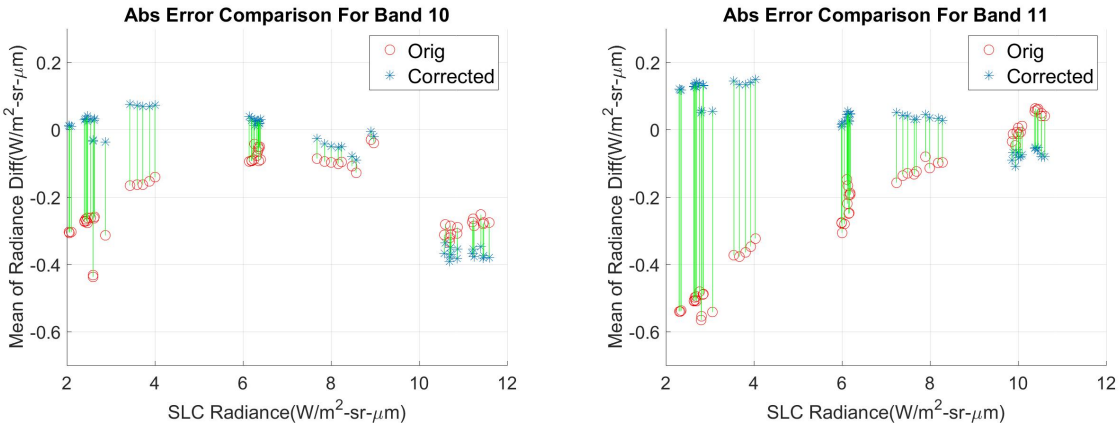

Figure 5.3: Left is the mean changes for band 10 (red circle: $TIRS_{orig} - MODIS_{adjust}$, blue star: $TIRS_{correct} - MODIS_{adjust}$). Right is the same for band 11. *TIRS* in the legend means original TIRS and *SLC* is *Stray Light Corrected*.

Best Scenario (Absolute Radiometric Error)						
	desert scene (15)		water scene(21)		snow scene(20)	
	before	after	before	after	before	after
Band 10	-0.2605	-0.3374	-0.1068	-0.0328	-0.1913	0.0901
Band 11	-0.0274	-0.1179	-0.1461	0.0705	-0.5252	0.0728

Table 5.2: Absolute radiance error for profiles of best scenario. (Numbers in parentheses are the numbers of profiles)

scenes; points, whose SLC radiances are between 6-10, are profiles from the water scenes; points, whose SLC radiances are higher than 10, are profiles from the desert scenes. Table 5.2 lists the mean of all points in Figure 5.3 in three types of material. The statistic results in the table show that for desert scene the absolute radiometric error increases for both band, increasing 0.0769 (band 10) and 0.0905 (band 11). The absolute radiometric error is reduced for both band of profiles from water scene and snow scenes, decreasing 0.0740 (band 10 water), 0.0756 (band 11 water), 0.1012 (band 10 snow), and 0.4524 (band 11 snow). In addition the absolute radiometric error decreases much more for the profiles from the snow scenes than the profiles from the water scene. In terms of the absolute error after the correction, the *TIRS-on-TIRS* algorithm has a better performance on band 10 than band 11, and better on the profiles from the water scene than those from the snow scenes.

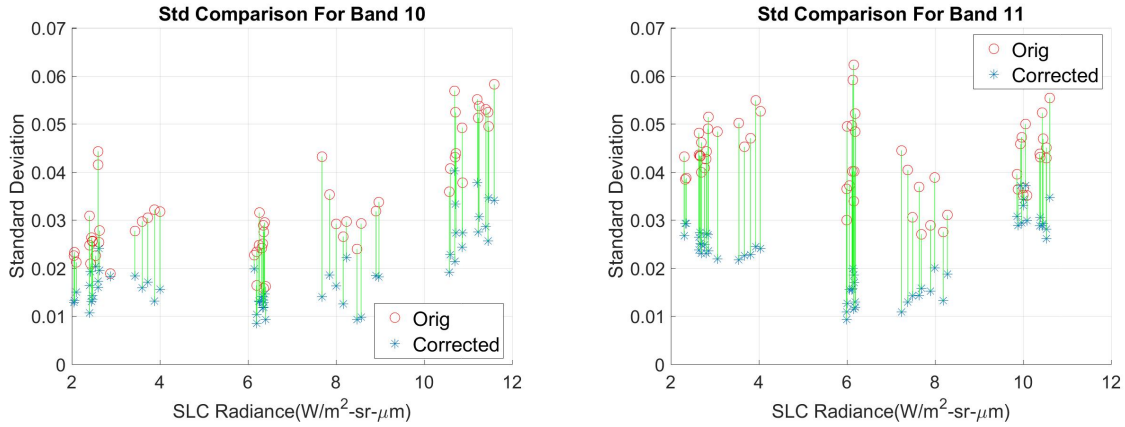

Figure 5.4: Left is the standard deviation changes for band 10(red circle: $TIRS_{orig} - MODIS_{adjust}$, blue star: $TIRS_{correct} - MODIS_{adjust}$). Right is the same for band 11.

Figure 5.4 shows standard deviation changes for all profiles of best scenario (band 10 on left, band 11 on right). Axis and symbols are the same as for Figure 5.3. Here standard deviation is used as a metric to evaluate how banding effect

Best Scenario ("Banding" Effect)						
	desert scene (15)		water scene(21)		snow scene(20)	
	before	after	before	after	before	after
Band 10	0.0495	0.0295	0.0268	0.0135	0.0283	0.0153
Band 11	0.0438	0.0328	0.0414	0.0155	0.0482	0.0255

Table 5.3: Standard deviations ("banding" effect) for profiles of best scenario. (Numbers in parentheses are numbers of profiles)

changes. Table 5.3 lists mean of standard deviation. Firstly, all standard deviations decrease after the correction, 40%(band 10 desert scene), 25% (band 11 desert scene), 49% (band 10 water scene), 62% (band 11 water scene), 46% (band 10 snow scene), and 47% (band 11 snow scene). In this view, the "banding" effect is removed by the *TIRS-on-TIRS* algorithm at least 40% overall. The standard deviation of the profiles from the water scenes after correction is the lowest for both bands, followed by those from the snow scenes and the desert scenes. The standard deviation of band 11 after correction is a little higher than band 10 for all three type of scenes, especially for the snow scenes.

5.1.2 Landscape Issue

As analyzed above, landscape issue situation, where out of the FOV has different material from that on the boundary of TIRS, is supposed to introduce some errors.The *TIRS-on-TIRS* algorithm approximates the radiance from out of the FOV with the radiance from the nearest pixel on the boundary of TIRS. In this landscape issue, different materials will usually result in radiance difference between out of the FOV and the boundary of TIRS. Therefore, the *TIRS-on-TIRS* algorithm is supposed to introduce error for this situation. This section will present the results of the landscape issue. The same analysis procedure will be used as in the best scenario.

Example

Here is an example of the landscape issue. Figure 5.5 shows the screenshot of the three-layer image and the geographic location of this example. The Landsat ID of this example is LC81720432013090LGN01. Also, the red line across the scene indicates the region of interest, and the white dashed box represents the areas contributing to the *stray light radiance* of the red line. The majority area in the left white dashed box is land, but the left boundary of TIRS is sea water; also, the majority area in the right white dashed box is land, but half of the right boundary of TIRS is water and the other half is land. Therefore, landscape issues occurs on both sides, more on the left side. Figure 5.6 shows $TIRS_{orig} - MODIS_{adjust}$ (red line) and $TIRS_{correct} - MODIS_{adjust}$ (green line) for band 10 (left) and band 11 (right). For band 10, after correction, a big improvement on the "banding" effect happened in pixel 70-130. In pixel 130-end, the radiance after correction increases, while the original decreases. In band 10, the peak-to-valley value decreases from 0.2 to 0.15, and from around 0.14 to 0.11 for band 11. Also for band 11 there is an improvement in pixel 70-130 the same in band 10.

Compare plots of the radiance difference in Figure 5.6 with that in Figure 5.2: more "banding" effect remaining in this one than in best scenario for both bands, a little more absolute radiometric error after correction in this example than in best scenario for both bands. Table 5.4 lists the statistic results of this example. Compare the data in these two tables: a higher absolute radiometric error occurs in this landscape issue example, a higher standard deviation after correction in this landscape issue example for both bands.

Summary of Landscape Issue

There is one set of profiles with the landscape issue. Following is the summary of all these cases. Figure 5.7 plots the absolute radiometric error of all the landscape issue profiles and Table 5.5 lists the mean of these data. Figure 5.8 plots the standard deviation of all these profiles and Table 5.6 lists the mean of these standard deviations ("banding" effect).

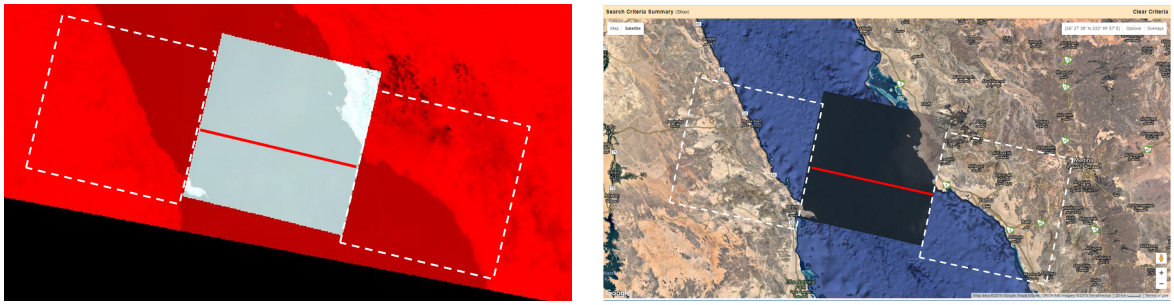

Figure 5.5: Left shows the screenshot of the three-layer image. Right is the geographic of the profile.

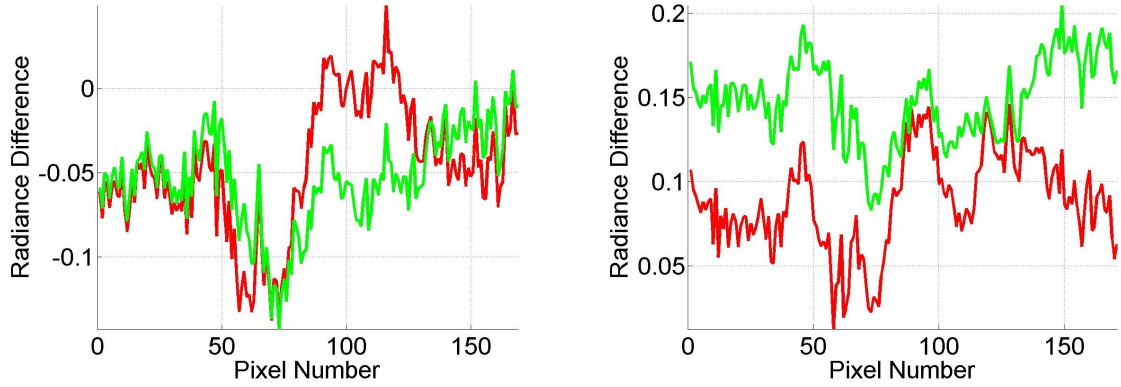

Figure 5.6: Plots of $TIRS_{orig} - MODIS_{adjust}$ (red), $TIRS_{correct} - MODIS_{adjust}$ (green) of band 10 (left) and band 11 (right).

Also the profiles are categorized into 3 groups: desert, water and snow. No profile with landscape issue from desert scene is available. Firstly, in terms of absolute error, it is reduced after correction for both bands of both snow scenes and water scenes. The absolute error reduces the most of profiles for band 11 from snow scenes (73%), the same as for best scenario. Reduction on others are: water band 10 (44%), water band 11 (14.7%), and snow band 10 (30.8%). In terms of absolute sense, after correction for water scenes the absolute error is slightly

	mean		standard deviation	
	before	after	before	after
Band 10	-0.0465	-0.0536	0.0386	0.0290
Band 11	0.0880	0.1479	0.0285	0.0244

Table 5.4: Statistic results of profiles of this landscape issue example. Notes are the same as in Table5.1.

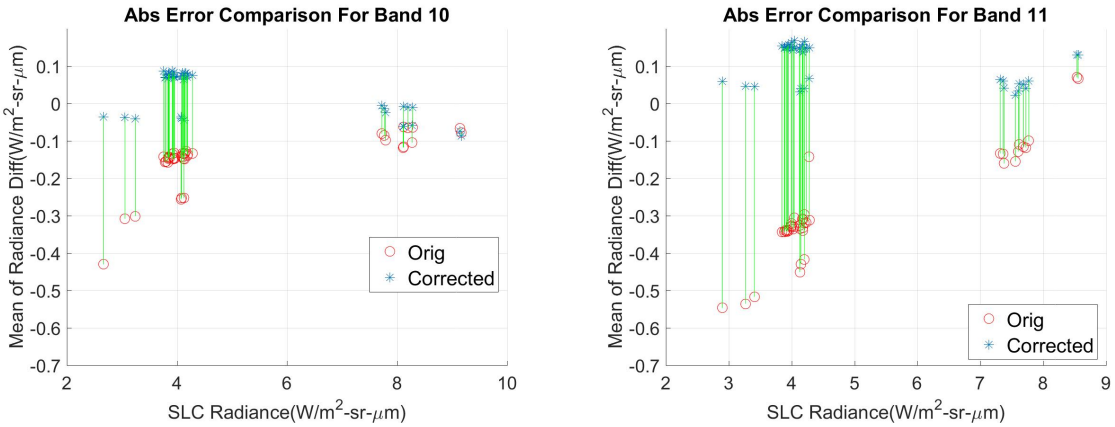

Figure 5.7: Left is mean changes for band 10 (red circle: original, blue star: corrected). Right is the same for band 11.

higher for band 11 (0.0228) than for band 10 (0.0194). For profiles from the snow scenes it is almost the same for band 10 (0.0909) and 11 (0.0906) after correction. For the "banding" effect, the standard deviation decreases a lot for all: 39% (water band 10), 48% (water band 11), 52% (snow band 10) and 63% (snow band 11). Also, the "banding" effect is reduced the most for band 11 of snow scenes, the same as the profiles of best scenario.

Comparison between the absolute error and the standard deviation after correction in landscape issue with those of best scenario can reveal the impact of the landscape issue on the absolute radiometric error. For absolute error, there is

Landscape issue (Absolute radiometric error)						
	desert scene (0)		water scene(11)		snow scene(31)	
	before	after	before	after	before	after
Band 10	NA	NA	-0.1080	-0.0604	-0.1315	0.0909
Band 11	NA	NA	-0.0835	-0.0712	-0.3388	0.0906

Table 5.5: Absolute radiance errors for profiles of landscape issue. (Numbers in parentheses are numbers of profiles)

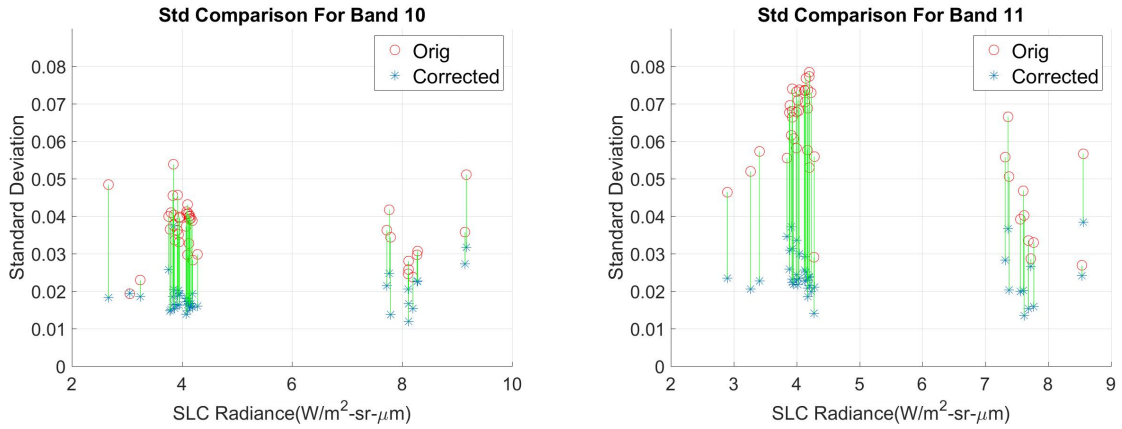

Figure 5.8: Left is the mean changes for band 10 (red circle: original, blue star: corrected). Right is the same for band 11.

0.03 difference for band 10 of water scene, 0.0007 for band 11 of water between best scenario and landscape issue, 0.0008 for band 10 snow and 0.018 for band 11 snow. Except for a little bigger difference in band 10 of water scene, others are quite stable and small, which means the absolute error does not change much for profiles with landscape issue. But for the "banding" effect, the standard deviation after the correction of profiles with landscape issue is higher than those from best scenario for both bands from snow scenes and water scenes: 44% (band 10 water), 47% (band 11 water), 24% (band 10 snow), and 5% (band 11 snow).

Landscape issue (”Banding” effect)						
	desert scene (0)		water scene(11)		snow scene(31)	
	before	after	before	after	before	after
Band 10	NA	NA	0.0326	0.0194	0.03935	0.0189
Band 11	NA	NA	0.0441	0.0228	0.0700	0.0267

Table 5.6: Standard deviations (”banding” effect) for profiles of landscape issue. (Numbers in parentheses are numbers of profiles)

For profiles from the water scenes, usually radiance difference between land and water is higher and nonuniform on some area across the focal plane. But for snow scenes, all are from polar area. Therefore, though landscape issue existing, there is very little radiance difference between out of the FOV and the boundary of TIRS. Hence, there is much less difference between best scenario and landscape issue of profiles from the snow scenes than those from the water scenes.

5.1.3 Cloud Issue

Cloud issue is another situation that introduces error by the approximation of the *TIRS-on-TIRS* algorithm. Chapter 2 already gives the analysis of cloud issue, where out of the FOV is cloudy and the corresponding boundary of TIRS is cloud-free. Compared with landscape issue, cloud issue is less predictable as the atmosphere changes all the time. Of the whole dataset with truth, only several examples were found.

Example

Following is an example of profile with the cloud issue. The Landsat ID of this example is LC82300472013089LGN01. Figure 5.9 shows the three-layer image and the geographic location of this scene. Again, the red line is region of interest and the white dashed box is the out of FOV area contributing to the *stray light radiance* of the red line. Obviously, there is no landscape issue in this example.

But as indicated by the three-layer image, it is clear that on the top-left area of the left white dashed box, the radiance is much lower than the left boundary of TIRS. However, on the right side, the radiance in white dashed box is close to that on the right boundary of TIRS. Therefore, expected error would be the overestimated *stray light radiance* on the left side.

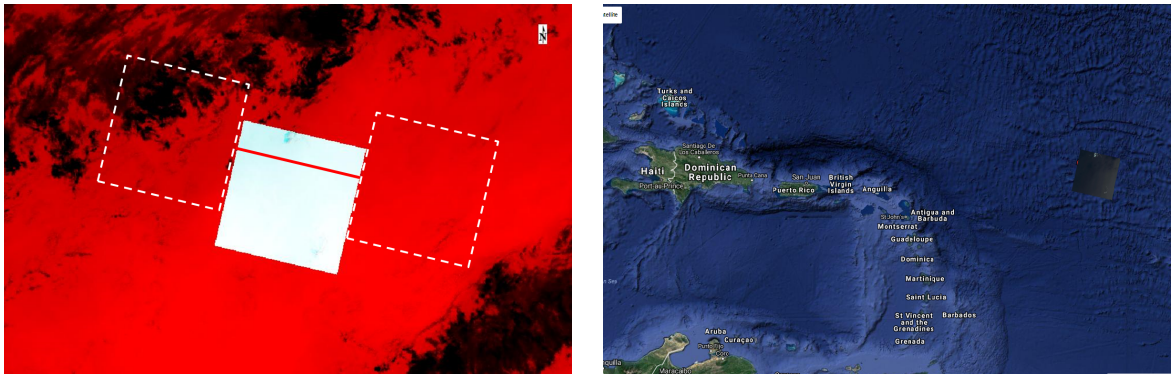

Figure 5.9: Left is the three-layer image of the example as well as previous example. Right is the geographic situation of this example.

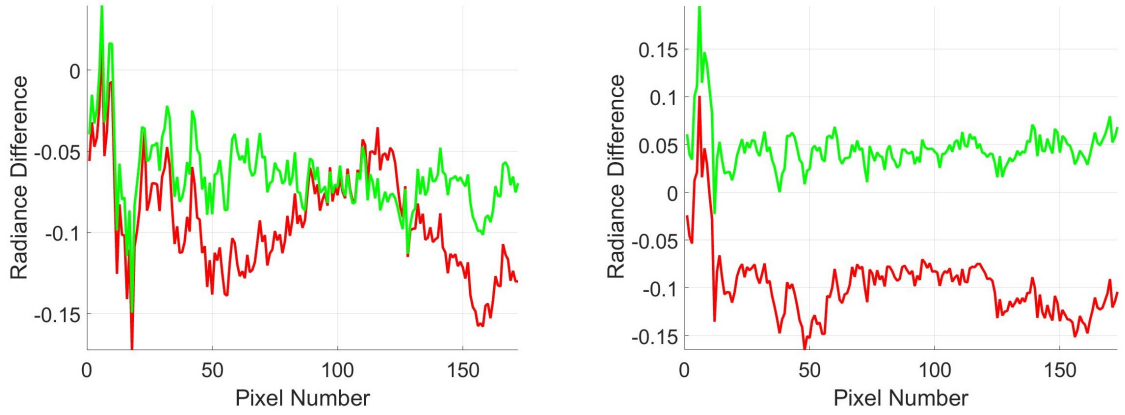

Figure 5.10: Plots of $TIRS_{correct} - MODIS_{adjust}$ (green line), $TIRS_{orig} - MODIS_{adjust}$ (red line) of band 10 (left) and band 11 (right).

Figure 5.10 shows the plots of the profiles ($TIRS_{orig} - MODIS_{adjust}$: red line, $TIRS_{correct} - MODIS_{adjust}$: green line). For band 10 on the left, generally a big improvement on the "banding" effect occurs in pixel 50-160. But the line varies a lot in pixel 1-50, especially a big dip around pixel 20. As the cloudy area on the left white dashed box has lower radiance than that on the left cloud-free boundary of TIRS, the *TIRS-on-TIRS* algorithm will overestimate the *stray light radiance* resulting in $TIRS_{correct}$ lower than expected. This overestimation is pixel-wise. So the profile varies more in pixel 1 - 60. Therefore, the cloud has different impact on the correction for different pixels. The line becomes much smooth in pixel 70 - 160. Almost the same situation for band 11 on the right, the "banding" effect improvement generally happens in pixel 50 - 160. Still in pixel 1 - 70, the green line varies more than in pixel 70 - 160, the same as in band 10 on the left.

Summary of Cloud Issue

As the same for best-scenario and landscape issue, mean and standard deviation are used to evaluate the absolute radiometric error and the "banding" effect. Figure 5.11 plots the absolute radiometric error change of profiles with cloud issue and Table 5.7 lists the mean of these data. Figure 5.12 plots the standard deviation changes of profiles with cloud issue and Table 5.8 lists the statistic results. Firstly, limited cloud issue profiles were found as indicated above: 4 from snow scenes (three smallest radiance), 3 from water scenes (three middle radiance) and 3 from desert scenes (highest radiance).

The absolute radiometric error almost has no change for band 10 of profiles from the desert scenes. There is a little improvement on band 11 of profiles from the desert scenes, but a big improvement on both bands of profiles from the water scenes and the snow scenes. Profiles from the snow scenes in Figure 5.11 showed that the changes of the 4 profiles are consistent with each other, and as well as the 3 profiles from the water scenes. But the four profiles from the desert scenes vary from each other, especially for band 10. This is due to partially the low uniformity of the desert scene in addition to the limited available profiles. Because the low

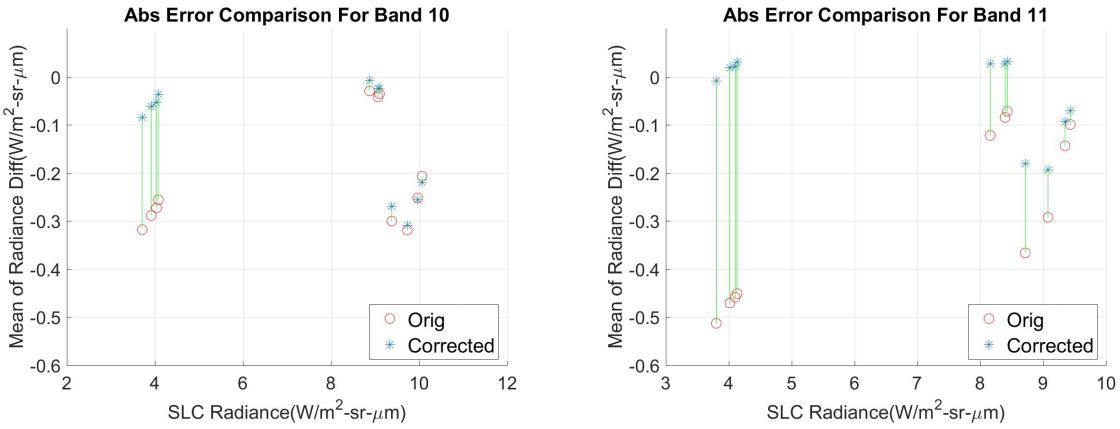

Figure 5.11: Red circle: mean of ($TIRS_{orig} - MODIS_{adjust}$), blue star: mean of ($TIRS_{correct} - MODIS_{adjust}$). Left is band 10 and right is band 11.

Cloud issue (Absolute radiometric error)						
	desert scene (4)		water scene(3)		snow scene(4)	
	before	after	before	after	before	after
Band 10	-0.254	-0.247	-0.105	-0.088	-0.249	-0.025
Band 11	-0.248	-0.158	-0.076	-0.046	-0.509	-0.020

Table 5.7: Absolute radiance errors for profiles of cloud issue. (Numbers in parentheses is numbers of profiles)

uniformity, error will be introduced by stacking the TIRS with the MODIS and the resolution difference between the two. Therefore, the statistic results in Table 5.7 are more meaningful for profiles from the water scenes and the snow scenes than for profiles from the desert scenes.

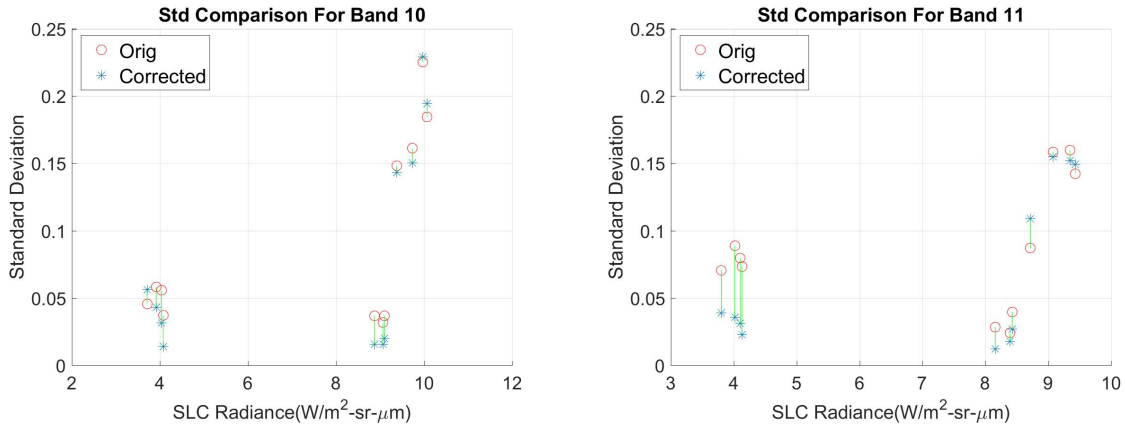

Figure 5.12: Red circle: standard deviation of ($TIRS_{orig} - MODIS$), blue star: standard deviation of ($TIRS_{correct} - MODIS$). Left is for band 10 and right is band 11.

Cloud issue (Banding Effect)						
	desert scene (4)		water scene(3)		snow scene(4)	
	before	after	before	after	before	after
Band 10	0.175	0.174	0.034	0.017	0.044	0.035
Band 11	0.141	0.147	0.028	0.018	0.076	0.031

Table 5.8: Standard deviations (banding effect) for profiles of cloud issue. (Numbers in parentheses is numbers of profiles)

For the "banding" effect, seen from Figure 5.12, profiles from the water scenes are consistent with each other. Again, it varies much more from each other for profiles from the desert scenes for the same reason. In Table 5.8, for profiles from

the water scenes, the standard deviation decreases almost 50% for both bands. For snow scene, it decreases 20% for band 10 and 59% for band 11. But the standard deviation does not change for desert scene, even increasing a little in band 11. Also this is partially due to the low uniformity of desert scene. Low-uniformity introduces error during layering TIRS with MODIS, and this error varies from pixel to pixel. MODIS has resolution of $1km$, while TIRS has $100m$. When stacking the TIRS with the MODIS, different registration methods used by the two instruments will introduce some errors when the scene varies a lot. This error is pixel by pixel. So this will have a bigger effect on the standard deviation.

5.1.4 Residual Error from Best Scenario

Through the full examination of three different scenarios above, the *TIRS-on-TIRS* algorithm has a good performance on correcting the absolute error for all scenes in all scenarios and reducing the standard deviation by half. But the standard deviation only gives the overall of the change of the "banding" effect. It is necessary to explore if there is any specific residual error pattern across the focal plane after the correction.

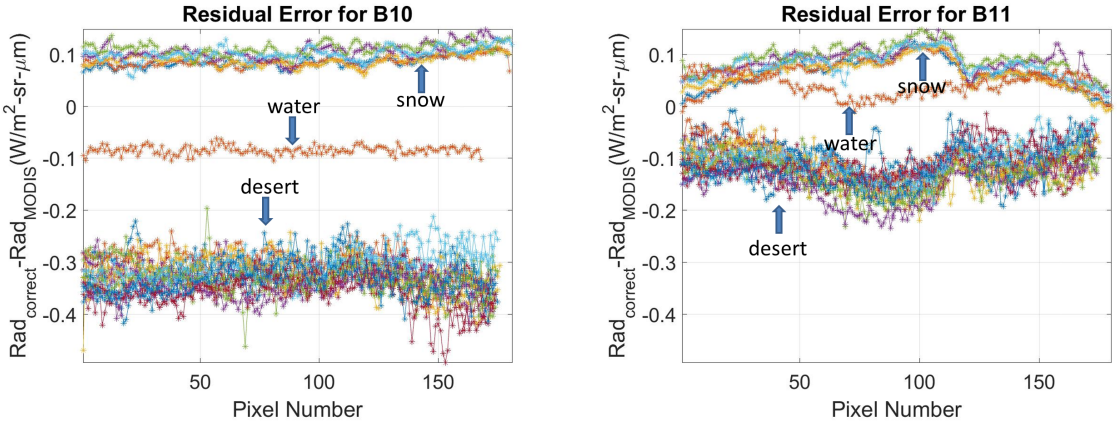

Figure 5.13: Residual error of band 10 (left) and band 11 (right).

Figure 5.13 gives the residual error after correction of the profiles across the focal plane. The vertical axis is the residual error ($Rad_{correct} - Rad_{MODIS}$), and the horizontal axis is the pixel number from the west to the east of the scene. Any profile has less than 165 km ground swath (165 pixels here) across the scene is masked out. The reason is that if the profile does not across the focal plan enough, the trend line of the profile is meaningless in terms of residual error pattern. Additionally, all these profiles come from best scenario. Moreover, the reason why there is only 1 profile from water scene is that most profiles from the water scenes are along the coastline, which makes the profile not across the focal plane or it has landscape issue.

For band 10 (left) in Figure 5.13, it shows almost flat in all three situations. However, for band 11 on the right, there is a clear residual error pattern for profiles from snow scene and desert scene. An obvious jump around 2/3 of the profiles from both the snow scenes and the desert scenes. This is the boundary between SCA-C and SCA-B. For the only water profile, the residual error varies more for band 11 than the corresponding one for band 10. This explains why the standard deviation after correction in band 11 is always higher than that in band 10.

As the training processing of the *TIRS-on-TIRS* algorithm takes no difference between band 10 and 11. Therefore, this residual error pattern in band 11 is highly due to error from the optical model.

5.2 Dataset Without Truth

This section demonstrates the results of data without truth. As stated above, all the data here is not going to be compared with any truth data. Only data before correction and after correction will be compared with each other. The comparison consists of two parts: the stability of the absolute radiance change and the visual examination of the ”banding” effect in worst situations.

5.2.1 Absolute Radiance Error Consistency

This subsection demonstrates the consistency between the change of the mean of radiance from the dataset without truth and that from the dataset with truth. Comparison of these two changes will show the stability of the performance of the *TIRS-on-TIRS* algorithm. The plot is shown in Figure 5.14. The plot shows great consistency of mean radiance change of with-truth data and without-truth data for both band 10 and 11. The mean radiance change is a linear relationship with the mean of correct radiance. The correlation coefficients for band 10 and 11 are -0.9941, -0.9961. These two values show that the high confidence of a linear relationship between the change from the dataset with truth and that from the dataset without truth. In another word, the improvement on the absolute radiometric error from the dataset with truth should also be valid for the dataset without truth.

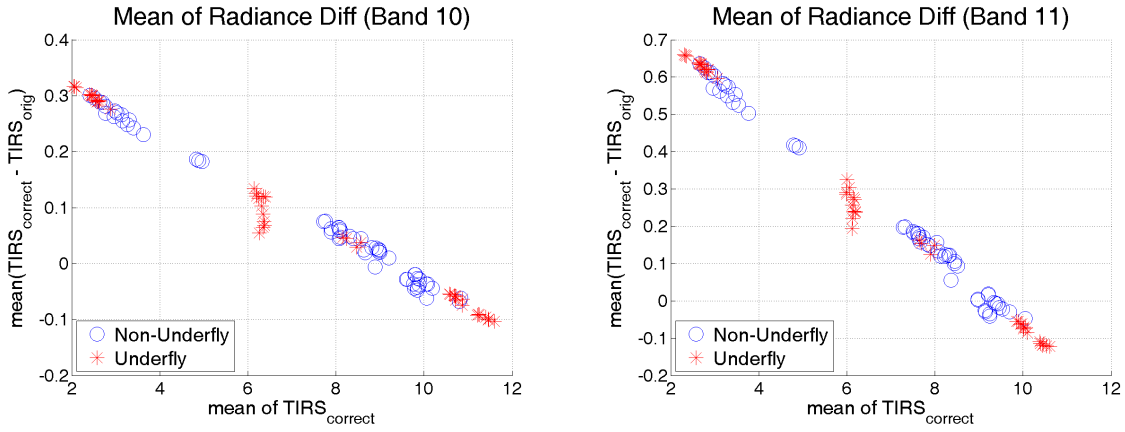

Figure 5.14: Left is the mean changes for band 10 (red star: dataset with truth, blue circle: dataset without truth). Right is the same for band 11.

5.2.2 Visual Examination of ”Banding” Effect

As stated in the methodology part, evaluation of the ”banding” effect for the dataset without truth will be ”viewing” the profiles directly. Here profiles with the worst landscape issue will be presented. So this section shows the worst performance of the *TIRS-on-TIRS* algorithm. Table 3.3 in Chapter 3 gives the list of the Landsat IDs of the chosen scenes. Figure 5.15 - 5.23 show all the geographic landscape locations and the profile plots of band 10 and 11 in order. In all these figures, the geographic location preview is plotted in **A**, band 10 profile plots are shown in **B**, and band 11 profile plots are presented in **C**. In these geographic location previews, the red line across the scene is the region of interest, and the two white dashed boxes are the out of FOV regions contributing to the *stray light radiance* radiance of the red line. In both profile plots, red line is the original TIRS data and blue is the corrected TIRS after applying the *TIRS-on-TIRS* algorithm. Four cloud issue example are also used to investigate the impact of cloud issue on the ”banding” effect.

Profiles with Worst Landscape Issue

Figure 5.15

For this scene, firstly from the geographic location subplot (Figure 5.15 A), the left boundary of TIRS is water while some of the left white dashed box is land, which should have a higher radiance than that of the left boundary of TIRS. Also, the right boundary of TIRS is closer to land than the right white dashed box, which means the right boundary of TIRS may have a slight higher radiance than that of the right white dashed box. This can also be verified from the profile plots in the figure. Overall, there is an obvious landscape issue on the left of the scene and maybe a slight radiance difference on the right part.

For Figure 5.15 B subplot (profile plot for band 10), generally after correction, the profile plot becomes smoother. In pixel 1300 - 3000, the radiance increases

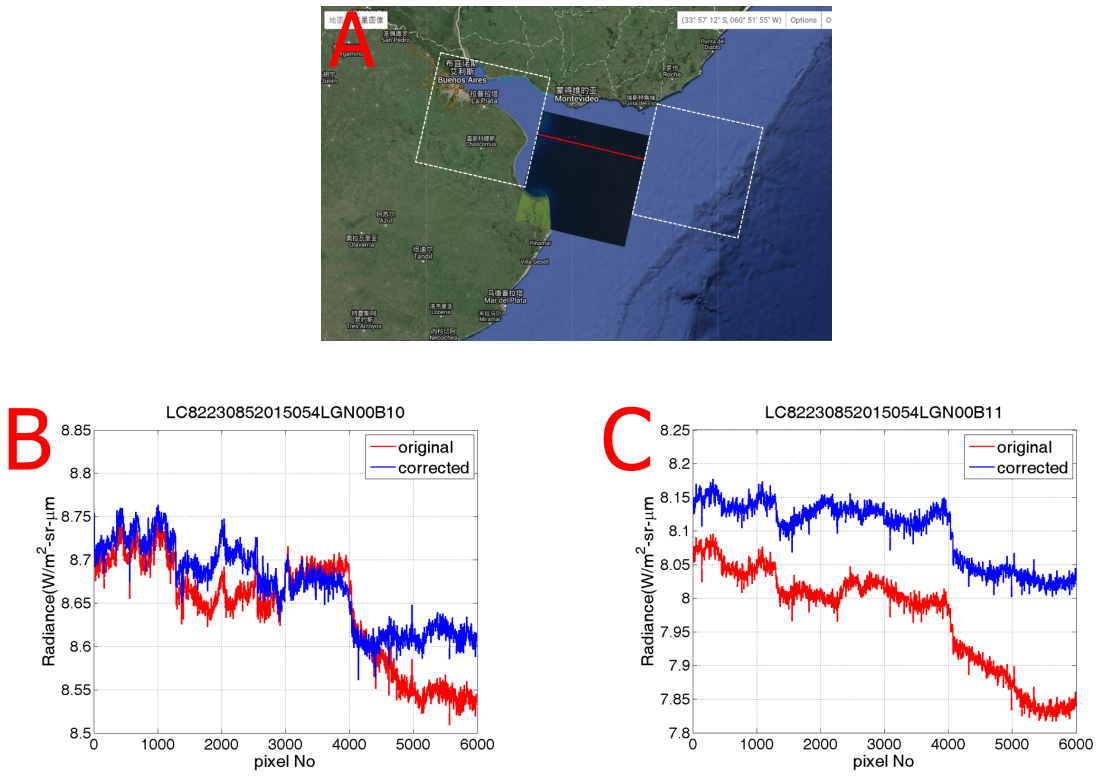

Figure 5.15: Geographic location preview for LC82230852015054LGN00 (**A**). Landscape issue shows in the left. Profile plots of band 10 (B) and 11 (C).

after correction, more consistent with the radiance level in pixel 1 - 1000. But the radiance jump on pixel 1300 still exists without too much improvement. For the jump on pixel 4000, there is a slight improvement, though still exists. Additionally, a big improvement happens in pixel 4000 - 6000, which makes a better consistent profile. For Figure 5.15 C subplot (profile plot for band 11), it is almost the same situation as for profile for band 10: general improvement of the ”banding” effect, slight improvement in pixel 1300 - 4000, almost no improvement of the jump on pixel 1300, a slight improvement on the jump on pixel 4000, and a big improvement in pixel 4000 - 6000. As analyzed above, the *TIRS-on-TIRS* algorithm underestimates the *stray light radiance* from the left due to the landscape issue. For the right part, the *TIRS-on-TIRS* algorithm may overestimate the *stray light radiance* slightly, which makes the right part radiance a little lower than the truth. For both bands, due to the landscape issue in left part, in pixel 1 - 4000, the radiance varies more while in pixel 4000 -6000 it becomes more flat. This is due to the pixel-wise effect from landscape issue in the left part of this example.

Figure 5.16

For this scene, the geographic location subplot (Figure 5.16 A) shows a severe landscape issue in the right area and maybe a slight radiance difference between the left boundary of TIRS and the left white dashed box, which is due to the different distances from the continent.

For band 10 profile plot (Figure 5.16 B) in pixel 1 - 3000, before correction the profile looks like a ’V’ shape with a dip on pixel 2000, while after correction this dip is reduced a lot. Moreover, another obvious improvement happens in pixel 4000 - 6000. Overall, the peak-to-valley value reduces from 0.4 to 0.3 after correction. The same situation occurs for band 11 profile plot (Figure 5.16 C), general improvement the peak-to-valley radiance is reduced from 0.26 to 0.2 after correction, and a little improvement on the jump on pixel 2000. But for both bands the dips on pixel 2000 and 4000 still exist after correction.

Figure 5.17

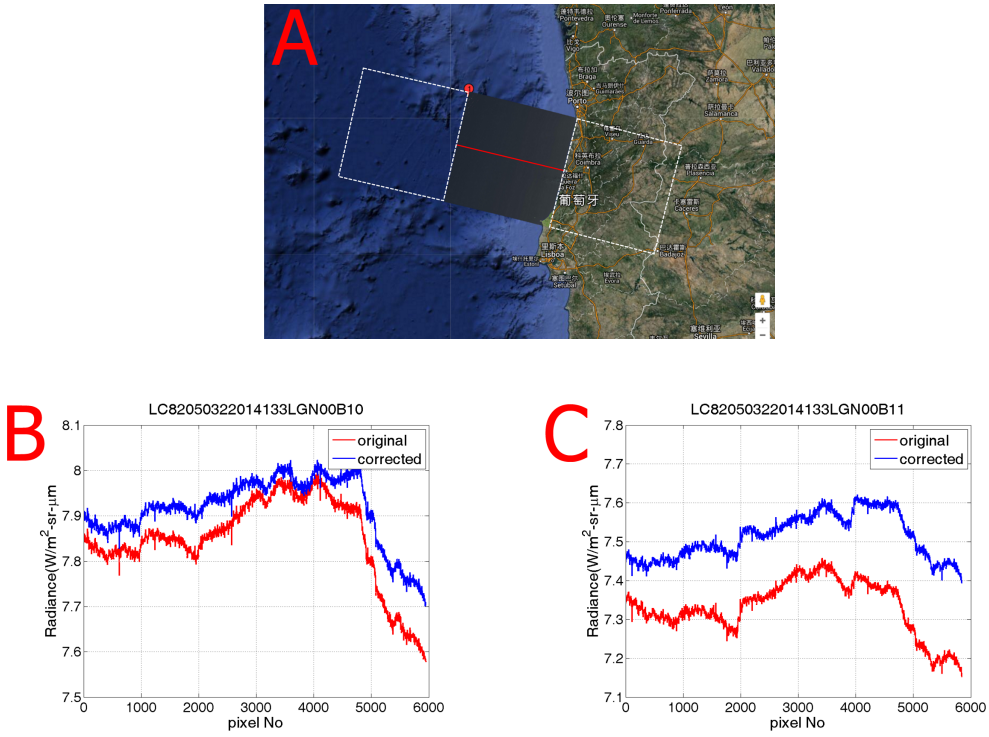

Figure 5.16: Geographic location preview for LC82050322014133LGN00 (A). Landscape issue shows on the right. Profile plots of band 10 (B) and 11 (C).

Firstly, the geographic location subplot (Figure 5.17 A) shows the landscape issue on the left side, almost none on the right side. Therefore, the *TIRS-on-TIRS* algorithm will underestimate the *stray light radiance* from the left side.

Band 10 profile plot in Figure 5.17 B shows a big improvement on the "banding" effect after correction. Overall, the peak-to-valley value is reduced from 0.1 to 0.05 after correction. In pixel 1 - 3500, after correction there is still the same variance trend but the variance amplitude is reduced almost by half. In pixel 1800 - 6000, there is a big improvement in terms of consistency with the trend in pixel 1 - 3000. For band 11 in Figure 5.17 C, a good improvement on the "banding" as well, overall the peak-to-valley value is reduced from 0.15 to 0.08 after correction.

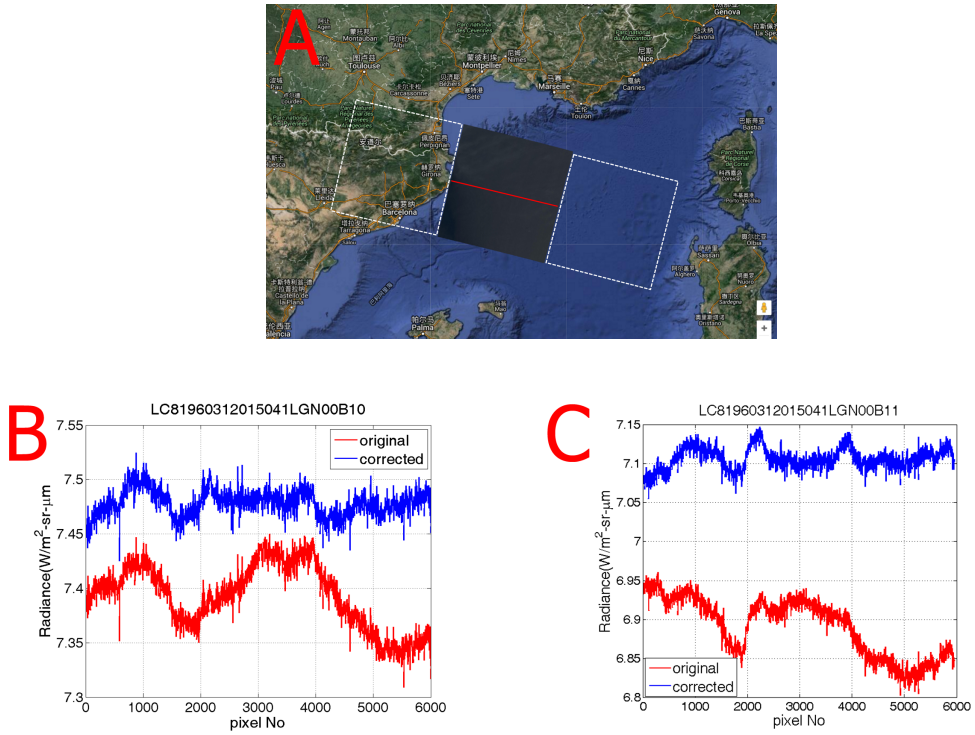

Figure 5.17: Geographic location preview for LC81960312015041LGN00 (A). Landscape issue shows on the left. Profile plots of band 10 (B) and 11 (C).

As well as the profile for band 10, in pixel 1 - 3000, the same variance trend line after correction, but the variance amplitude is reduced around by half. In pixel 1800 - 6000, the corrected profile has a much better consistency with the trend line in pixel 1 - 3000. Partially due to the landscape issue on the left, there is still the sawtooth in pixel 1 - 4000.

Figure 5.18

From the preview plot (Figure 5.18 A), both sides of this scene have severe landscape issue. The *TIRS-on-TIRS* algorithm is expected to underestimate the *stray light radiance* from both sides, but probably in different degree because they are not the same situations for two sides.

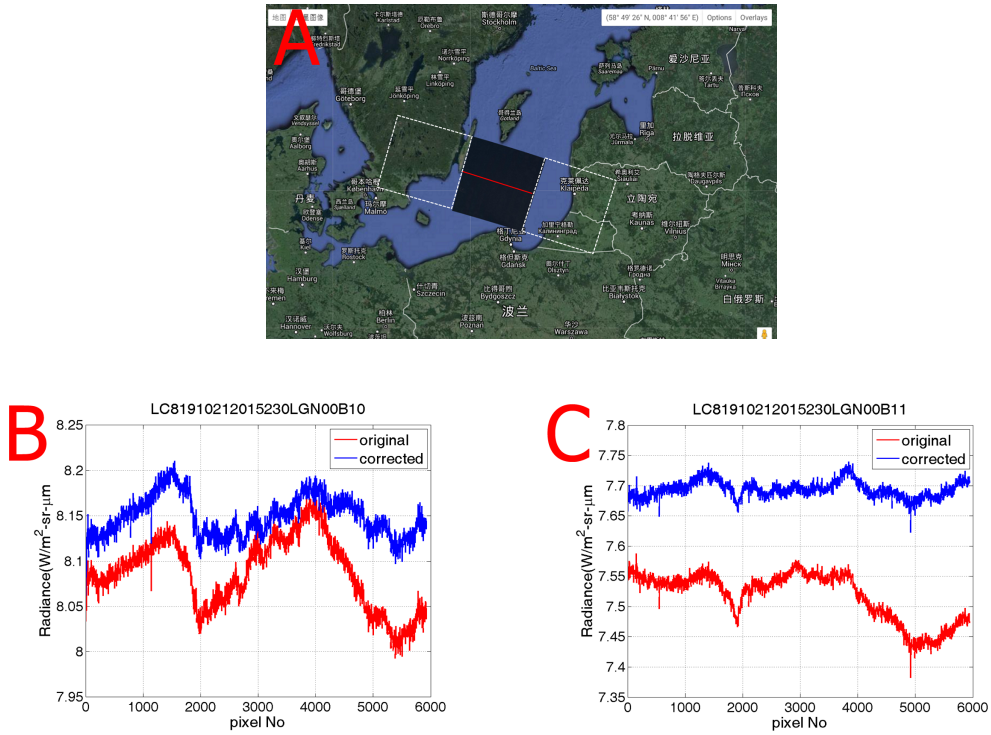

Figure 5.18: Geographic location preview of LC81910212015230LGN00 (A). Landscape issue shows on both the left and right. Profile plots of band 10 (B) and 11 (C).

For band 10 profile plot in Figure 5.18 B, in terms of the "banding" effect there is a big improvement in pixel 2000 - 6000, while in pixel 1 - 2000 the profile does not changes much. The peak-to-valley value reduces from 0.15 to 0.09. For band 11 in Figure 5.18 C, there is a big improvement in pixel 2000 - 6000 as well and the peak-to-valley value drops from 0.15 to 0.09. The dip in around pixel 2000 in both bands is highly due to landscape issue on the left.

Figure 5.19

The geographic location preview of this scene (Figure 5.19 A) shows landscape issue only for the right part area. Profile plots in Figure 5.19 B (band 10) and Figure

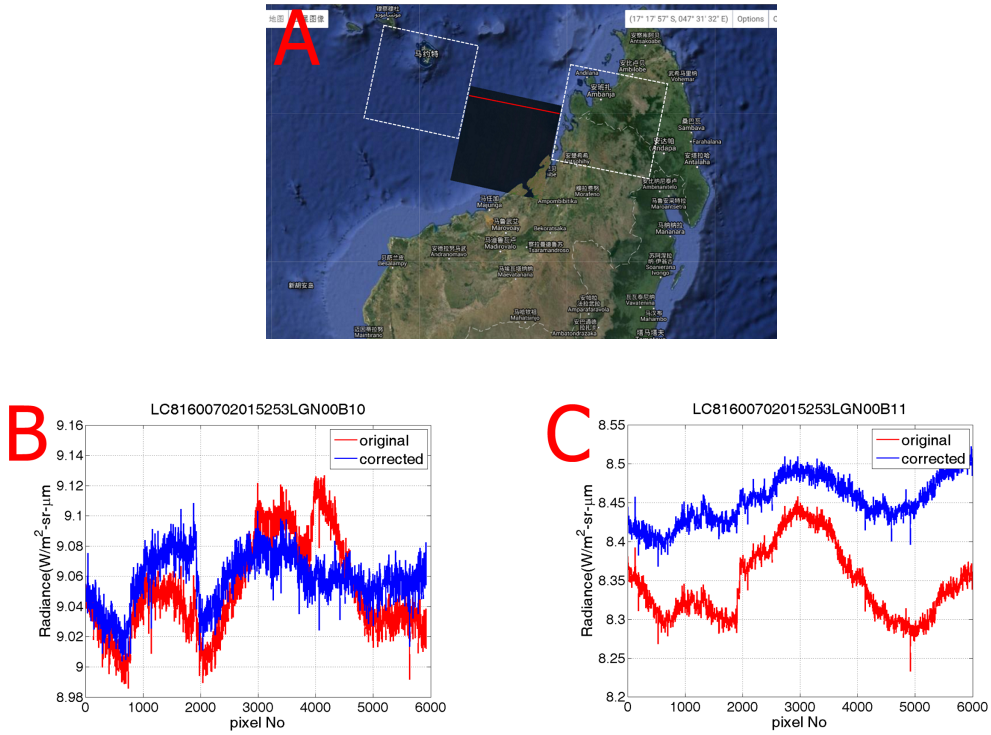

Figure 5.19: Geographic location preview of LC81600702015253LGN00 (A). Landscape issue shows on the right. Profile plots of band 10 (B) and 11 (C).

5.19 C (band 11) show a great improvement for both bands in pixel 2000 - 6000. For band 10 subplot in Figure 5.19 B, in pixel 1 - 2000, there is just a slight change, but no improvement for the jump on pixel 2000. But for profile subplot for band 11 in Figure 5.19 C, the jump on pixel 2000 is almost totally removed after correction. For both bands due to the landscape issue, the *TIRS-on-TIRS* algorithm will underestimate the *stray light radiance* from the right part, which contributes to the *stray light radiance* in pixel 2000 - 6000. Therefore, after the correction, the dip in pixel 2000 (around 0.05 $W/m^2 \cdot sr$) still exists for band 10 but not band 11. The difference performance of the *TIRS-on-TIRS* on pixel 2000 between band 10 and 11 shows the difference of the *TIRS-on-TIRS* algorithm may have between band

10 and 11.

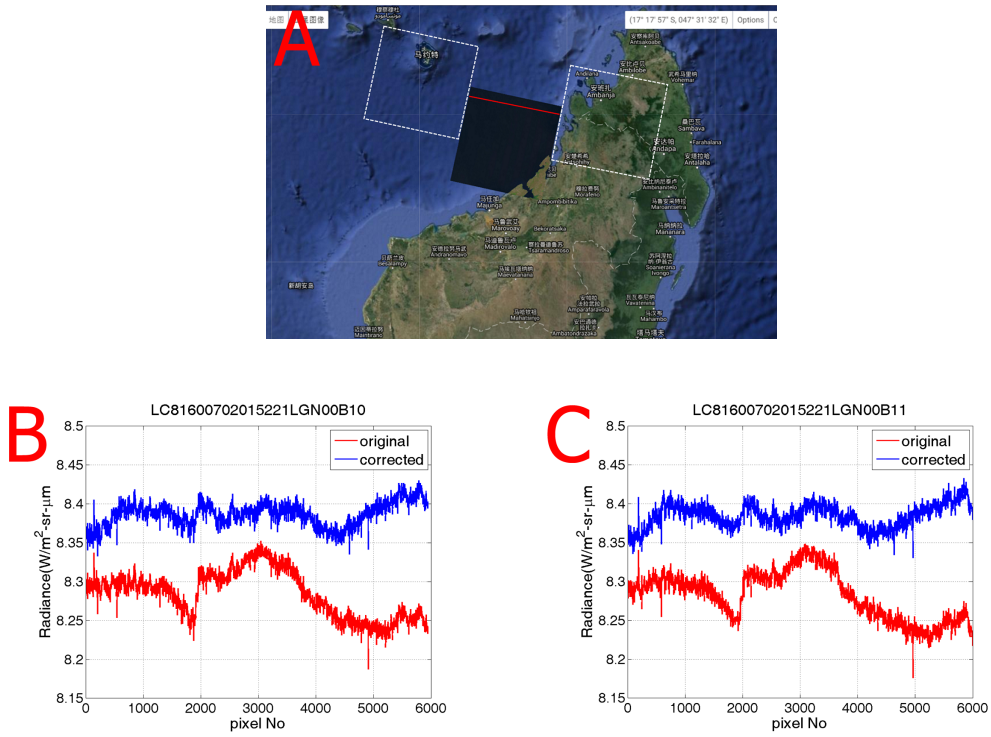

Figure 5.20: Geographic location preview of LC81600702015221LGN00 (A). Landscape issue shows on the right. Profile plots of band 10 (B) and 11 (C).

Figure 5.20

This is the same geographic location scene as last one. Theoretically, landscape issue only happens on the right part.

Generally, profile plots in Figure 5.20 B (band 10) and Figure 5.20 C (band 11) show a big improvement after correction for both bands through the whole profile. Firstly, the jump on pixel 2000 in both bands is removed a lot after correction. Additionally, the uniformity is much better after correction in pixel 2000 - 6000, the peak-to-valley value decreasing from 0.13 to 0.08 for band 10, and from 0.13 to 0.08 for band 11.

In this scene, there is still a small '∧' ($0,03\ W/m^2 \cdot sr$) on pixel 2000 (the boundary of SCA-A and SCA-C) for both bands after correction. Compared with the example from the last one, the *TIRS-on-TIRS* has good performance on band 11 in both scenes and better performance on this one than Figure 5.19 for band 10. This may be due to the ground truth difference between the two.

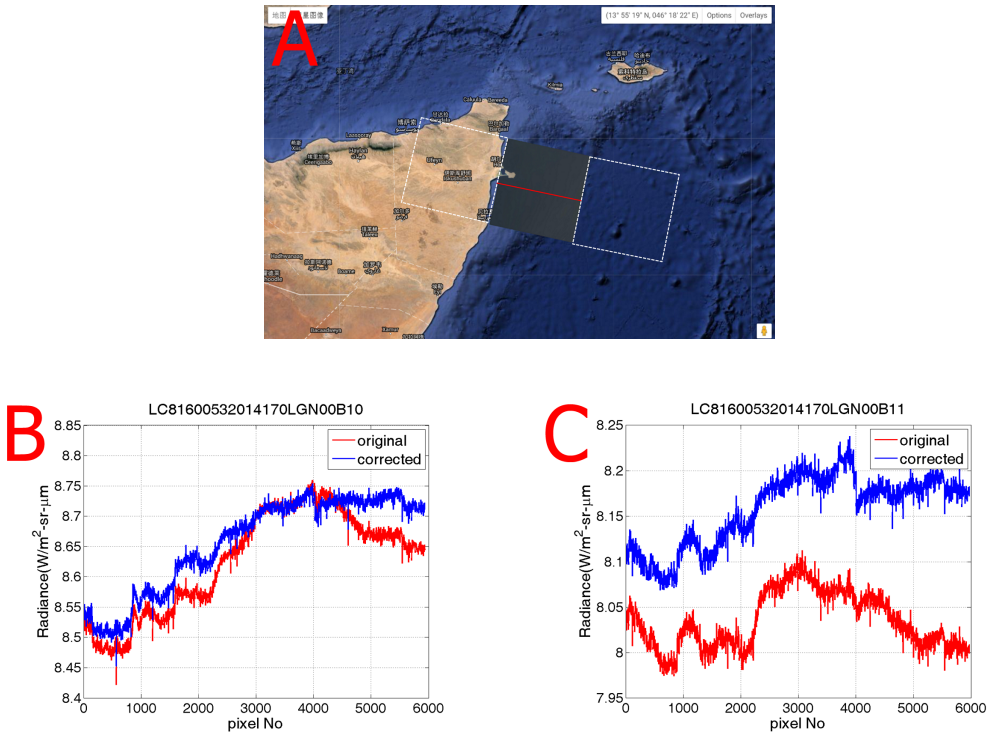

Figure 5.21: Geographic location preview of LC81600532014170LGN00 (A). Landscape issue shows on the left. Profile plots of badn 10 (B)and 11 (C).

Figure 5.21

The geographic location preview (Figure 5.21 A) shows landscape issue only on the left part of the scene, and on the right side maybe there is a little radiance difference between the out of FOV region and the right boundary of TIRS due to the difference distances from the continent.

Generally, after correction profile becomes smoother for both band 10 (Figure 5.21 B) and 11 (Figure 5.21 C). For band 10, the profile in pixel 4000 - 6000 follows the trend after correction, making the overall profile smoother hence less "banding" effect. But still there is a small jump around pixel 800, 1600 and 4000. The sawtooth in pixel 1 - 4000, including several jumps, is highly due to the landscape issue on the left. For the profile plot of band 11, overall the profile becomes smoother after correction especially in pixel 2000 - 3000. But still there is still a jump around pixel 800, and a big jump on pixel 4000, which does not exist before correction. As the same situation on band 10, both are more highly due to the landscape issue on the left. For both bands the 0.05 jump around pixel 4000 are exaggerated by the correction due landscape on the left, which makes the *TIRS-on-TIRS* algorithm underestimating the *stray light radiance* in pixel 1 - 4000, SCA-A and SCA-C (recall Figure 2.2).

Figure 5.22

The geographic location preview (Figure 5.22 A) shows landscape issue only on the right area. The out of FOV region is land while the right boundary of TIRS is water. So there is an expected underestimation of the *stray light radiance* from the right area.

From the profile plot for band 10 in Figure 5.22 B, there is a nice improvement in pixel 1 - 3000, removing the "V" dip at pixel 2000. But no improvement on the jump in pixel 3500 - 4000 (0.1 $W/m^2 \cdot sr$) can be found after the correction. However, there is still somehow improvement in pixel 4000 - 6000. For band 11 profile plot in Figure 5.22 C, the uniformity in pixel 1 - 2000 and 4000 - 6000 is slightly improved after correction. But the jump in pixel 2000 is not reduced at all. The "V" dip at pixel 4000 is reduced slightly. Comparing the two blue after-correction lines, we can found that "V" dip around pixel 2000 is removed for band 10 while not for band 11, and the "V" dip at pixel 4000 keeps the same for band 10 while reduces in some degree for band 11. Again this also tells us that there is a performance difference between the two bands by correction of the

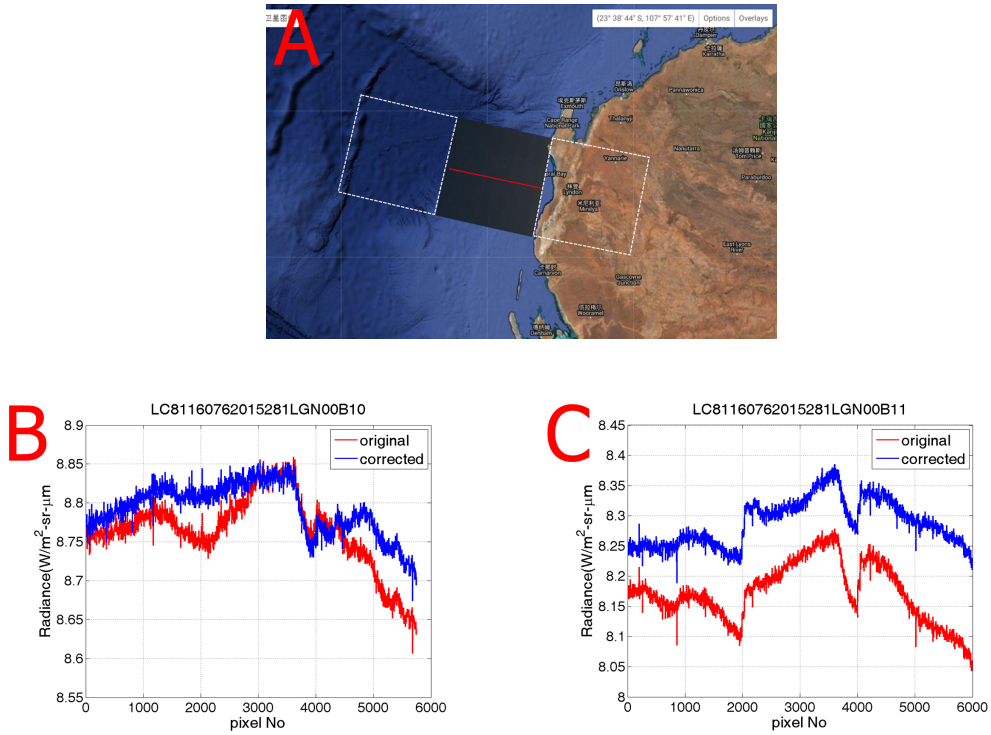

Figure 5.22: Geographic location preview of LC81160762015281LGN00 (A). Landscape issue shows on the right. Profile plots of band 10 (B) and 11 (C).

TIRS-on-TIRS algorithm.

Figure 5.23

The geographic location preview (Figure 5.23 A) shows landscape issue on the left part of the scene. For profile plot of band 10 in Figure 5.23 B, in pixel 3000 - 5500 the radiance becomes much more flat, but almost no change for the rest in terms of "banding". For profile plot of band 11 in Figure 5.23 C, the same improvement happens in pixel 3000 - 5500, and also no change for the rest. But one thing showing on both bands is that more sawtooth shows on the left half of the scene profiles while much less on the right. This is highly due to the pixel-wise effect from the landscape issue on the left.

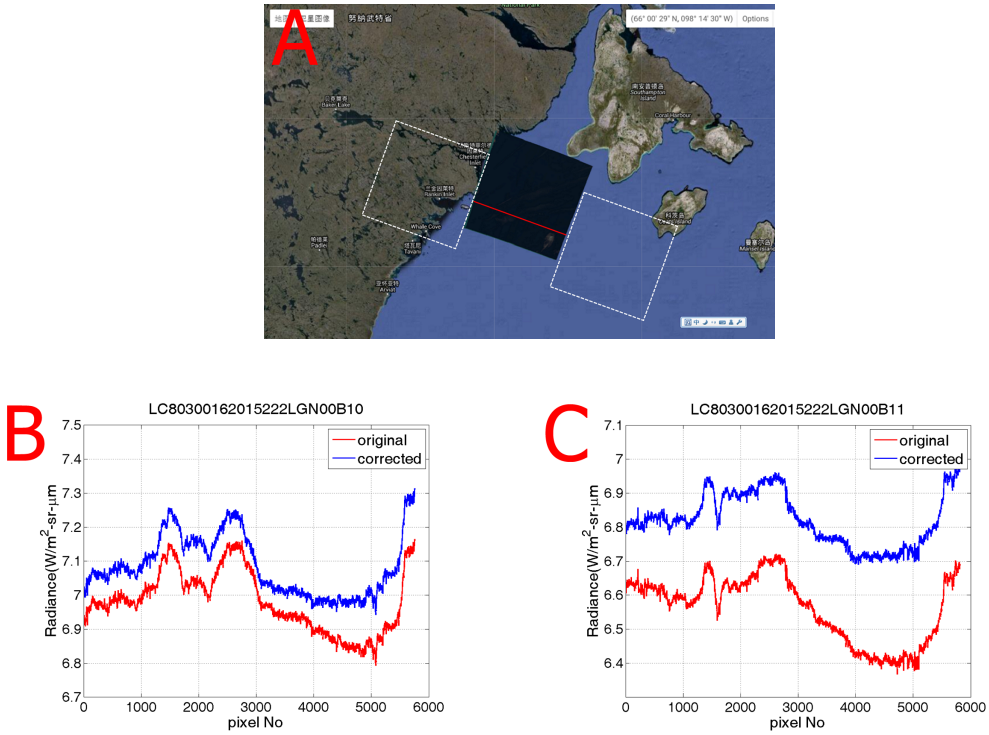

Figure 5.23: Geographic location preview of LC80300162015222LGN00 (A). Landscape issue shows on the left. Profile plots of band 10 (B) and 11 (C).

Profiles with Cloud Issue

In addition to the profiles with worst landscape issue, we also visually examine the ”banding” effect of profiles with cloud issue for the dataset without truth. We have four examples here. For each example, we will present the profile plots with cloud issue and the corresponding ones which have no cloud issue. In order to have a better comparison between the profile plots for ”banding”, we will center the profile plot by subtracting the mean.

Example 1: The first example is the scene located off the east coast of North Carolina, USA. The Landsat ID of the scene having the cloud issue is LC80150372014322LGN00 and the Landsat ID of the corresponding scene having no cloud issue is LC80150372014114LGN00.

For both scenes, the corresponding GOES image is used to confirm the cloud condition for the out of FOV region. Figure 5.24 shows the stacked GOES and TIRS image with cloud issue example on the left, and a corresponding example without cloud issue on the right. For both the background is GOES data; the whitish square is the TIRS image; the red line indicates the region of interest; the white dashed boxes are the out of FOV region contributing to the *stray light radiance* of the red line. The small images demonstrate the geographic situation of the scene.

For the scene on the left, there is obvious cloud issue on the right side of the scene, and a slight cloud issue on the left side. The cloudy area has lower radiance than the boundary of the TIRS. Therefore, the *TIRS-on-TIRS* algorithm is supposed to overestimate the *stray light radiance*. For the no-cloud-issue example on the right, there is no cloud or landscape issue present, this represents the best scenario case. Figure 5.25 illustrates the profile plots of the two in Figure 5.24.

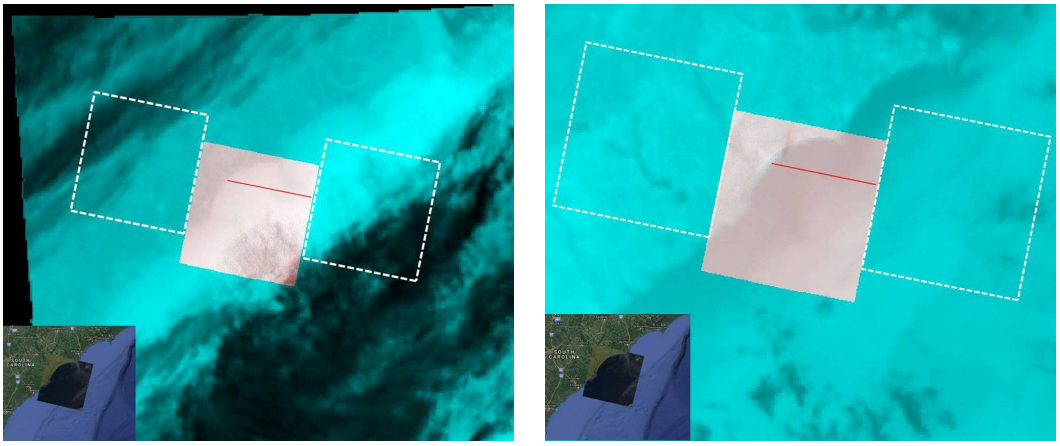

Figure 5.24: Stacked image of GOES and TIRS of the cloud-issue example as LC80150372014322LGN00 (left), and the no-cloud-issue example as LC80150372014114LGN00 (right). The small images show the geographic situation.

For band 10 profile plots, there is almost no difference between the original

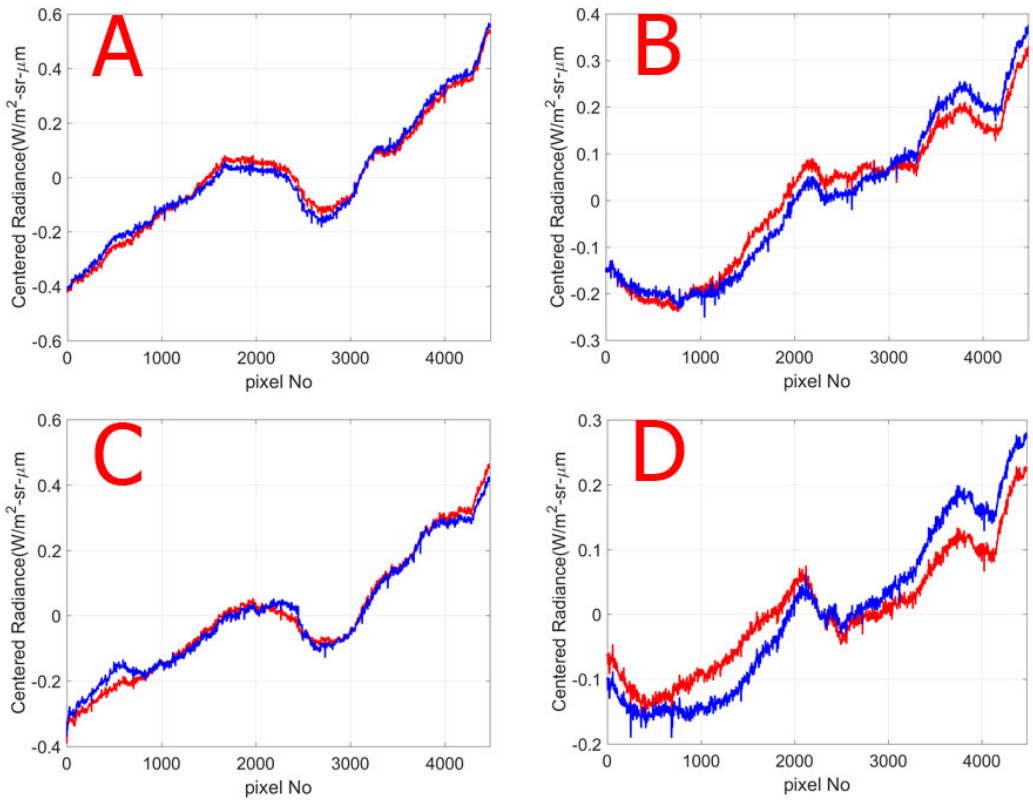

Figure 5.25: Profile plots of band 10 (A) and 11 (C) of LC80150372014322LGN00, and band 10 (B) and 11 (D) of LC80150372014114LGN00. Red lines are the original TIRS and blue lines are the corrected TIRS.

TIRS and the corrected TIRS for cloud-issue example (Figure 5.25 A). For the no-cloud issue example (Figure 5.25 B), a slight smaller peak-to-valley value, less "banding", in pixels 1 - 3000 is found after correction, and a better consistency between pixels 1 - 3000 and pixels 3000 - 4500. Generally, it can not be concluded that there is any worse performance of band 10 associated with the cloud issue for the example in Figure 5.24.

For the band 11 profile plots, the cloud-issue example (Figure 5.25 C) exhibits very limited difference between the original TIRS and the corrected TIRS, but a

little jump occurs at pixel 500 and pixel 2500 after correction. For the no-cloud-issue example (Figure 5.25 D), the corrected TIRS line is steeper than the original TIRS, and higher peak-to-valley value after correction. The sharp change in pixel 2000 Figure 5.25 D is more likely due to the residual error pattern (recalling Figure 5.13) and the ground truth change. According to the residual error analysis, there is only residual error pattern in band 11 but not in band 10. Therefore, the sharp change in pixel 2000 of band 10 in Figure 5.25 B is more likely due to ground truth change. However, the sharp change in pixel 2000 of band 11 in Figure 5.25 is sharper than that in band 10 (Figure 5.25 B). Therefore, the combination of ground truth change and residual error should be responsible for that.

Comparing Figure 5.25 C and D, only the jumps in pixel 500 and pixel 2500 in Figure 5.25 C are suspected to be caused by the cloud issue.

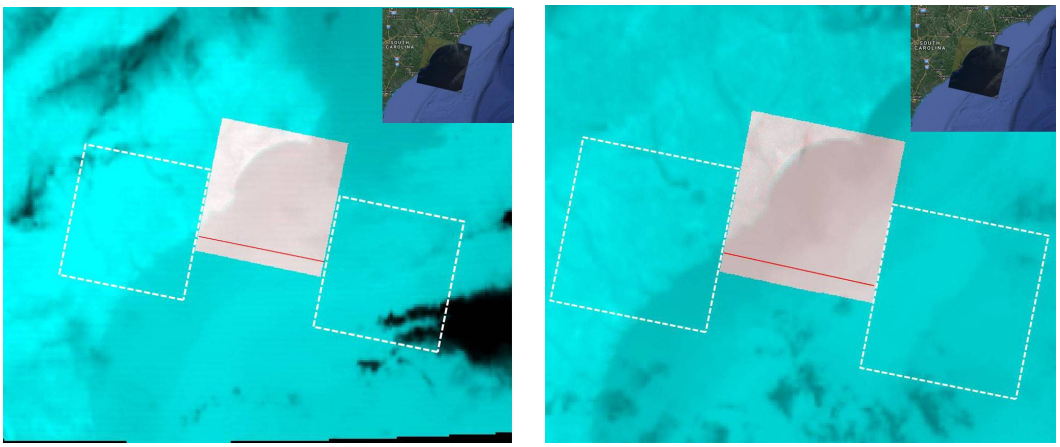

Figure 5.26: Stacked image of GOES and TIRS of the cloud issue example as LC80150372016120LGN00 (left), and the no cloud isseue examle as LC80150372014114LGN00 (right). Small image shows the geographic location of the scene presenting slight landscape issue on the left side.

Example 2: The second example is from the same location as the first one. The Landsat ID of the cloud-issue example scene is LC80150372016120LGN00. The

Landsat ID of the no-cloud-issue example is used for comparison: LC80150372014114LGN00. Figure 5.26 shows the stacked GOES and TIRS images. The red line and the white dashed boxes share the same meanings as in Figure 5.24. In Figure 5.26, there is slight cloud (black area) showing on the right side, along with the landscape issue on the left (verified by the small image). For the no-cloud-issue example, there is the same landscape issue on the left and no landscape or cloud issue on the right.

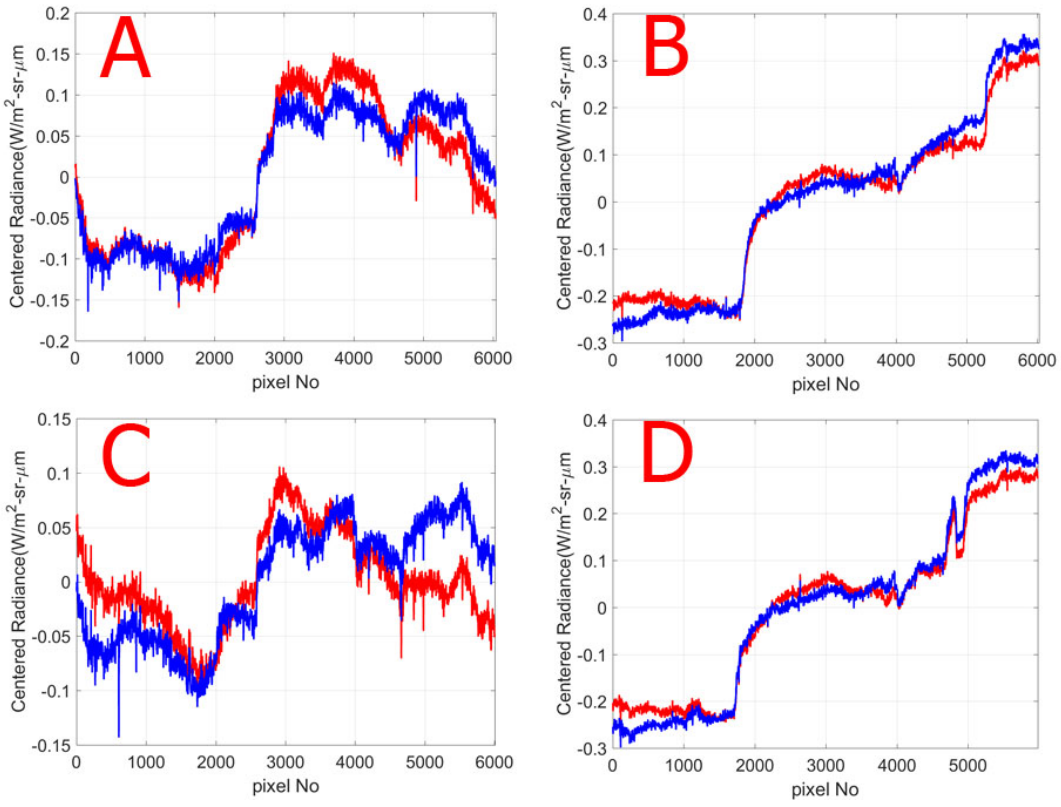

Figure 5.27: Profile plots of band 10 (A) and 11 (C) of LC80150372016120LGN00, and band 10 (B) and 11 (D) of LC80150372014114LGN00. Red lines are the original TIRS and blue lines are the corrected TIRS.

For band 10 profile plots, cloud issue example (Figure 5.27 A) presents a smaller peak-to-valley value in pixels 3000 - 6000, hence less ”banding”, after the

correction, but a slight increase in pixel 2000 compared to the original TIRS. For the no cloud issue example (Figure 5.27 B), variance in pixels 2000 - 4000 is almost removed by the correction, but a higher peak-to-valley value in pixels 4000 - 6000 after correction.

For band 11 profile plots, cloud issue example profile plot (Figure 5.27 C) showed that the variance in pixels 2500 - 6000 is reduced a lot in general but there is no improvement for the sudden decreases at pixel 3000 and 4000 after correction. The spike in pixel 3000 is reduced but not removed. The corresponding no-cloud-issue example profile plot (Figure 5.27 D) demonstrated slightly less variance in pixels 2000 - 4000, but no changes of the spike in pixel 4800. There is a slight change in the profile plot in pixels 1- 1800 and a shift for profile plot in pixels 5000 - 6000.

The sudden increase in pixel 1800 is found in both band 10 and 11 for the no-cloud-issue example. Therefore, this is considered to be caused by the ground truth change. There is also a sudden increase in pixel 2500 in band 10 (Figure 5.27 A) and 11 (Figure 5.27 C) in the cloud-issue example. The very limited cloud issue on the right side would not be suspected of being responsible for such a sharp change. This sharp change would be more likely to be caused by the ground truth change and maybe as well as the landscape issue on the left side. Moreover, the sudden decrease in pixel 4000 is only found in band 11 (Figure 5.27 C) while not in band 10 (Figure 5.27 A). Considering the only difference between band 10 and 11 would be the residual error pattern, we would expect that the residual error pattern is responsible for this sharp decrease. The trend lines of the two examples show big difference. Also the very limited cloud would not be expected having a big effect on the ”banding”. For this example, cloud issue presents very limited effect on the ”banding”.

Example 3: The third example is a scene from the Gulf of Mexico, south of Alabama, USA. The Landsat ID of the cloud-issue scene is LC80200392016219LGN00. The Landsat ID of the corresponding no-cloud-issue scene is LC80200392016283LGN00.

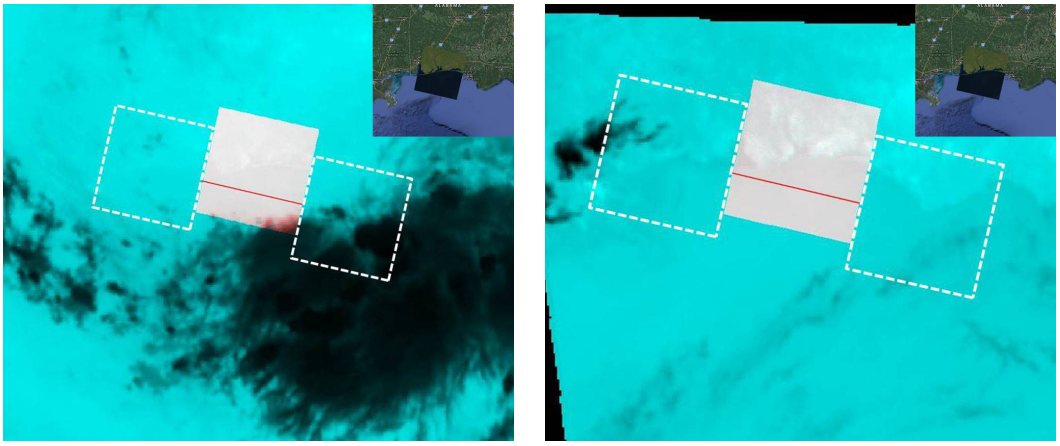

Figure 5.28: Stacked image of GOES and TIRS of the cloud-issue example as LC80200392016219 (left), and the no-cloud-issue example as LC80200392016283LGN00 (right). Small image shows the geographic situation.

Figure 5.28 plots the GOES and TIRS stacked images of the cloud issue on the left and the corresponding no-cloud-issue example on the right. The red lines and white dashed boxes share the same meaning as in previous examples. For the cloud issue example on the left, there is a clear cloud issue on the right side and some landscape issue on the left. For the no-cloud-issue example, a similar landscape issue occurs on the left side and none on the right side.

Figure 5.29 plots the profiles of the two examples in this case. All red lines are the profile plots of original TIRS and all blue lines are profile plots of the corrected TIRS with *TIRS-on-TIRS* algorithm.

For band 10 profile plots, the cloud issue example (Figure 5.29 A) exhibited a significant change of dip in pixel 2000, a big reduce for the spike in pixels 3500 - 3800 and a smooth increase in pixels 4000 - 6000 after correction. The no-cloud-issue profile plot (Figure 5.29 B) showed a drop of peak-to-valley value in pixels 2200 - 6000. Cross comparison between the blue lines in Figure 5.29 A and B showed that the spike in pixel 2000 is highly due to the cloud issue, which is only

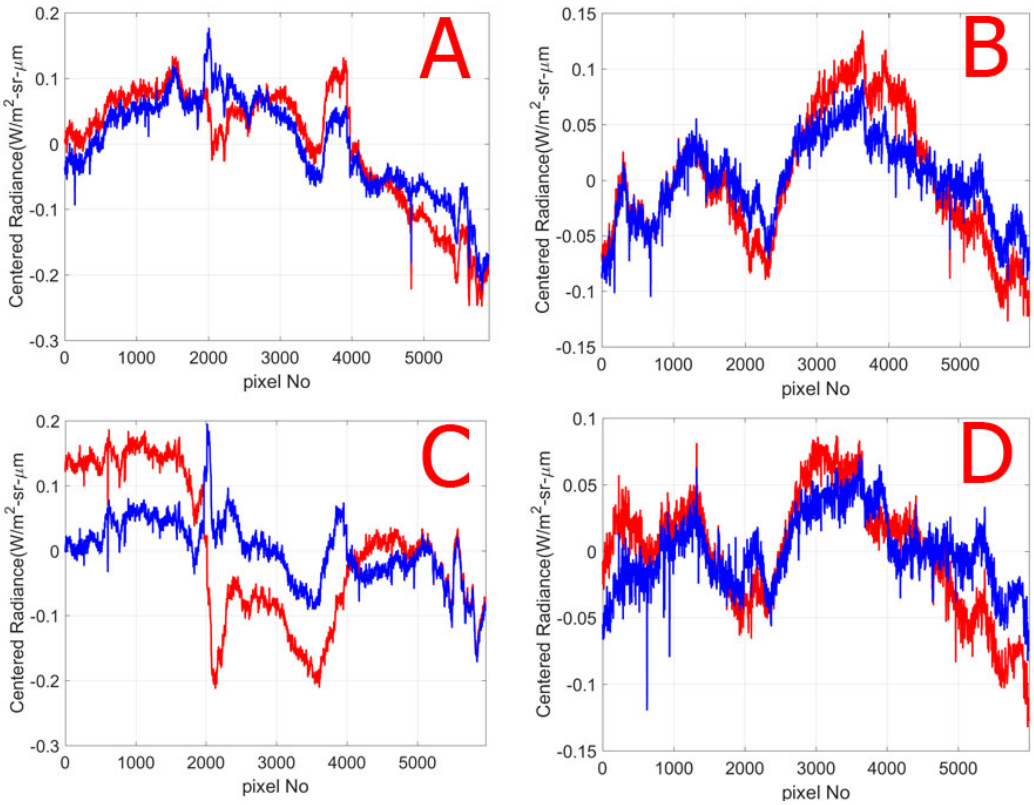

Figure 5.29: Profile plots of band 10 (A) and 11 (C) of LC80200392016219LGN00, and band 10 (B) and 11 (D) of LC80200392016283LGN00. Red lines are the original TIRS and blue lines are the corrected TIRS.

showing on cloud issue plot, because the ground truth has low chance of having such a dramatic change in such small area in open sea.

For the band 11 profile plots, the cloud-issue example (Figure 5.29 C) presented a big reduced peak-to-valley value overall except no improvement for the spike in pixel 2000 or the variance in pixels 5000 - 6000. The no-cloud-issue example plot (Figure 5.29 D) demonstrated a smaller overall peak-to-valley value after correction, and a sudden decrease showing in pixel 4000 after correction. Comparing the corrected blue lines in Figure 5.29 C and the blue line in Figure 5.29 D showed

the spike in pixels 2000 and 4000, only shown in the cloud issue example, could be due to the cloud issue.

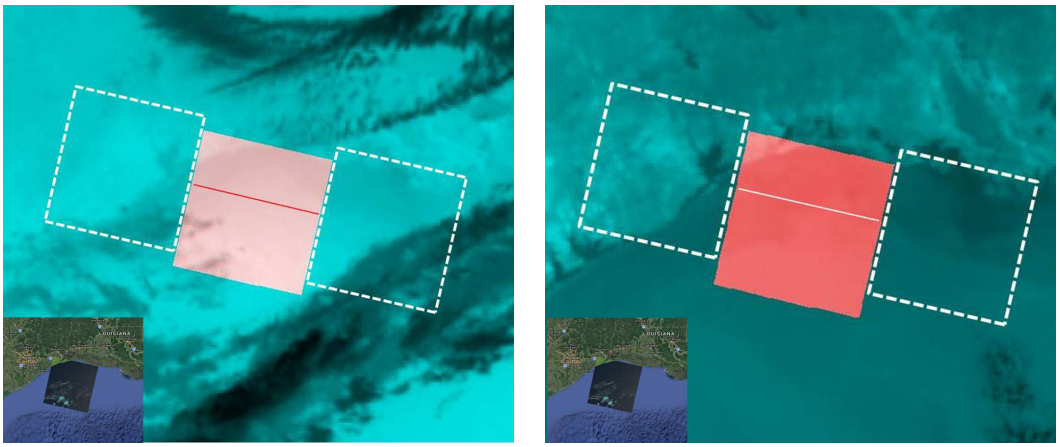

Figure 5.30: Stacked image of GOES and TIRS of the cloud issue example LC80240402014017LGN00 (left), and the no cloud issue example as LC80240402014289LGN00 (right). Small image shows the geographic situation.

Example 4: The last example is another scene in the Gulf of Mexico, south of Texas, USA. The Landsat ID of the cloud issue scene is LC80240402014017LGN00. The Landsat ID of the corresponding no cloud issue scene isLC80240402014289LGN00. Figure 5.30 shows the stacked GOES and TIRS image of the cloud-issue example on the left and the no-cloud-issue example on the right. Again, the red line and the white dashed boxes share the same meanings as in previous examples. From the stacked image, the cloud-issue example showed a mediate cloud issue on the right side and some landscape issue on the left side. The no-cloud-issue example shows the same landscape issue on the left and none on the right area.

For band 10 profile plots, the cloud-issue example (Figure 5.31 A) showed almost no change after the correction except a slightly higher peak-to-valley value in pixels 3000 - 6000. The no-cloud-issue example profile plot (Figure 5.31 B) demonstrated more variance in pixels 1500 - 3500, a shift in pixels 3500 - 4000.

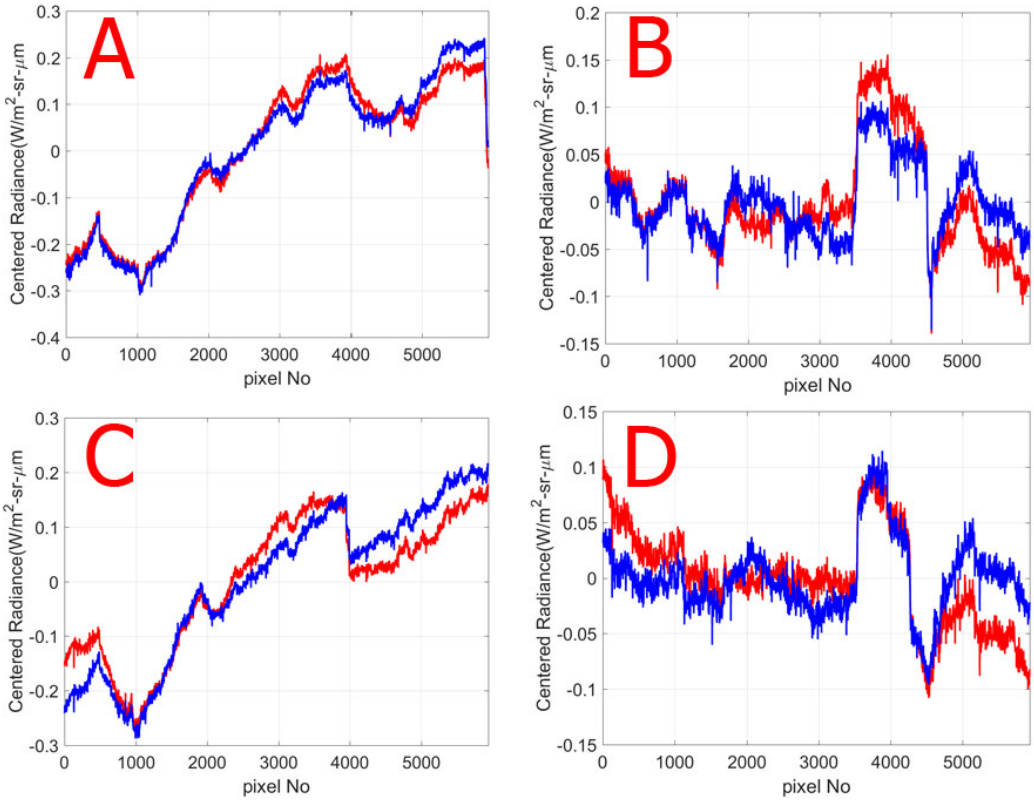

Figure 5.31: Profile plots of band 10 (A) and 11 (C) of LC80240402014017LGN00, and band 10 (B) and 11 (D) of LC80240402014289LGN00. Red lines are original TIRS and blue lines are corrected TIRS.

The significant difference between the trend lines of the two prevents concluding the impact of the cloud issue through comparing the blue lines in Figure 5.31 A and B.

For band 11 profile plots, the cloud-issue example (Figure 5.31 C) showed a shift in pixels 1 - 1000, a less variance in pixels 2000 - 4000 and a shift in pixels 4000 - 6000 after correction. The sharp decrease in pixel 4000 still exists after correction. The no-cloud-issue profile plot (Figure 5.31 D) illustrates a small change in pixels 1 - 1000, a small spike in pixel 2000, and some shift in pixels 4000 - 6000. Comparing

the blue lines in Figure 5.31 C and D showed that the sharp decrease in pixel 4000, showing in Figure 5.31 C and D but not in Figure 5.31 A, is highly due to the residual error of band 11 recalling Figure 5.13, and may be partially due to the landscape issue on the left but not entirely. Also more high-frequency variance in pixels 2000 - 6000 than in pixels 1 - 1000 for Figure 5.31 C, which is not shown in Figure 5.31 D, is highly due to cloud issue in Figure 5.31.

5.3 Summary

Results of the dataset with truth and the dataset without truth are presented and analyzed above. Here we will have a summary of both datasets and cross compare the performance between scenarios. We will also compare the performance of the *TIRS-on-TIRS* algorithm on different materials.

For the dataset with truth (MODIS), Table 5.9 lists the summary of absolute radiometric error. In the table, numbers are changes in percentage calculated as $(|Before| - |After|) \,/\, |Before|$, where $Before$ and $After$ are the mean from previous summary tables. Therefore, a positive value means decrease and an negative value means increase. The number in the parentheses is the absolute error after correction in terms of radiance and K. For profiles from the desert scenes, the absolute radiometric error increases after correction for both bands, more for band 11 than for band 10. But in absolute sense, the absolute error after correction is -0.1179 for band 11, which is lower than -0.3374 for band 10. This increasing and abnormal high error may be caused by the time difference (10-25 min) between MODIS and TIRS. MODIS collected the data from desert later than the TIRS. The temperature on desert can increase dramatically due to the properties of desert. The collecting time of those desert scenes is around 9 am. Therefore, there is a high chance that the ground temperature of desert is higher for MODIS than TIRS. In hence, the absolute is negative and increasing after correction. For profiles from the water scenes and the snow scenes, the absolute radiometric error decreases

for both bands. Moreover, it decreases more for profiles with best scenario than those with landscape issue and cloudy issue for both bands. The absolute error decreases a comparable percentage of profiles with landscape issue and cloud issue for band 10. But for band 11, the absolute error decreases more of profiles with cloud issue than profiles with landscape issue from the water scenes, but more of profiles with landscape issue than those with cloud issue from the snow scenes. This may be due to the limited effect of landscape issue on snow scenes, as the snow scenes are from Iceland and Dome C, where the out of FOV region is ice or very cold water having close radiance as the boundary of TIRS. Therefore, the existing landscape issue does not have that much effect on absolute error. In absolute scene, after correction the profiles from the water scenes have lower absolute error than those from the desert scenes and the snow scenes. This is not surprising as the absolute radiometric calibration uses buoy data, which is from surface water. Therefore, the calibration will have the best performance on the radiance range of water scenes. But one good thing that can be found is that profiles from the snow scenes have just slight higher errors than those from the water scenes. For profiles from the desert scenes, the absolute error is much higher especially for band 10. Considering that the goal of the Landsat program is providing data for land especially for farming works, the high accuracy in the range of water can satisfy the mission. But low or very high radiance level data of TIRS need more corrections before being used as high accuracy data. Table 5.10 shows the standard deviation (”banding” effect) change in percentage after correction as well as for the absolute error. The calculation is the same as Table 5.9. The number in the parentheses is the standard deviation after correction. Overall, the ”banding” effect is reduced for all but profiles with cloud issue from the desert scenes for band 11. Firstly, we compare the performance difference for band 10 and 11. For best scenario, the ”banding” effect is removed more for band 10 than band 11 of profiles from the desert scenes, more for band 11 than band 10 of profiles for the water scenes, and a comparable amount for band 10

		Desert	Water	Snow
B10	Best Scenario	-30%(-0.337,≈ -3.4K)	69%(0.033,≈ 0.3K)	53%(0.090,≈ 0.9K)
	Landscape Issue	NA	44%(-0.060,≈ -0.6K)	31%(0.091,≈ 0.9K)
	Cloudy Issue	2%(-0.247,≈ -2.5K)	16%(-0.088,≈ -0.9K)	90%(-0.025,≈ -0.2K)
B11	Best Scenario	-300%(-0.118,≈ -1.2K)	52%(0.070,≈ 0.7K)	86%(0.073,≈ 0.7K)
	Landscape Issue	NA	15%(0.071,≈ 0.7K)	77%(0.090,≈ 0.9K)
	Cloudy Issue	36%(-0.157,≈ -1.6K)	40%(0.046,≈ 0.5K)	96%(-0.020,≈ -0.2K)

Table 5.9: Absolute radiometric error changes in percentage $(|Before| - |After|)/|Before| * 100\%$, negative means absolute error increases after correction. (Numbers in parentheses is absolute error after correction, also convert to K unit.)

and 11 of profiles from the snow scenes. More "banding" effect is removed for band 11 than band 10 of profiles with landscape issue from the water scenes and the snow scenes. For cloud issue, the standard deviation does not change much for both bands of profiles from the desert scenes, but it decreases of profiles from the snow scenes and the water scenes. Due to the limited available profiles with cloud issue and inconsistency of these profiles, no certain conclusion should be drawn. Overall, the "banding" effect is reduced around 50% after the *TIRS-on-TIRS* correction. Furthermore, more is removed for band 11 than band 10. In an absolute sense, after correction, the standard deviation is higher for band 11 than band 10 of all profiles but those with cloud issue from the desert scenes and the snow scenes. The "banding" effect is removed through the correction more in band 11 than band 10 relatively but still it has more "banding" for band 11 than band 10 after correction, which is confirmed by the residual error pattern for band 11. The standard deviation of all profiles with landscape issue is higher than those with best scenario. This makes sense as the error introduced by the approximation of the *TIRS-on-TIRS* algorithm of profiles with landscape issue. But for the profiles with cloud issue, it is higher than best scenario for all but not an unanimous relationship with profiles with landscape issue. To sum up,

the "banding" effect is reduced at most cases, and a little high of profiles with landscape issue but unpredictable of profiles with cloud issue.

The residual error of profiles with best scenario shows a residual error pattern for band 11 after correction, but almost none for band 10. This explains why the standard deviation after correction for band 11 is always higher than that for band 10. As the training data takes no difference between band 10 and 11, this is highly suspect to be an error from the optical model and/or the limitation of lunar collection. This should be taken into consideration if there is a further calibration.

		Desert	Water	Snow
B10	Best Scenario	40%(0.029)	49%(0.014)	46%(0.0153)
	Landscape Issue	NA	40%(0.019)	52%(0.019)
	Cloudy Issue	0.3%(0.174)	50%(0.017)	20%(0.034)
B11	Best Scenario	25%(0.033)	63%(0.016)	47%(0.026)
	Landscape Issue	NA	48%(0.023))	62%(0.027)
	Cloudy Issue	-4%(0.147)	34%(0.0182)	59%(0.031)

Table 5.10: Standard deviation changes in percentage $(|Before| - |After|)/|Before| * 100\%$, negative means standard deviation increases after correction.(numbers in parentheses is standard deviation of the profile after correction)

For the dataset without truth, two parts are analyzed: consistency of the absolute radiometric error and the visual examination of profiles with worst landscape issue and cloud issue. The first part has similar procedure as the dataset with truth but different metrics. This part shows the consistency of the absolute radiometric changes between the dataset with truth and the dataset without truth. The plot shows that the change in the dataset without truth is highly consistent with that of the dataset with truth. This shows that the absolute radiometric error after correction is the same as those with truth. Therefore, the good performance on the dataset with truth of the absolute radiometric error, from -0.0960 to -0.0434 (band 10), from -0.1081 to -0.0700 (band 11), stands for the regular time. For the

second part, the visual examination of the ”banding” effect, there are 13 selected scenes with the severe landscape issue, most of which are along the coastline of different continents. Firstly, for all scenes, the profiles become smoother after correction for both band 10 and 11. Therefore, the *TIRS-on-TIRS* algorithm will not make the ”banding” effect worse even in the most severe situations. But there are usually two jumps for most profiles from most scenes after the correction, which is reduced but not removed totally. The jump will be around 0.05 radiance (around 0.5 K), which is partially due to the approximation made by the *TIRS-on-TIRS* algorithm. For those scenes where the boundary of TIRS is highly parallel with the coastline of the continent, the landscape issue will make 2/3 of the scene like sawtooth due to the different effect of landscape issue on different pixels. For the scenes with cloud issue, firstly the cloud issue does not make ”banding” worse among the four examples in general. But it is very difficult to draw a conclusion of how cloud issue affects the ”banding” effect. Because the ground truth varies a lot from the cloud issue scenes to the corresponding no cloud issue scenes, the ”banding” effect is overwhelmed by the ground truth variance. Moreover, these water scenes are all along the coastline of US, so these scenes have more or less landscape issue. The mixture of cloud issue and landscape issue and the variance of the ground truth makes it difficult to conclude the impact of the cloud issue on ”banding”.

Chapter 6

Summary and Future Work

6.1 Summary

Stray light issue caused by the defect in hardware in TIRS instrument was found. So far, there is no operational correction algorithm used. Two correction methodologies were proposed, using and external data and using an internal data (*TIRS-on-TIRS*). The *TIRS-on-TIRS* algorithm has the advantage of using TIRS data only, simplifying the operational procedure.

In this article, a comprehensive evaluation of the *TIRS-on-TIRS* stray light correction algorithm is addressed. There were two methodologies for the evaluation based on if there are the corresponding truth data (MODIS).

Before using MODIS as truth, pre-processing of MODIS is explored: band shape adjustment and exploration of view angle correction. It is found to be a linear relationship between band 10 (TIRS) and band 31 (MODIS), and between band 11 (TIRS) and band 32 (MODIS) through 936 MODTRAN simulations. The simulations include all combinations of atmospheric conditions, three types of material, and wide ground temperature range. This adjustment processing reduces the RMS error from 0.093 to 0.044 (band 10), and from 0.115 to 0.042 (band

11). For view angle issue, there should be a correction of MODIS for the data where MODIS and TIRS have different view angles. With the 6,552 MODTRAN simulations, through the controlling variable analysis and the theoretical analysis, ground temperature is found to have the biggest effect on the view angle issue, followed by atmosphere model and water vapor content. Material has almost no effect on view angle issue, as the emissivity of the three materials are very similar to each other on the spectral band windows. One operational example showed that it is very difficult to conduct a precise correction for a water scene with the available data, because the scene has a wide range of water vapor. But for the clear snow scenes, it is not necessary to do the correction for using MODIS data within 30° for our dataset. So for the datasets we will use, view angle correction is not necessary.

After applying the band shape adjustment, MODIS is used as the truth data to be compared with the original TIRS data and the corrected TIRS. The absolute radiometric error and the "banding" effect are evaluated through two metric: mean of radiance difference and standard deviation of radiance difference. For absolute error, it increases for both bands of profiles from the desert scenes (due to the time difference between MODIS and TIRS), and decreases for both bands of profiles from the snow scenes and the water scenes, especially very good performance of profiles from the snow scenes. Landscape issue is found to have limited impact on the absolute error. Data with cloud issue shows more effect than those with landscape issue. But the limited data amount prevents a solid conclusion about cloud issue.

For the standard deviation, it reduces around 40% for band 10 and 11 of profiles with best scenario. As expected, profiles with landscape issue have slightly higher standard deviation than those with best scenario. For profiles with cloud issue, the absolute error is higher of profiles from the water scenes but lower of those from the snow scenes compared to profiles with best scenario. Furthermore, profiles from the desert scenes have low consistency with each other. Again

for the unpredictable cloudy issue, limited data make it difficult to draw a clear conclusion how much impact it has.

But from the residual error analysis, there is a clear residual error pattern for band 11 after the correction but none for band 10. This is highly suspect to be resulting from the optical model, which is based on the lunar collection. To sum up, after correction, for best scenario, both the absolute radiometric error and the "banding" effect are reduced significantly of profiles from both snow scenes and water scenes but not desert scenes. Landscape issue has almost no effect on the absolute radiometric error but some effect on the "banding" effect. Cloud issue has comparable effect on the "banding" as the landscape issue and varying effect on the absolute radiometric error. Also because cloud issue can vary dramatically from scene to scene, even within the same scene, it is hard to have a final conclusion for cloud issue.

For the dataset without truth, two parts are analyzed: consistency of absolute radiometric error and a visual examination of the "banding" effect of profiles with the worst landscape issue. For consistency of absolute radiometric error, it is an indirect way to show that the radiometric change after correction of the dataset without truth is consistent with that of the dataset with truth. For visual examination of the "banding" effect, 13 chosen scenes with the most severe landscape issue are analyzed one by one with the profile of the original TIRS and the corrected TIRS. Firstly, the *TIRS-on-TIRS* algorithm does make the profile smoother (less "banding") in general even for profiles with the worst landscape issue. But there are still two or three jumps of the profile mostly on the boundaries of SCAs, and the biggest jump is around $0.05W/m^2 \cdot sr$. Furthermore, landscape issue in some degree will make part of the profile sawtooth due to the pixel-wise effect from landscape issue. To sum up, firstly the absolute radiometric error on regular days is consistent with that with truth. For "banding" effect the *TIRS-on-TIRS* algorithm removes the "banding" effect in some degree even of the profiles with the worst landscape issue, but still jumps occur on the boundaries of SCAs.

No solid conclusion can be made of the impact of cloud issue on the ”banding” effect for the dataset without truth due to the mixture of landscape issue and cloud issue and the large variance between the ground truth.

6.2 Future Work

Generally the *TIRS-on-TIRS* algorithm shows a stable and good performance on all different situations. But there is also a residual pattern for band 11 but not for band 10. This should be an important part if there is a further-calibration algorithm. For absolute error, the calibration of TIRS utilized only the radiance range of water. Therefore, the absolute error is minimized for this specific range. But the error from snow scenes is usually higher than those from water scenes. The absolute error from desert scenes becomes higher after the correction, which is highly caused by the time difference between MODIS and TIRS. The mission of TIRS is providing data for farming work in the US continent, which requires high precision on a certain radiance range close with water scenes. Therefore,the high absolute error in desert would not be a concern. But this should be taken into consideration if there is a further calibration. Also, more precise calibration of view angle is necessary if large view angle MODIS needs to be used as truth.

Bibliography

[1] Gerace, A., [*Demonstrating Landsat's new potential to monitor coastal and inland waters*], Rochester Institute of Technology (2010).

[2] Jensen, J. R. and Lulla, K., "Introductory digital image processing: a remote sensing perspective," (1987).

[3] "National Aeronautics and Space Administration landsat program." `http://landsat.gsfc.nasa.gov/?page_id=2`. Accessed: 2015-8-10.

[4] Roy, D. P., Wulder, M., Loveland, T., Woodcock, C., Allen, R., Anderson, M., Helder, D., Irons, J., Johnson, D., Kennedy, R., et al., "Landsat-8: Science and product vision for terrestrial global change research," *Remote Sensing of Environment* **145**, 154–172 (2014).

[5] "United State Geological Survey landsat 8 program." `http://landsat.usgs.gov/landsat8.php`. Accessed: 2015-8-10.

[6] Montanaro, M., Gerace, A., and Rohrbach, S., "Toward an operational stray light correction for the landsat 8 thermal infrared sensor," *Applied Optics* **54**(13), 3963–3978 (2015).

[7] Schott, J. R., Gerace, A., Raqueno, N., Ientilucci, E., Raqueno, R., and Lunsford, A. W., "Chasing the tirs ghosts: Calibrating the landsat 8 ther-

mal bands," in [*SPIE Optical Engineering+ Applications*], 92181A–92181A, International Society for Optics and Photonics (2014).

[8] Gerace, A., Montanaro, M., Beckmann, T., Tyrrell, K., Cozzo, A., Carney, T., and Ngan, V., "Tirs stray light correction: algorithms and performance," in [*SPIE Optical Engineering+ Applications*], 96070Q–96070Q, International Society for Optics and Photonics (2015).

[9] Jhabvala, M., Reuter, D., Choi, K., Jhabvala, C., and Sundaram, M., "Qwip-based thermal infrared sensor for the landsat data continuity mission," *Infrared Physics & Technology* **52**(6), 424–429 (2009).

[10] Montanaro, M., Gerace, A., Lunsford, A., and Reuter, D., "Stray light artifacts in imagery from the landsat 8 thermal infrared sensor," *Remote Sensing* **6**(11), 10435–10456 (2014).

[11] Reuter, D. C., Richardson, C. M., Pellerano, F. A., Irons, J. R., Allen, R. G., Anderson, M., Jhabvala, M. D., Lunsford, A. W., Montanaro, M., Smith, R. L., et al., "The thermal infrared sensor (tirs) on landsat 8: Design overview and pre-launch characterization," *Remote Sensing* **7**(1), 1135–1153 (2015).

[12] "United States Geologial Survey earthexplorer." `http://earthexplorer.usgs.gov/`. Accessed: 2015-8-10.

[13] "United States Geologial Survey glovis." `http://glovis.usgs.gov/`. Accessed: 2015-8-10.

[14] "United States Geologial Survey landsatlook viewer." `http://landsatlook.usgs.gov/`. Accessed: 2015-8-10.

[15] Markham, B., Barsi, J., Kvaran, G., Ong, L., Kaita, E., Biggar, S., Czapla-Myers, J., Mishra, N., and Helder, D., "Landsat-8 operational land imager radiometric calibration and stability," *Remote Sensing* **6**(12), 12275–12308 (2014).

[16] Knight, E. J. and Kvaran, G., "Landsat-8 operational land imager design, characterization and performance," *Remote Sensing* **6**(11), 10286–10305 (2014).

[17] Montanaro, M., Levy, R., and Markham, B., "On-orbit radiometric performance of the landsat 8 thermal infrared sensor," *Remote Sensing* **6**(12), 11753–11769 (2014).

[18] Montanaro, M., Lunsford, A., Tesfaye, Z., Wenny, B., and Reuter, D., "Radiometric calibration methodology of the landsat 8 thermal infrared sensor," *Remote Sensing* **6**(9), 8803–8821 (2014).

[19] Barsi, J. A., Schott, J. R., Hook, S. J., Raqueno, N. G., Markham, B. L., and Radocinski, R. G., "Landsat-8 thermal infrared sensor (tirs) vicarious radiometric calibration," *Remote Sensing* **6**(11), 11607–11626 (2014).

[20] Hook, S. J., Chander, G., Barsi, J., Alley, R. E., Abtahi, A., Palluconi, F. D., Markham, B. L., Richards, R. C., Schladow, S. G., Helder, D. L., et al., "In-flight validation and recovery of water surface temperature with landsat-5 thermal infrared data using an automated high-altitude lake validation site at lake tahoe," *Geoscience and Remote Sensing, IEEE Transactions on* **42**(12), 2767–2776 (2004).

[21] "National Aeronautics and Space Administration lunar collection." `http://landsat.gsfc.nasa.gov/wp-content/uploads/2014/10/20141031_nu4.png`. Accessed: 2015-8-10.

[22] "National Aeronautics and Space Administration modis." `http://modis.gsfc.nasa.gov/about/specifications.php`. Accessed: 2015-10-28.

[23] Xiong, X., Chiang, K., Esposito, J., Guenther, B., and Barnes, W., "Modis on-orbit calibration and characterization," *Metrologia* **40**(1), S89 (2003).

[24] Xiong, X. and Barnes, W., "An overview of modis radiometric calibration and characterization," *Advances in Atmospheric Sciences* **23**(1), 69–79 (2006).

[25] Barnes, W. L., Xiong, X. J., and Salomonson, V. V., "Status of terra modis and aqua modis," in [*Geoscience and Remote Sensing Symposium, 2002. IGARSS'02. 2002 IEEE International*], **2**, 970–972, IEEE (2002).

[26] Xiong, X., Chiang, K., Guenther, B., and Barnes, W. L., "Modis thermal emissive bands calibration algorithm and on-orbit performance," in [*Third International Asia-Pacific Environmental Remote Sensing Remote Sensing of the Atmosphere, Ocean, Environment, and Space*], 392–401, International Society for Optics and Photonics (2003).

[27] Xiong, X., Chiang, K.-F., Wu, A., Barnes, W. L., Guenther, B., and Salomonson, V. V., "Multiyear on-orbit calibration and performance of terra modis thermal emissive bands," *Geoscience and Remote Sensing, IEEE Transactions on* **46**(6), 1790–1803 (2008).

[28] Hook, S. J., Vaughan, R. G., Tonooka, H., and Schladow, S. G., "Absolute radiometric in-flight validation of mid infrared and thermal infrared data from aster and modis on the terra spacecraft using the lake tahoe, ca/nv, usa, automated validation site," *Geoscience and Remote Sensing, IEEE Transactions on* **45**(6), 1798–1807 (2007).

[29] Ientilucci, E. J., "Using modtran: predicting sensor-reaching radiance," *Chester F. Carlson Center for Imaging Science. Rochester Institute of Technology* (2007).

[30] "MODIS UCSB Emissivity Library material emissivity." `http://www.icess.ucsb.edu/modis/EMIS/html/em.html`. Accessed: 2016-01-28.

[31] "National Aeronautics and Space Administration sea surface temperature."

http://www.ospo.noaa.gov/Products/ocean/sst.html. Accessed: 2015-9-1.

[32] "Dome C dome concordia in antractic area." http://www.gdargaud.net/Antarctica/Concordia.html. Accessed: 2015-06-20.

Appendices

Appendix A

Band Shape Adjustment of GOES to TIRS

Geostationary Operational Environmental Satellite system (GOES) supports weather forecasting, severe storm tracking, and meteorology research on United States. It has been used providing sampled *stray light radiance* from the out of FOV region, because band 4 of GOES has similar spectral band window to that of band 10 of TIRS. But due to the low requirement, GOES is not a well calibrated instrument. This section explores the band adjustment from GOES to TIRS. Figure A.1 shows the relative sensor response of band 4 of GOES 15 and band 10, 11 of TIRS. From the plot, it is clear that almost there is total overlap between band window of band 4 of GOES and that of band 10 of TIRS, but none between band 4 of GOES and that of band 11. Therefore, a good band shape adjustment is expected from band 4 of GOES to band 10, and a high error from band 4 of GOES to band 11 of TIRS.

Similar to the band shape adjustment from MODIS to TIRS, 936 MODTRAN simulations are used to derive the band shape adjustment function and error analysis. Three different materials are used in the simulations: snow, sea water and sand. Six different atmosphere models are used: the tropical atmosphere model, the mid-latitude summer atmosphere model, the mid-latitude winter atmosphere

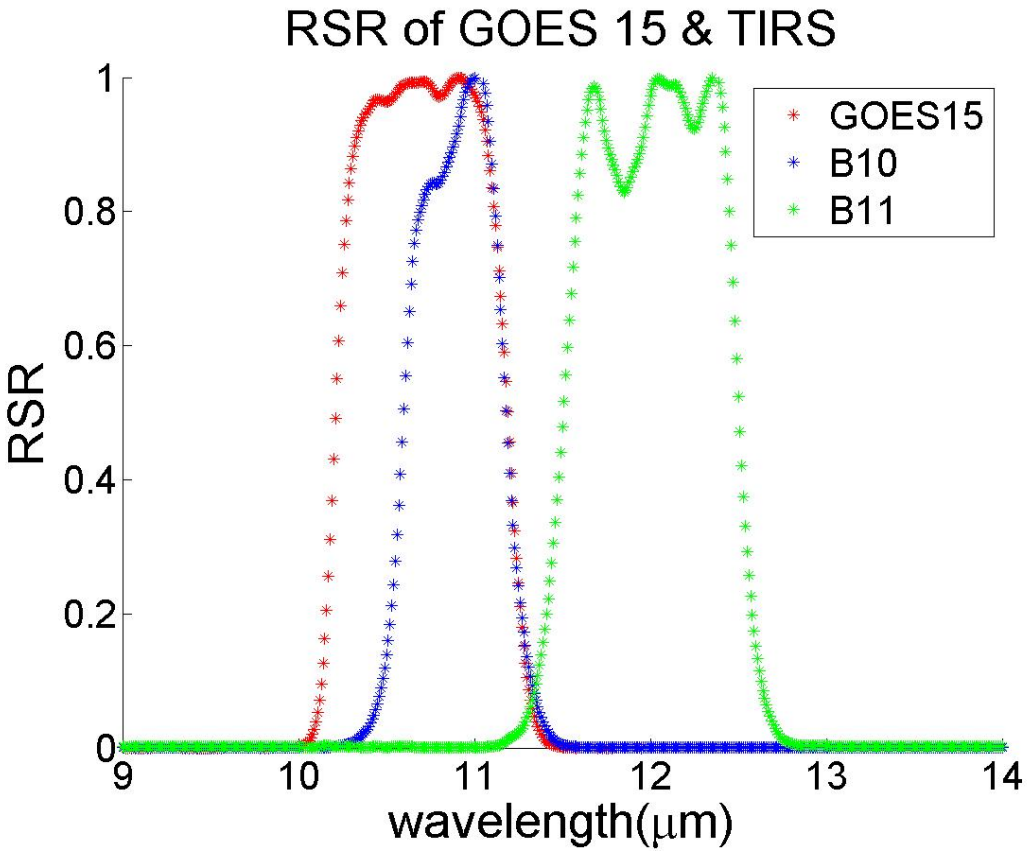

Figure A.1: Relative Sensor Response (RSR) of band 4 of GOES 15 and band 10, 11 of TIRS.

model, the subarctic summer atmosphere model, the subarctic winter atmosphere model and the US 1976 standard atmosphere model. In addition, 0.5, 1.0, 1.5 and 2.0 water vapor scalars are used. As well as in MODIS band shape adjustment, the ground temperature from 220 K to 340 K with 10 K interval are simulated in MODTRAN.

Figure A.2 shows the linear regression of the MODTRAN simulations. Obviously it is a linear relationship. After the linear correction, the RMS is reduced from 0.185 to 0.053 (band 10), from 1.175 to 0.314 (band 11). As expected, error of

adjusting from band 4 of GOES to band 10 is similar to the error of from MODIS to TIRS, RMS between 0.04 – 0.05. But a much higher error occurs adjusting from band 4 of GOES to band 11, where the RMS (0.314) is around 6 times of that from band 4 of GOES to band 10.

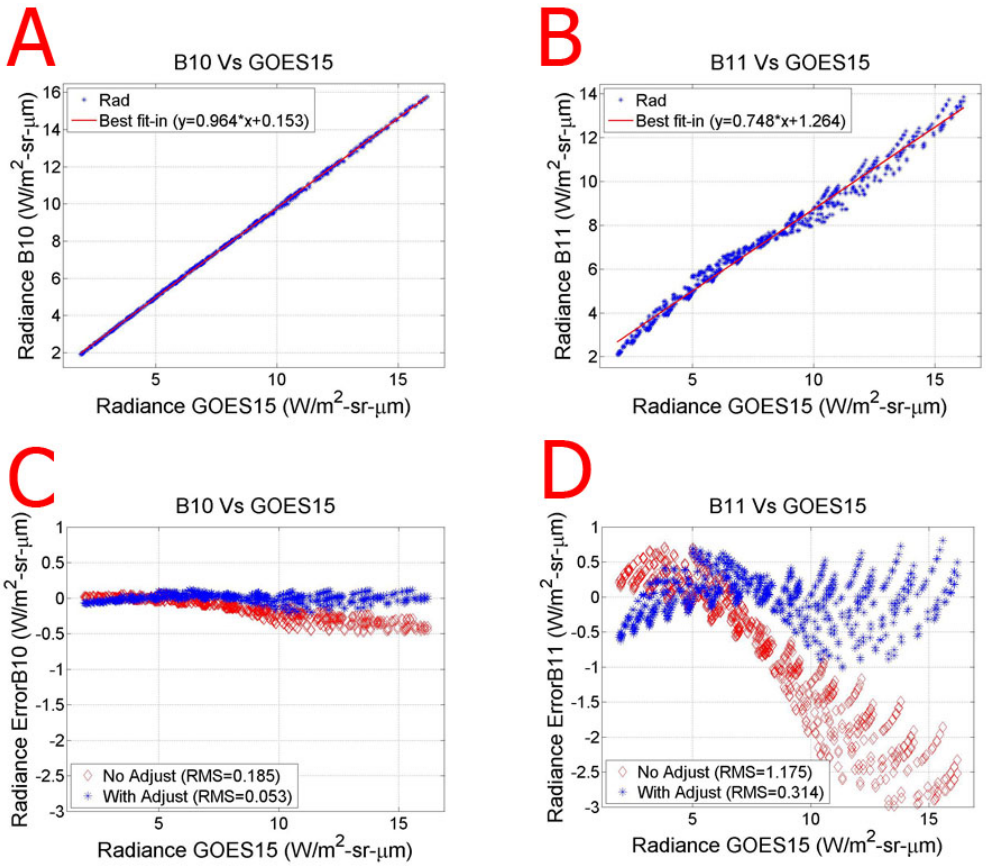

Figure A.2: Plots of the linear regression of band adjustment function between band 4 of GOES and band 10 of TIRS (A), and between band 4 of GOES and band 11 of TIRS (B). Plots of the error before and after linear regression for band 10 (C) and 11 (D).

Appendix B

View Angle Study of GOES

GOES is far away from earth (35,780 km altitude) in order to cover large area. There is also a view angle issue for GOES. Firstly, as GOES is far away from earth, the sensor view angle is far different from the effective view angle, which is the angle between the radiance path and the normal direction of the surface. Figure B.1 illustrates the sensor view angle and the effective view angle. It can be found that the sensor view angle for GOES (α) is less than 10°, but the effective view angle (β) can reach 90°. Assuming the equate of the Earth is a circle, the relationship between the effective view angle and the sensor view angle for GOES can be calculated, which is plotted in Figure B.2. As named in GOES, GOES is a geostationary satellite, which means GOES keeps relative still to the Earth. Therefore, for each location on earth, the sensor view angle and the effective view angle are constants for GOES. Figure B.3 shows the effective view angle for GOES 13 (centering at 75° West, east of US) and 15 (centering at 135° West, west of US) with the coastline in green dot lines.

As well as the exploration of view angle issue of MODIS, 1,638 MODTRAN simulations are used: combinations of three materials (snow, sea water, and sand), six atmosphere models (tropical atmosphere model, mid-latitude summer atmosphere model, mid-latitude winter atmosphere model, sub-arctic summer

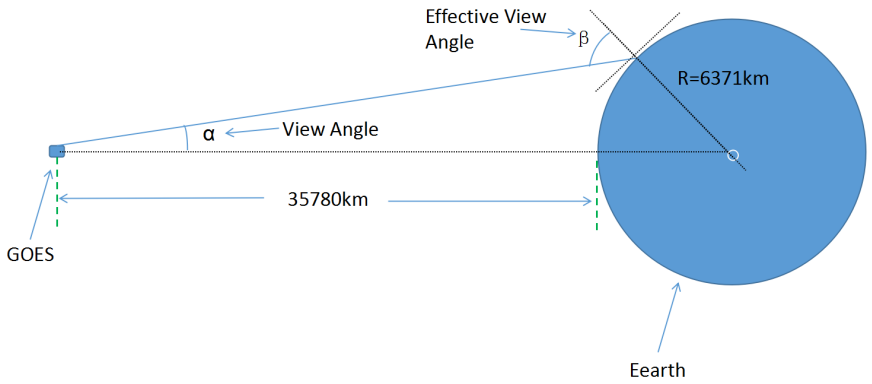

Figure B.1: Illustration of GOES effective view angle (left) and the relationship between effective view angle and sensor view angle (right).

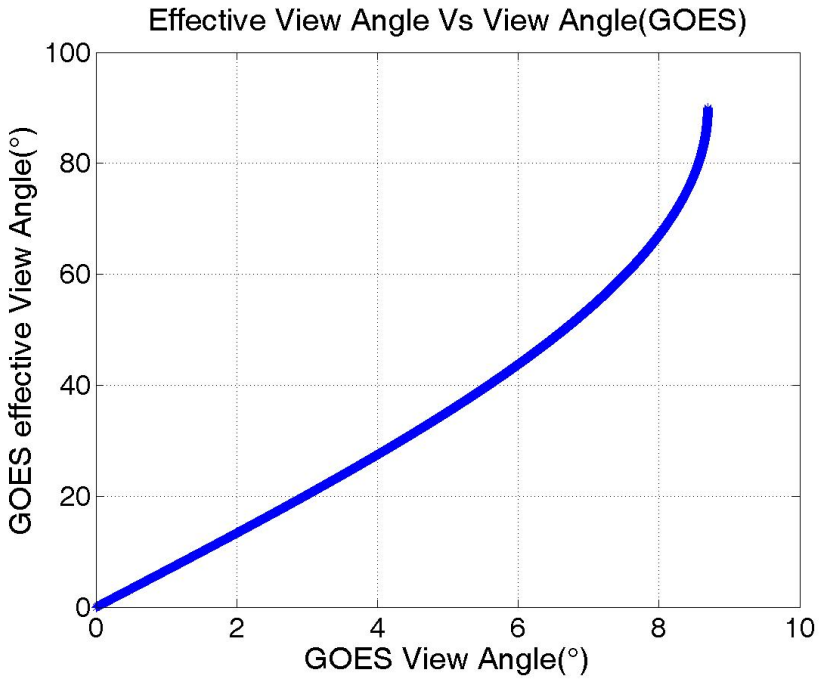

Figure B.2: Plot of *Effective View Angle vs Sensor View Angle*.

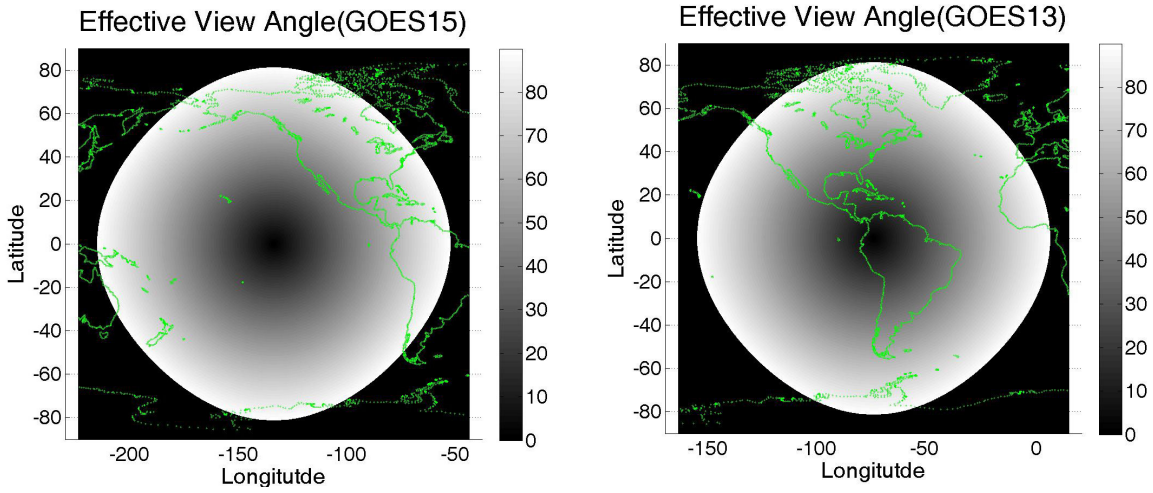

Figure B.3: Effective view angle for GOES13 (left) and GOES15 (right) with coast line of the continents in green dot line.

atmosphere model, sub-arctic winter atmosphere model and US 1976 standard atmosphere model), ground temperature (220 K to 340 K with 10 K interval), water vapor scalars (0.5, 1.0, 1.5, and 2.0), and the effective view angle (0° to 60° with 10° interval).

As the view angle analysis part of MODIS, view angle sensitivity order is: blackbody temperature > atmosphere model~water vapor scalar > material(sand, water, snow). For each black-body temperature, *Normalized Radiance vs View Angle* spreads out when view angle increases due to different atmosphere models, water vapor and materials. In order to present how much it spreads out, for any specific view angle, uncertainty is defined as half between the maximum and minimum of *normalized radiance*. Table B.1 shows the uncertainty Look-Up Table (LUT). This table also shows the effects from ground temperature. The uncertainty at 60° changes from 0.2642 at 220 K to 0.0564 at 290 K, then increases to 0.1379 at 340 K. This agrees with the view angle study of MODIS. In order to have a better visualization of the view angle, this uncertainty LUT can be mapped onto the

	0°	10°	20°	30°	40°	50°	60°
220 K	0	0.0034	0.0141	0.0333	0.0664	0.1249	0.2642
230 K	0	0.0031	0.0124	0.0295	0.0569	0.1057	0.2183
240 K	0	0.0026	0.0106	0.0251	0.0483	0.0856	0.1749
250 K	0	0.0021	0.0085	0.0202	0.0390	0.0687	0.1354
260 K	0	0.0016	0.0065	0.0154	0.0298	0.0525	0.1039
270 K	0	0.0011	0.0045	0.0108	0.0209	0.0370	0.0826
280 K	0	0.0007	0.0030	0.0072	0.0140	0.0253	0.0670
290 K	0	0.0006	0.0024	0.0059	0.0122	0.0238	0.0564
300 K	0	0.0009	0.0037	0.0088	0.0172	0.0311	0.0628
310 K	0	0.0014	0.0056	0.0133	0.0258	0.0457	0.0852
320 K	0	0.0018	0.0074	0.0176	0.0339	0.0595	0.1050
330 K	0	0.0022	0.0092	0.0217	0.0417	0.0725	0.1225
340 K	0	0.0027	0.0110	0.0255	0.0489	0.0848	0.1379

Table B.1: Uncertainty Look-Up Table (LUT) in unit of *Normalized Radiance*.

effective view angle plot in Figure B.3. Here only view angle from 0° - 60° is simulated. So the areas, where the effective view angle is over 60°, are masked out. Figure B.4 gives several uncertainty examples of GOES 13 at 220 *K*, 250 *K*, 280 *K*, 290 *K*, 320 *K* and 340 *K*. Figure B.5 shows the same examples of GOES 15.

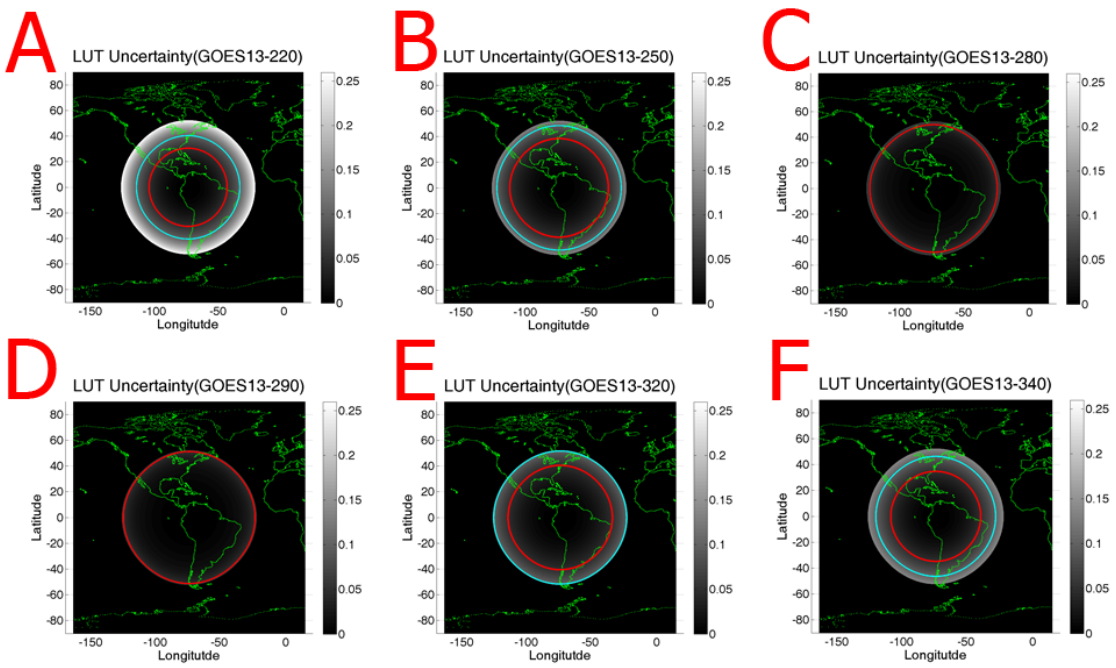

Figure B.4: Normalized radiance uncertainty for GOES 13 for ground temperature as 220 K (A), 250 K (B), 280 K (C), 290 K (D), 320 K (E) and 340 K (F). Red circle represents 0.05 and cyan circle represents 0.10. For all subplots, the horizontal axis is longitude and the vertical axis is latitude.

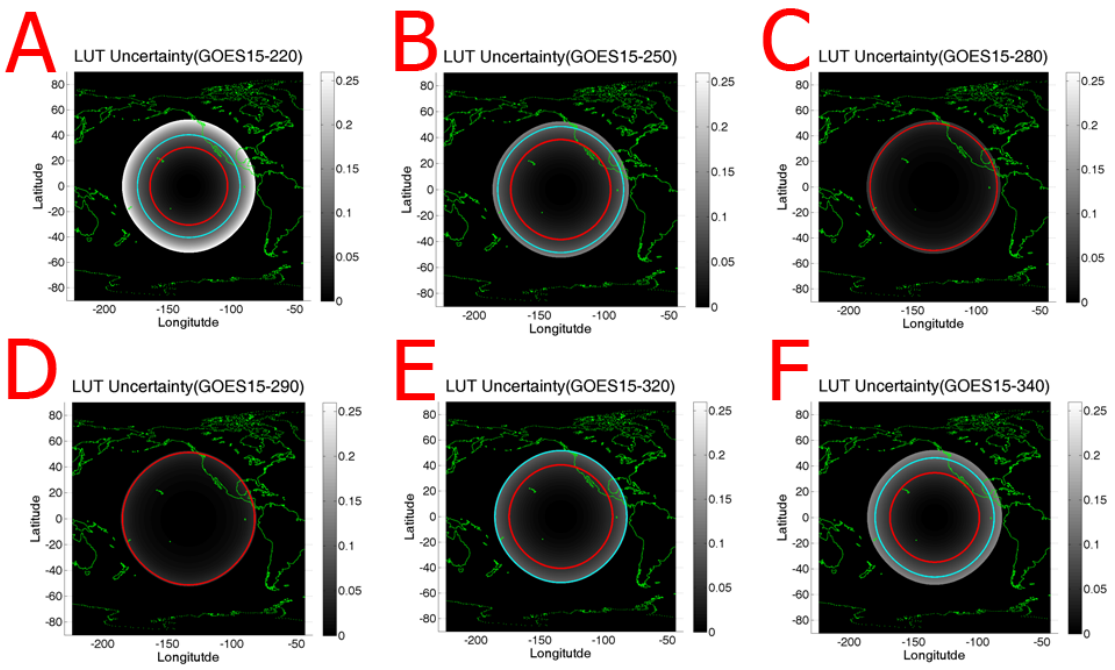

Figure B.5: Normalized radiance uncertainty for GOES 15 for grounp temperature as 220 K (A), 250 K (B), 280 K (C), 290 K (D), 320 K (E) and 340 K (F). Red circle represents 0.05 and cyan circle represents 0.10. For all subplots, the horizontal axis is longitude and the vertical axis is latitude.